MELTING BEHAVIOR OF FENI NANOPARTICLES ON W(110): INFLUENCE OF STOICHIOMETRY AND TEMPERATURE

Inaugural-Dissertation
zur Erlangung des Doktorgrades
der Mathematisch-Naturwissenschaftlichen Fakultät
der Heinrich-Heine-Universität Düsseldorf

vorgelegt von
Mahboobeh Ravankhah
aus Teheran, Iran

Düsseldorf October 2023

aus dem Institut für Angewandte Physik der Heinrich-Heine-Universität Düsseldorf

Gedruckt mit der Genehmigung der Mathematisch-Naturwissenschaftlichen fakultät der Heinrich-heine-Universität Düsseldorf

Referent: Prof. Dr. Mathias Gezlaff
Korreferent: Prof. Dr. Klaus Schierbaum

Tag der Mündliche Prüfung: 04.12.2023

Zusammenfassung

Diese Arbeit bietet einen umfassenden Überblick über meine Forschung, die in Zusammenarbeit mit dem Max-Planck-Institut in Düsseldorf am Institut für Angewandte Physik durchgeführt wurde. Die Studie gliedert sich in zwei verschiedene Teile, die jeweils verschiedene Aspekte des Materialverhaltens untersuchen.

Im ersten Teil lag der Fokus auf der Herstellung und Abscheidung von 3D-Bimetall-Nanopartikeln unter Verwendung einer Magnetron-Sputterquelle. Die Nanopartikel zeigten ein faszinierendes Schmelzverhalten bei Erwärmung. Durch sorgfältige Analyse wurde festgestellt, dass die Schmelzpunkte dieser Bimetall-Systeme zwischen denen ihrer monometallischen Gegenstücke lagen. Das Verhalten wurde zusätzlich durch Faktoren wie Stöchiometrie und die Struktur des Bimetall-Systems beeinflusst. Um dieses Phänomen zu untersuchen, wurden die Nanopartikel auf einem Wolfram-Substrat abgeschieden und mittels Rastertunnelmikroskopie und hochauflösender Transmissionselektronenmikroskopie detailliert analysiert.

Der zweite Teil meiner Arbeit drehte sich um die Synthese von Graphen auf einem dünnen Kobaltfilm und die Untersuchung der Mobilität und des Schmelzverhaltens von Nanopartikeln auf der Graphenoberfläche. Hierfür wurde Graphen mittels chemischer Gasphasenabscheidung mit einer dünnen Kobaltschicht auf einem W(110) Einkristallsubstrat hergestellt. Zur Charakterisierung der Graphen-Oberfläche wurden Rastertunnelmikroskopie und Niederenergie Elektronenbeugungstechniken angewendet. Bemerkenswerterweise unterschieden sich die Ergebnisse dieser Studie von früheren Experimenten mit Graphenoberflächen auf Eisen, Kobalt und Nickel, wie in den Masterarbeiten von Torsten Veltum, Wolfram Gilbert und der Bachelorarbeit von Hoai Nam Pham dokumentiert.

Um die Genauigkeit der Ergebnisse zu gewährleisten und eine Kontamination der Proben zu minimieren, wurden alle Experimente sorgfältig in einer ultrahochvakuum-Umgebung durchgeführt. Für die hochauflösende Transmissionselektronenmikroskopie-Analyse wurde jedoch eine kontrollierte Exposition der Nanopartikel gegenüber Luft durchgeführt.

Summary

This thesis provides a comprehensive account of my research carried out in collaboration with the Max-Plank-Institute in Düsseldorf at the Institute of Applied Physics. The study is divided into two distinct parts, each exploring different aspects of material behavior.

In the first part, I focused on the fabrication and deposition of 3D bimetallic nanoparticles, achieved through a magnetron sputtering source. The nanoparticles exhibited intriguing melting behavior when subjected to heating. Through careful analysis, it was observed that the melting points of these bimetallic systems lay between those of their monometallic counterparts. The behavior was further influenced by factors like stoichiometry and the structure of the bimetallic system. To investigate this phenomenon, I deposited the nanoparticles onto a tungsten substrate and utilized scanning tunneling microscopy and high-resolution transmission electron microscopy for detailed analysis.

The second part of my work centered around synthesizing graphene on a cobalt thin film and investigating the mobility and melting behavior of nanoparticles on the graphene surface. This involved the chemical vapor deposition of graphene with a Co thin film layer on top of a W(110) single crystal substrate. To characterize the graphene overlayer, scanning tunneling microscopy and Low Energy Electron Diffraction techniques were employed. Notably, the findings in this study differed from previous experiments conducted with graphene surfaces on Fe, Co, and Ni, as documented in the master thesis of Torsten Veltum, Wolfram Gilbert, and the bachelor thesis of Hoai Nam Pham.

To maintain the accuracy of the results and minimize sample contamination, all experiments were meticulously conducted in an ultra-high vacuum environment. However, for high-resolution transmission electron microscopy analysis, a controlled exposure of the nanoparticles to air was carried out.

Content

1 Introduction

Nanotechnology is a rapidly advancing field that involves manipulating matter at the nanoscale. At this scale, the properties of materials can be significantly different from their bulk counterparts, leading to unique characteristics. Some nanometerials exhibit superior electrical and thermal conductivity. Some have distinct magnetic characteristics or better light reflectivity.

The approach to nanoparticles can vary depending on whether the focus is on the bulk material properties or the individual atoms and their quantum mechanical behavior. The bulk material perspective allows for the use of classical physics and thermodynamics to describe and manipulate nanoparticles, while the atomic perspective requires the application of quantum mechanics to understand their properties at the atomic scale. Both perspectives are essential in comprehending the behavior and applications of nanoparticles in different contexts. One of the fascinating aspects of nanomaterials is the significant changes that occur in their properties as a function of size. As the size decreases, nanoparticles exhibit unique quantum confinement effects. For quantum dots, the discrete energy levels become prominent due to the confinement of electrons within a small volume. This leads to size-dependent optical properties, including changes in absorption, emission, and scattering behavior. Moreover, mechanical properties, such as strength and hardness, can be influenced by nanoparticle size. Smaller nanoparticles often exhibit enhanced mechanical properties due to their high surface area-to-volume ratio.

Furthermore, the properties of nanoparticles can be finely adjusted based on their composition. Nanoparticles can be made from various materials, such as metals, semiconductors, oxides, or composites, each with distinct properties. By altering the composition, one can tailor the nanoparticles' properties for specific applications. For example, gold nanoparticles exhibit a localized surface plasmon resonance, providing unique optical properties and enabling applications in sensing, imaging, and photothermal therapy. Semiconductor nanoparticles, like quantum dots, have tunable bandgaps that determine their absorption and emission wavelengths, making them valuable in optoelectronic devices and displays.

This thesis is focused on production and study of nanoparticles composed of iron and nickel and their alloys with different stoichiometry. The nanoparticles were produced with a magnetron sputtering source. They werde deposited on a tungsten surface with (110) orientation and graphene. A significant aspect of the scientific work during my doctorate involved the preparation of graphene on a thin film of cobalt. The nanoparticles were examined by scanning tunneling microscopy (STM), energy dispersive x-ray spectroscopy (EDX) and electron energy loss spectroscopy (EELS).

Deposition and examinations were taking place under ultra vacuum conditions. The nanoparticles were exposed to ambient air as part of the process of transferring them to another laboratory for EDX and EELS examinations.

Chapters: This thesis consist of 5 chapters. Chapter two provides an explanation of

the scientific background, focusing on the properties of nanoalloy on the surfaces specifically FeNi nanoparticles. In the next sections the theoretical aspects of the nanoparticles' supports i.e. tungsten and graphene are covered. The specific aspects relevant to this doctoral research are discussed in connection with recent findings from various research groups.

In chapter three the experimental background of various instruments and the experimental setup are explained. The upcoming discussion will cover the ultra-high vacuum system, followed by an introduction to the primary measurement systems: low-energy electron diffraction (LEED), scanning tunneling microscopy (STM), energy dispersive x-ray (EDX) and electron energy loss spectroscopy (EELS). A brief overview of the magnetron sputtering source and preparation of thin film with the evaporator are also covered and the chapter concludes with the preparation of the substrate.

Finally in chapter 4 the results obtained throughout this project are shown and discussed. For each measurement, detailed information will be provided regarding nanoparticle preparation and sample treatment. Additionally, the results will be thoroughly discussed, accompanied by potential explanations for the observed outcomes. A conclusion is provided along with an outlook for future research projects, emphasizing the potential for further exploration and development.

2 Scientific background

The topic of my thesis is nanoalloy and this chapter will discuss the fundamental aspects. Nanoparticles are small particles having size ranges from 1 to 100 nm. There are various methodes to synthesize such small particles. These methode are divided into two main classes: (1) bottom-up and (2) top-down approach. In the first approach, the nanoparticles are formed by means of chemical reaction among atoms or molecules, whereas top-down starting from bulk, which is decomposed into smaller units to form nanoparticles (Figure 2.1). Nanoparticles can also be deposited onto a substrate or embedded in a matrix, while such experiments simplify study of nanoparticles by microscopic techniques. Section 2.1 will introduce the properties of free and surface-supported nanoparticles. Nanoparticles may be composed of a single element or more than one element. Alloy nanoparticles with variable compositions add a new dimension to nanoscience and have many applications. Section 2.2 presents some theoretical and experimental studies of magnetic and structure properties of alloy nanoparticles. The structural and magnetic properties of nanoalloys may vary because of their composition. Section 2.3 focuses on the substrate and the interaction between nanoparticles and their support. The materials used for nanoparticles in this work will be introduced in section 2.4. Finally, section 2.5 gives an overview of graphene synthesis and its characterization.

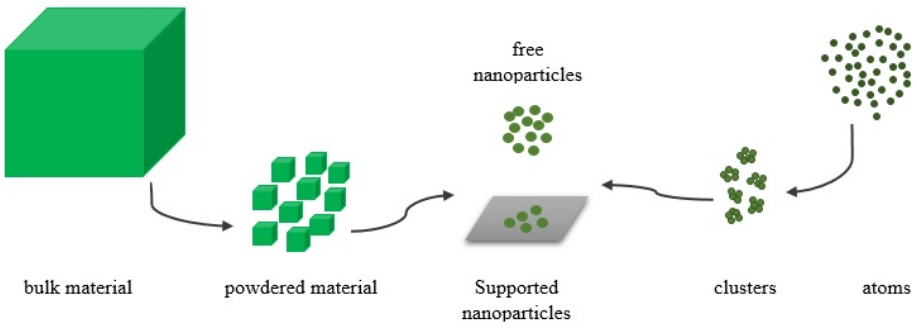

Figure 2.1: Top-down and bottom-up approaches to nanoparticle synthesis

2.1 Nanoparticles and Clusters

This chapter provides an overview of the properties and applications of supported nanoparticles. Preparation methods and some topics such as characterization and properties of nanoalloys are discussed.

2.1.1 Nanoparticle structure

The structure of a nanoparticle can depend on factors such as the method used to synthesize the particle, the materials used to make the particle, and the conditions under which the particle is formed. They can have a crystalline structure, be amorphous, or form pseudo-close packing that cannot be described by any of the crystallographic groups. They can have a variety of structures, including spherical, rod-like, and irregular shapes. One method to determine the equilibrium shape of a crystal or nanoparticle is the Wulff construction [1]. The theorem states that for a given solid of fixed volume, the shape that minimizes the total surface energy is the Wulff shape. The Wulff shape is determined by a balance between the surface energy of different crystal planes, represented by their Miller indices, and the lattice energy of the solid. The resulting shape is one of minimized total surface energy, where the length of the vector drawn perpendicular to the crystal face (h_j) is proportional to its surface energy (γ_j).

$$h_j = \gamma_j \lambda \tag{2.1}$$

where λ is a constant of proportionality.

Wulff's theorem has limitations because it assumes that the solid is in a state of equilibrium and that the surface energy is isotropic and homogeneous. In reality, many solids have surfaces that are not isotropic or homogeneous, which can affect their shape and stability. The formation of nanoparticles from the gas phase is far from equilibrium. In addition, in some cases the surface energy is not the only energy that determines the shape of the solid, and other factors such as chemical reactions or external forces may also play a role. Filipovich and Kalinina [2] proved that when nanoparticles reach a critical size, the contribution of surface energy to the free energy of a system increases significantly.

In practice, the nanoparticles need to be supported. The equilibrium shape of the supported crystal is expressed by the Wulff-Kaischew theorem, which induces the adhesion energy E_{adh}. The adhesion energy is a measure of how strongly the crystal and substrate are bonded at the interface. In the Young-Laplace equation, which describes the equilibrium shape of a droplet or a nanoparticle on a substrate, the adhesion energy can be related to the truncation of the nanoparticle Δh (see Figure 2.2) through the equation:

$$\frac{\Delta h}{h_j} = \frac{E_{adh}}{\gamma_j} \tag{2.2}$$

On a stepped surface, the step edges can provide nucleation sites for nanoparticle formation, leading to different behavior than on flat surfaces. Step edges provide additional surface sites for precursor molecules to adsorb and form small clusters. These clusters can grow into nanoparticles by diffusion and coalescence along the step edges. In addition, the growth rate at the step edges can be different from that on flat surfaces, resulting in differences in shape and size. A flat surface does not provide adsorption sites and the nucleation and growth of nanoparticles is very slow.

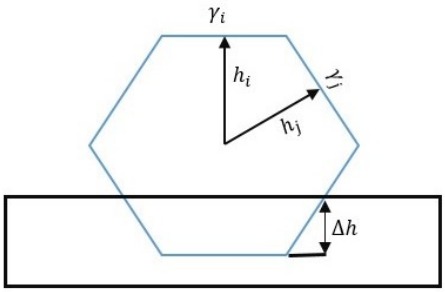

Figure 2.2: The equilibrium shape of the supported crystal is truncated by Δh, which is proportional to the adhesion energy. Adapted from [3]

2.1.2 Magnetism of nanoparticles

From a magnetic point of view, nanoparticles exhibit specific magnetic properties that are different from those of the bulk. The magnetic structure of nanoparticles, and consequently their magnetic behavior in an external magnetic field, is strongly dependent on their size. By reducing the size of the nanoparticle from tens to a few nanometers, the magnetic structure changes from a structure with magnetic domains, with non-uniform and stable magnetization, to a structure with stable and uniform magnetization or unstable magnetization (transition state). At very small dimensions it changes to a single domain structure with fluctuating magnetization along one direction in the crystal (superparamagnetic regime). The magnetic moments of the individual atoms in the cluster can also interact with each other, leading to collective magnetic behavior such as ferromagnetism or antiferromagnetism. Nanoparticles typically exhibit a higher level of magnetocrystalline anisotropy compared to bulk materials, and this anisotropy depends on the direction in which it is easiest or hardest with respect to the crystallographic axes. For example, for iron the directions |100|, |010| and |001| are the easy magnetization axis and |111| is the hard magnetization axis. The magnetic properties of iron and cobalt thin films and islands have been studied on a W(110) substrate [4]. With increasing temperature of the epitaxial thin films around 700 °C, three-dimensional islands were observed. Both the thin films and the cobalt islands showed remanent magnetization along the |110| axis of the substrate, while the magnetic dichroism disappeared after heating around 700 °C. In the presence of a magnetic field, certain materials exhibit different absorption properties for left-circularly polarized light and right-circularly polarized light when they interact with polarized light. This difference in absorption between the two polarizations is known as magnetic dichroism. A possible explanation could be that the easy magnetization axis of the Fe island is switched from the |110| to the |100| direction of the tungsten substrate, which means that there is no longer any long-range ferromagnetic order in the island structure.

The nanoparticles produced in this work are smaller than 10 nm. These small particles have a single domain of uniform magnetization.

The magnetic moments of Fe, Co and Ni clusters are studied as a function of temperature and size [5]. In all three cases, small clusters exhibit spin imbalances close to those predicted by the atom-based localized moment model. As the clusters increase in size, the

spin imbalances gradually approach the levels observed in bulk materials. Nickel clusters show a faster convergence to the bulk limit compared to Co and Fe clusters. Specifically, a nickel cluster consisting of about three layers of atoms (N_{150}) exhibits bulk-like behavior, whereas Co and Fe clusters require about four to five layers (Co_{450}, Fe_{550}) before reaching the same bulk-like properties. This observation suggests that the perturbations caused by the surface penetrate deeper into the cluster as its size increases. The ferromagnetic state depends not only on the presence of magnetic moments, but also on their orientation, even at high temperatures. Experimental results show that even in small clusters the mutual alignment of magnetic moments remains significant. For example, Ni clusters show a nearly constant interaction up to 300 K, indicating a strong alignment similar to the bulk. However, a smoother transition is observed near the Curie temperature (T_c), which is a characteristic effect of small particles. Co clusters also show bulk-like behavior, with a slight increase in interaction with increasing temperature. In contrast, Fe clusters show anomalies due to the sensitivity of the magnetic moment to the crystal structure. The phase transition occurs at lower temperatures as the cluster size increases, but this trend is expected to reverse in larger clusters to match the bulk behavior. The anomalous behavior in Fe clusters is primarily influenced by surface induced electronic effects that affect the magnetic moments of atoms deep within the clusters.

Isabelle et al. [6] studied iron clusters with 25 to 700 atoms in a molecular beam at different temperatures. These clusters were produced by a laser evaporation cluster source. The temperature of the nozzle in this source was varied between 100 and 1000 K and the clusters were deflected in the field of a Stern-Gerlach magnet. According to the superparamagnetic model, when an external magnetic field is applied to an assembly of superparamagnetic nanoparticles, the magnetic moment of a monodomain particle μ tends to align with the external magnetic field B. However, thermal motion opposes the alignment, so in equilibrium the magnetization M is related to temperature and field by:

$$M = \mu^2 B/3kT \tag{2.3}$$

where k stands for the Boltzmann constant and T represents the temperature.

In this experiment, the researchers examined the superparamagnetic model. Their findings revealed that the magnetization experiences growth as the clusters spend more time exiting the nozzle and becomes constant after sufficient time. However, at very small time intervals, the magnetization at $T = 120$ K is less than that at $T = 320$ K. On the other hand, for supersonic conditions, the magnetization is not linear with the external magnetic field. These observations challenge the validity of the superparamagnetic model under supersonic conditions, indicating that the magnetization must depend on more than the external field and temperature.

The dependence of the magnetic moment on cluster size has been determined. For Fe_{50-60} and two larger size ranges, $Fe_{250-290}$ and $Fe_{500-600}$, μ decreases gradually with increasing temperature. For Fe_{80-90} and $Fe_{120-140}$, μ is approximately constant at lower temperatures and then decreases. In general, it has been seen that the larger particles have smaller magnetic moments compared to the bulk, with increasing temperature, μ decreases and finally disappears at the Curie temperature $T_c = 1043$ K. The decrease of μ is related to the thermally induced disorder in the mutual orientation of the spins.

Although free particles offer a way to study the particles without the influence of

a surface, supported nanoparticles are more suitable for technological applications. Free clusters are isolated and not in contact with any other material. In this case, the magnetic properties of the cluster are determined solely by the magnetic moments of the atoms in the cluster and their interactions. The interaction between the cluster and its substrate influences the magnetic properties. Supported clusters are in contact with a substrate or matrix, and the magnetic properties of the substrate can influence the magnetic properties of the cluster. For example, the substrate can provide an exchange interaction between the magnetic atoms in the cluster, which can result in a higher magnetic moment or a higher magnetic ordering temperature compared to a free cluster. The substrate can also induce magnetic anisotropy in the cluster, which can lead to a preferred orientation of the magnetic moment. For supported clusters, the average magnetic moment decreases monotonically with increasing size [7, 8], while for free clusters it decreases in a non-monotonic oscillatory manner [9–11]. Ab-initio spin density functional theory has been used to study the dependence of magnetic moments on cluster size for free and supported clusters of identical size and shape [12]. They investigate the magnetic moments in Fe and Co clusters either free or supported by a substrate. It was observed that the local spin magnetic moments for free clusters are much more complex than for supported clusters of the same size range. This is consistent with the fact that the peaks in the density of states or spectral distribution function are sharper for the free clusters than for the supported clusters.

A metal substrate can induce a strong exchange interaction between the magnetic moments of the cluster and the substrate atoms, leading to a higher magnetic moment and a higher ordering temperature. On the other hand, a non-magnetic substrate such as carbon or silicon dioxide can provide weaker exchange interactions, leading to a lower magnetic moment and a lower ordering temperature.

2.1.3 Melting of nanoparticles

There are dramatically different melting behaviors and thermodynamic properties between nanoparticles and the bulk. Macroscopic (bulk) material should have a constant melting point regardless of its size because the percentage of atoms at the surface is very small relative to the total number of atoms in the bulk material. As the dimensions of materials decrease toward the nanoscale, some physical and chemical properties of nanomaterials differ significantly from those of bulk materials. Nanoscale materials have a much larger surface-to-volume ratio, which changes their thermal properties and melting point. The change in melting point can be on the order of tens to hundreds of degrees for nanoscale metals. This is because surface atoms have fewer neighboring atoms in close proximity compared to atoms in the bulk of the solid. Each chemical bond that an atom shares with its neighbors provides cohesive energy. The cohesive energy of an atom is directly related to the thermal energy required to release an atom from the solid. Thus, atoms at or near the surface have reduced cohesive energy due to the reduced number of bonds. The lower melting point of nanoparticles results from this effect.

In general, the model of the size-dependent melting temperature of spherical nanoparticles can be described as a linear relationship between the melting temperature and the

reciprocal radius of the particle [13]:

$$T_m = T_{bulk}(1 - \frac{c}{r_s}) \tag{2.4}$$

where c is a material constant related to material properties. As the size of nanoparticles decreases to the atomic scale, the melting temperature scales with the diameter, as shown in Figure 2.3, which shows the temperature depression of gold nanoparticles as a function of size. The solid line is the melting temperature from the calculated result and the points are from experimental data.

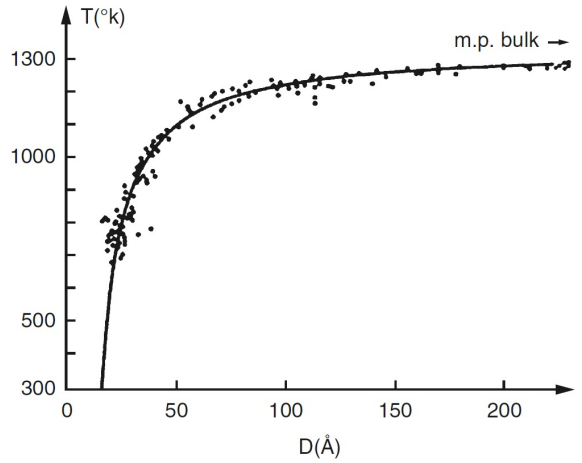

Figure 2.3: Size-dependent melting temperature of gold nanoparticles (from [14])

Classically, the melting behavior of nanoparticles can be described in three ways. The first is the homogeneous liquid drop model (HLDM). It assumes that the entire particle is in a homogeneous phase and the transition occurs at a single temperature. According to the HLDM, the melting behavior of a material can be described by a balance between the energy required to overcome the interatomic forces holding the solid together and the energy released by the increase in entropy as the solid melts. The surface energy term in the HLDM plays a critical role in determining the melting point of the material because it determines the energy required to create a new surface between the solid and liquid phases. The HLDM can be used to predict the melting temperature of a material based on its atomic structure and composition. However, the model has limitations because it assumes that the material is perfectly homogeneous and that the interatomic forces are isotropic, which may not be the case for all materials.

Based on the Liquid Shell Nucleation (LSN) model, a surface layer of atoms melts before the bulk, meaning that the larger particles have a higher melting point due to their larger radius.

The liquid nucleation and growth model predicts that the surface of the nanoparticle melts first, and the liquid-solid interface grows and moves through the entire particle. Thus, the melting temperature of nanoparticles depends on the size of the particle, the interfacial energies between the solid and liquid phases, and the density of each phase.

All of the above models are based on spherical and free particles. However, almost all experiments have been performed on a solid substrate. Due to the different synthesis methods and growth mechanism of nanoparticles, they can be not only spherical, but also

triangular, nanorods and hexagon and many other shapes, so the surface to volume ratio of different shapes can also be varied. Then, the models should be modified based on the shape and dimension of the nanostructure [15]. When a small nanoparticle is supported on a substrate, the substrate can provide a stabilizing effect, resulting in a higher melting point compared to a free nanoparticle of the same size.

The melting behavior of supported nanoparticles can also be influenced by the nature of the substrate, including crystal matching, chemical interactions, surface morphology, and heat transfer properties. For example, a nanoparticle supported on a crystalline substrate may have a higher melting point if the crystal structure of the substrate closely matches that of the nanoparticles. In this case, the interface between the nanoparticles and the substrate is well-aligned, resulting a more stable interface. This increased stability can require more energy to initiate the melting process. Similarly, a nanoparticle supported on a substrate with strong chemical interactions may have a higher melting point due to the formation of strong bonds between the particle and the substrate.

The size and shape dependent melting temperature of gallium nitride nanoparticles with their spherical and cylindrical geometry has been studied using the numerical thermodynamic model [14]. They have considered the radius of curvature to explain the difference in shape and developed the model for cylindrical nanoparticles. According to the relationship between the total surface free energy and the radius of curvature, an expression for the size and shape dependence of the melting point of nanoparticles is developed. It is shown that the melting point of GaN nanoparticles decreases consistently with the size of the nanoparticles. However, this decrease is greater for cylindrical than for spherical shape.

The melting point of 3-6 nm spherical nickel nanoparticles on carbon-coated copper grids has been studied using dynamic transmission electron microscopy and compared with molecular dynamic predictions [16]. The melting point was recorded over a temperature range of 700-1100 °C and the nanoparticles were found to have melted when the average diameter of the spherical nanoparticles rapidly increased. For a 4.3 nm nanoparticle, there was an abrupt, sustained increase at (925±25) °C. This process was repeated for the other nanoparticles and the melting point decrease was compared with the Gibbs-Thomson, liquid-drop, and liquid nucleation and growth models. The experimental data showed that the melting point of nanoparticles decreases with size and for nanoparticles between 3.5 nm and 5.3 nm there was a very good agreement with the liquid nucleation and growth model, which assumes that the liquid phase is initiated at the surface and propagates towards the centers.

2.2 Nanoalloy

Nanoalloys can be formed by mixing elements that are immiscible in the bulk. In some cases, nanoalloy systems exhibit high stability, enhanced catalytic activity, improved mechanical strength, and unique magnetic and optoelectronic properties compared to their pure metal counterparts. These improved characteristics offer possibilities for their application in fields including pollution control, data storage, sensors, imaging, and enhancing the effectiveness of medications. This section briefly introduces the structure and characterization of magnetic nanoalloys.

2.2.1 Magnetic 3d alloys

Understanding the magnetic behavior of magnetic alloys will allow us to control the fundamental properties of the material, such as saturation magnetization and magnetic anisotropy, for a variety of technological applications. Magnetic nanoalloys are interesting because of the possibilities to manipulate them with different size, structure and chemical order. The magnetic properties of nanoalloys can be influenced by the composition of the constituent metals. When two or more metals are mixed in a nanoalloy, their magnetic moments can interact, leading to the formation of new magnetic phases with different magnetic properties. The presence of magnetic or non-magnetic elements in the nanoalloy can also affect the magnetic properties, as the magnetic moment can be modified by the exchange interaction between the different elements. The magnetic moment of an atom is determined by the number of unpaired electrons in its outermost shell. We consider the ground state of an isolated Co atom, $[\mathrm{Ar}]3d^7 4s^2$, the inner shells and the $4s$ shell are completely filled, so they have no contribution to the magnetic moment, and all contributions are due to the 7 electrons in the $3d$ shell. Therefore, the magnetic moment of a multi-metal alloy depends on the number of unpaired electrons contributed by each metal. For example, if one metal has more unpaired electrons than the other, the magnetic moment of the nanoalloy will be dominated by the metal with more unpaired electrons. Most of the studies on magnetism in nanoalloys are related to the system where $3d$ metals are alloyed with $4d$ or $5d$ metals. Since the large spin-orbit coupling of the $4d$ and $5d$ atoms and the large magnetic moments of the $3d$ atoms can enhance the magnetic anisotropy of the system compared to pure $3d$ systems.

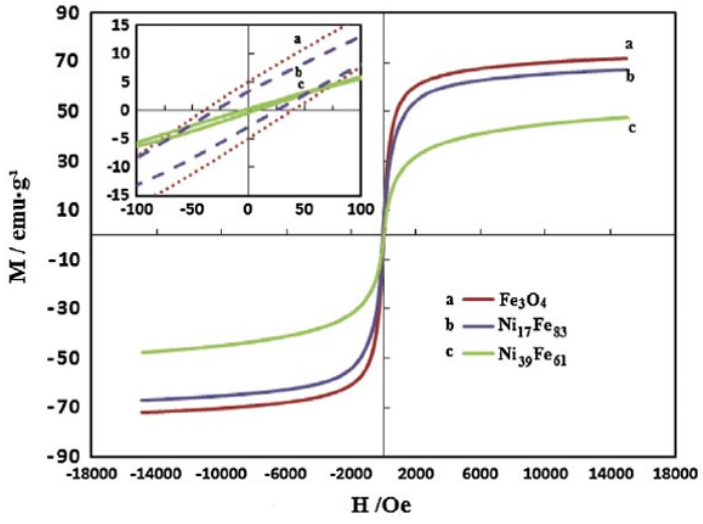

Figure 2.4: Magnetization curves for the nanoparticles synthesized with different initial ratios of Ni to Fe, from [17]

Figure 2.4 illustrates a representative series of magnetization curves for particles synthesized via the hydrothermal method using different initial ratios of Ni to Fe [17]. Parameters extracted from the hysteresis loop to evaluate the magnetic properties of these nanoparticles include saturation magnetization (Ms), remanence (Mr), and coercivity (Hc). Examination of these values suggests a potential minimum point with increasing

percentage of Ni in the nanoparticles. This trend could be related to a structural transition from a spinel to an fcc-type structure within the nanoparticles. Notably, changes in particle size were evident as the composition of the nanoparticles changed, making it difficult to determine a specific pattern.

Magnetocrystalline anisotropy (MCA) is a property of magnetic materials that describes the dependence of their magnetic energy on the orientation of the magnetization with respect to the crystal lattice. The interaction between the spin and orbital moments of the electrons in the crystal lattice of the magnetic material can cause certain directions of magnetization to be energetically favored over others, resulting in a preferred direction of magnetization. The magnetocrystalline anisotropy of L10 ordered alloys such as FePt, FePd, CoPt, and FeNi is widely recognized because of their magnetic properties [18, 19]. L10 refers to a crystal structure, also known as the tetragonal structure, which has an elongated shape along one axis. The strong MCA in these materials makes it possible to stabilize the magnetic bits used to store data in very small areas, which is critical for the development of high-density data storage devices.

FePt and CoPt nanoalloys are expected to exhibit high magnetocrystalline anisotropy. A considerable amount of research effort has been directed toward exploring the magnetic properties of nanoalloys. In nanoalloys composed of both Co and Pt for compositions close to 1:1, a clear transition from superparamagnetic to blocked behavior is observed [19]. The measured magnetic anisotropy energy (MAE) values of Co-Pt nanoalloys are consistently higher than those observed for pure Co nanoparticles of equivalent size [20]. This is consistent with the theoretical prediction that the majority of the MAE results from the bonding between Co and Pt [21].

Using a molecular beam epitaxy system, L10-FeNi films with different levels of anisotropy were fabricated by manipulating the deposition process. Three different levels of anisotropy were obtained by this technique [22]. Hysteresis measurements were performed to investigate the magnetization reversal and magnetic domain structure. The quadratic hysteresis loop of all samples indicated that the magnetization reversal occurs through the process of nucleation and subsequent movement of domain walls. Therefore, it is possible to fabricate thin films of L10-FeNi with variable anisotropy, allowing the adjustment of magnetization reversal.

Using first-principles density functional calculations, Miuara et al. [23] investigated the MCA energy of L10-FeNi. The Fe atoms present in L10-FeNi are mainly responsible for the perpendicular MCA observed in it. They found that decreasing the in-plane lattice parameter is an effective means of increasing the MCA energies. The effects of Co incorporation on the structure and magnetic properties of L10-FeNi thin films were investigated by Kojima et al. [19]. It was found that replacing Ni atoms with Co, without reducing the order parameter, leads to an improvement in the uniaxial magnetic anisotropy.

2.2.2 Nanoalloy structure (Homogeneity)

Nanoparticle production often involves processes that are not in equilibrium. Rapid cooling of a hot vapor plume leads to supersaturation and aggregation of atoms into particles that may not have the geometric structure or morphology corresponding to the lowest (free) energy state. This is particularly important for nanoalloys, which have a very com-

plex potential energy. For this reason, nanoalloys can form different structures according to the mixing pattern, as shown in Figure 2.5. Core-shell nanoalloys consist of a core of material A and a shell of material B, and multishell structures have onion-like A-B-A shells. Mixed A-B nanoalloys can be ordered or disordered. Subcluster segregated nanoalloy A and B subcluster, where they share a mixed interface. In recent experiments, three-shell Pd-Au nanoparticles have been successfully created. These nanoparticles exhibit a mixed core, an intermediate shell enriched with Au, and an outer shell enriched with Pd [24].

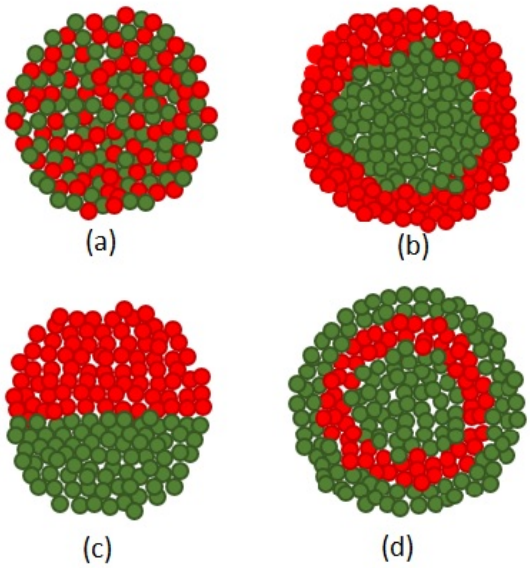

Figure 2.5: Schematic representation of different mixing patterns, (a) mixed, (b) core-shell, (c) subcluster segregated, (d) multishell. The image shows a cross-sectional view of the clusters.

The mixing patterns are typically categorized according to their degree of order, which can range from perfectly ordered phases to completely random solid solutions.The transition from the disordered to the ordered phase can be driven by various factors such as temperature, pressure, or the presence of impurities. Co-Pt and Fe-Pt are examples of systems that exhibit ordered phases for certain compositions. The L10 phase (for 1:1 compositions) and the L12 phase (for 3:1 and 1:3 compositions) are based on the fcc lattice [25, 26].

The core-shell structure can improve the performance and stability of the nanomaterial. For example, a core-shell nanoalloy with a catalytic core and a protective shell can be used as a catalyst that is resistant to deactivation by impurities in the reaction environment. There are complex factors that influence the growth and structure of bimetallic nanoparticles. The knowledge of a phase diagram of a given bimetallic nanoparticle is certainly helpful to predict the properties of nanoparticles, but it is limited for bimetallic particles because it describes the thermodynamic equilibrium phase. In addition, surface energy effects, which are sometimes dominant for nanoparticles, are not taken into account in the phase diagram. The properties of nanoparticles depend not only on their size, but also on their actual shape and composition. For example, certain properties of

magnetic nanocrystals such as blocking temperature, magnetic saturation and permanent magnetization are all dependent on particle size [6, 27], but the coercivity of nanocrystals is totally dependent on particle shape due to surface anisotropy effects [28].

Several methods can be used to produce nanoalloys, including vapor condensation, chemical reduction, thermal decomposition of transition metal complexes, electrochemical synthesis, and even biosynthesis. Vapor condensation involves the evaporation of metals in a vacuum chamber followed by condensation of the metal vapors onto a substrate of controlled size and composition. Compared to many wet chemical methods, this technique has the advantage of producing self-standing, high purity nanoalloys without the presence of ligands. There are several methods for generating vapor from solid precursors, including thermal evaporation, laser ablation, ion or magnetron sputtering, and electrical discharge. In this work, we produced nanoparticles by magnetron sputtering of alloy targets.

It is important to ensure that the elemental composition of the produced nanoalloys matches the expected stoichiometry of the synthesis process. Therefore, advanced analytical techniques capable of distinguishing elements at the nanometer scale or smaller are required. Such techniques are commonly associated with high-resolution transmission electron microscopy, such as energy-dispersive X-ray spectrometry (EDX) and high-angle annular dark-field (HAADF) imaging. These methods are discussed in sections 3.4 and 3.5.

Au_xAg_{1-x} were prepared by pulsed laser ablation and deposited directly into the TEM carbon grids to study the atomic arrangement of Au and Ag atoms in the nanoparticles [29]. According to the STEM HAADF images and the STEM simulated profile of pure gold and pure silver, the composition of the cluster core is always enriched with the minority element. The gold-rich nanoparticles have a core of silver, while for silver it is reversed. A complete mixing is observed when two elements are present in the same amount.

The non-uniform composition profile in a nanoalloy can be attributed to surface segregation of one of its elements. This tendency can lead to depletion of the interior of the nanoalloy, resulting in patterns with characteristics intermediate between mixed and core-shell, or even a complete core-shell structure.

2.3 Tungsten surfaces

The properties of tungsten as a substrate and the diffusion of nanoparticles on its surface are presented in this section.

Tungsten is a transition metal with a high melting temperature of 3422 °C. It has a body-centered cubic (bcc) crystal structure with a lattice parameter of 3.165 Å . Tungsten has a low coefficient of thermal expansion, high thermal conductivity, excellent mechanical strength, and significant spin-orbit coupling, making it useful in industry and for researchers working on the fundamental physics of thin films and nanostructures. Tungsten has been most commonly used as a substrate to support thin films and nanoparticles. All low-index surfaces of tungsten can be prepared as substrates, including the (100), (110), and (111) surfaces [30]. The (110) surface has a higher surface reactivity compared to the (100) and (111) surfaces, which makes it useful for certain chemical reactions and cat-

alytic applications. The surface energy of (100) and (110) is highly anisotropic, resulting in different surface energies in different crystallographic directions. This property can be used to create well-ordered structures and to regulate the orientation of adsorbed atoms and molecules. The (100) surface has a low surface roughness, which is advantageous for growing thin films with uniform thickness and morphology. The (111) surface is the most stable of all the low-index tungsten surfaces under certain conditions, such as in the presence of oxygen or at high temperatures, making it useful for high-temperature applications. Figure 2.6 illustrates the surface structure of a bcc(110) facet.

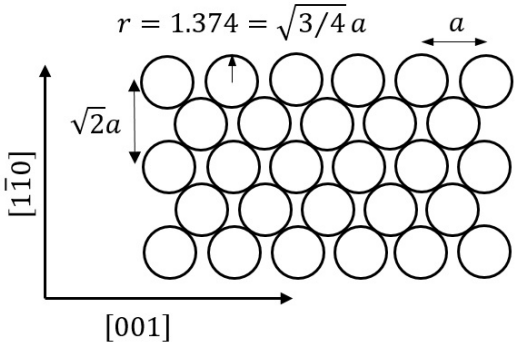

Figure 2.6: The structure of the bcc W(110) surface; r is the radius of a tungsten atom, and a is the lattice constant.

The most common impurities on the W(110) surface are carbon and oxygen. It is observed that the annealing of W crystal results in the segregation of carbon from the bulk to the surface [31]. Therefore, annealing the substrate in the presence of oxygen atmosphere leads to the reaction of carbon with oxygen and formation of CO [32, 33]. Prolonged annealing can result in excessive heat transfer to the ultra-high vacuum (UHV) components, leading to degraded vacuum conditions. In addition, a layer of tungsten oxide can form on the surface. To remove the oxide layer, the tungsten crystal should be heated to 2200 °C.

2.3.1 Diffusion on a bcc (110) surface

Understanding surface diffusion at the atomic scale is critical to gain a better understanding of the film growth and spreading behavior of nanoparticles at high temperatures. The diffusion of metal clusters on tungsten surfaces can occur by a variety of mechanisms, including thermally activated diffusion, surface diffusion, and Ostwald ripening.

Figure 2.7 shows the possible diffusion behavior of an atom on the bcc(110) surface. The diffusion of a single free atom (atom 1) can occur along (111) direction, but the possibility of hopping along (001) is quite small. The basic step of the hopping mechanism is a thermally activated jump from one equilibrium adsorption site to the next. As a result, it is more likely that atom 2 will detach from the step edge than move along it. On the other hand, atom 3 can easily diffuse along its step edge ((111) direction) until the number of nearest neighbors is maximized, it will remain there. Atom 4 will not migrate along the edge of the island, since the on-top position is involved in the process. Therefore, it implies that the (110) edges cannot expand, and the atom can detach from the island [34]

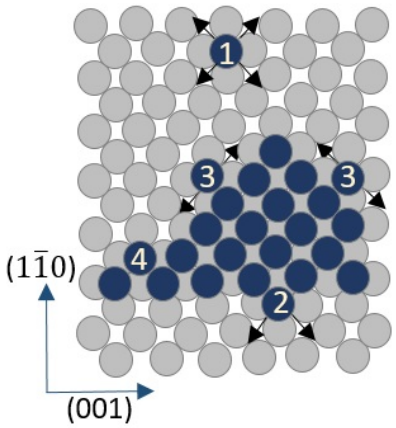

Figure 2.7: Diffusion of atoms on a bcc (110) surface (from [33])

When an atom reaches an island, it seeks an energetically favorable location. In certain cases, an adatom may be able to move along the edge of an island, but it may not be able to cross the corner. Without crossing the corner, the growth process results in the development of branched, fractal-like islands. As the temperature increases, there is a transition from fractal-like growth to compact island growth because edge diffusion increases.

Diffusion processes become more complex when the diffusing species consists of a cluster rather than a single adatom. The diffusion behavior of various tungsten clusters with different numbers of adatoms has been studied using molecular dynamics (MD) simulations [35]. Numerous migration events were observed during the diffusion processes. The clusters tended to maintain their compact configurations for long periods of time. However, in certain cases, the clusters temporarily exhibited a distorted shape, while the adatoms eventually returned to their original configurations. Some of these processes involved localized motion of the adatoms without displacement of the cluster's center of mass. The research found that clusters composed of six or more atoms exhibited lower mobility, particularly in terms of mass center displacement, resulting in relatively high migration energies for diffusion. Clusters consisting of five atoms or less did not exhibit a dimer-shearing mechanism. The MD simulations suggested that the migration of the clusters occurred by a successive hopping mechanism of atoms at the edge of the cluster.

2.3.2 Unrolling carpet

The unrolling carpet (Figure 2.8) refers to the mechanism in which the atoms of the first layer are strongly bound to the substrate and are immobile. Otherwise, the atoms of the second layer are weakly bound to the substrate and highly mobile. Under these conditions, the atoms of the second layer will move toward the edges of the first layer. The first layer can be a single monolayer (ML) or thicker [36].

In the study by Butz and Wagner [37], 2 mm long Pd filaments were evaporated onto different tungsten surfaces. The researchers observed the subsequent annealing of this quasi-one-dimensional system using Scanning Auger Microscopy (SAM). By subjecting the system to a heat treatment at 1068K, a diffusion zone of 1 monolayer (ML) in height and over 1 micrometer in width was created, characterized by a distinct boundary. Two

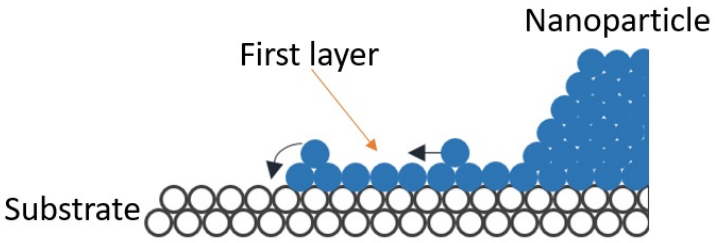

Figure 2.8: The hard ball model of the unrolling carpet mechanism

additional treatments at the same temperature expanded the diffusion zone and blurred the boundary. The formation of additional layers occurred only after the initial layer had spread over several micrometers, and this effect could be corrected by prolonging the annealing time. They suggested that a higher binding energy of atoms in the first ML compared to atoms in subsequent layers was the reason for this kind of spreading behavior.

2.3.3 Anisotropic spreading of nanoparticles on tungsten

The tendency of nanoparticles to spread preferentially along certain crystallographic directions of the tungsten surface is due to the anisotropy of tungsten. This behavior varies with the crystallographic orientation of the surface.

Two reasons for anisotropic spreading have been reported, one is the crystallographic structure of the surface and the other is steps on the surface [38]. The anisotropic spreading of the W(110) surface can be dominated by either the step orientation or the crystallographic structure. The dominant regime depends on the material and the temperature.

The anisotropic diffusion of Fe, Ni, Co and Cu on a W(110) surface has been investigated using scanning electron microscopy (SEM) and scanning Auger microscopy (SAM) [39]. The samples were repeatedly annealed at 720 to 1070 K for 20 s to 30 min. It was observed that Fe formed elliptically shaped islands after annealing. This implies that the Fe diffusion is caused by the crystallographic structure of the substrate, where the fast diffusion direction is along [110] and the slow diffusion direction is along [100]. Co and Ni showed different behavior at low temperature, but at higher temperature, the spreading anisotropy was very similar to that of Fe, and the influence of steps became weaker. For Cu, the fast spreading direction for the first monolayer is oriented along the step direction, while the anisotropic spreading of the second monolayer is attributed to the crystallographic structure.

2.4 FeNi nanoparticles

The iron-based alloys exhibit ferromagnetism at room temperature. FeNi and NiCo have soft magnetic properties such as low coercivity and high saturation magnetization. Nanostructured $Fe_{1-x}Ni_x$ has shown promising applications in various fields. They can be used as an essential component in high-density magnetic recording and in the fabrication of

sensors. Here are some properties of FeNi nanoparticles.

2.4.1 Magnetic properties

FeNi alloy exhibits ferromagnetic behavior at room temperature. At high temperatures, it may exhibit paramagnetic behavior. The most common crystal structures of FeNi alloys are face-centered cubic (fcc) and body-centered cubic (bcc). The structural and magnetic phase diagram of FeNi is shown in Figure 2.9.

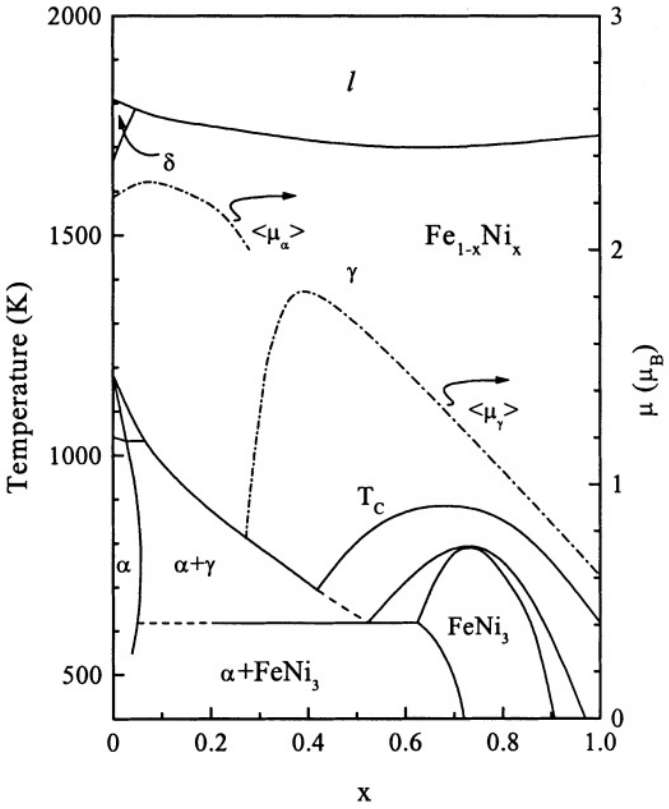

Figure 2.9: Structural and magnetic phase diagram of $Fe_{1-x}Ni_x$ (from [40])

The dominant phase is the γ phase with an fcc structure. The addition of nickel to iron increases the temperature range of face-centered cubic (fcc) stability in γ-Fe, resulting in the formation of a continuous series of fcc $Fe_{1-x}Ni_x$ alloys. The α phase occurs when x is less than 0.5.

The magnetic properties of nanoparticles are strongly influenced by their size, shape and composition. Recent studies have explored various methods to regulate the size and chemical ordering of FeNi alloy nanoparticles. The research has shown that the saturation magnetizations (M_s) of non-heat-treated FeNi nanoparticles (NPs) decreased with increasing Ni content. On the other hand, the saturation magnetizations of heat-treated NPs generally increased as the temperature of heat treatment was increased [41]. The temperature-dependent magnetic characteristics of FeNi nanoparticles have been investigated across various sizes (ranging from 4 to 16 nm) and with consideration of core-shell chemical ordering [42]. As the nanoparticle size decreases, the magnetic behavior around

the transition point becomes less critical and broader. In addition, a decrease in the magnetic ordering temperature is observed with increasing nanoparticle size. For 4 nm Fe@Ni core-shell nanoparticles, the mean temperature-dependent magnetization remains relatively constant when transitioning from elemental Fe nanoparticles to Fe1.0@Ni0.25 nanoparticles (the numerical values denoting the portion of the radius taken up by Fe and/or Ni atoms within the 0 to 1 range). Interestingly, there is a dramatic change in the mean temperature dependent magnetization and magnetic ordering temperature when the nanoparticles composition consists of 89%Fe and 11%Ni. This can be explained by the fact that the high magnetic moment Fe atoms (with an atomic spin moment of 2.22 μ_B) are replaced by low spin moment Ni atoms (with an atomic spin moment of 0.606 μ_B). In the case of Ni@Fe, there was a significant increase in magnetization below the temperature (450 K) at which magnetic ordering occurs.

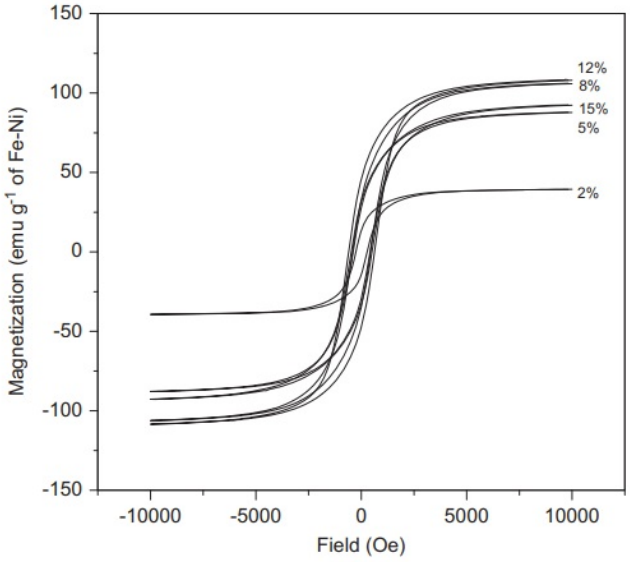

Figure 2.10: Hysteresis loop of the FeNi nanoalloys at room temperature (from [43])

Huaqiang Wu et al. [43] have investigated the magnetic properties of size-controlled FeNi nanoalloys attached to carbon nanotubes for magnetic storage and ultra-high density magnetic recording applications. A wet chemical method was used to synthesize FeNi alloy nanoparticles with average diameters ranging from 12 to 25 nm. The results of magnetic measurements, as depicted in Figure 2.10, indicate that the FeNi alloy nanoparticles attached to carbon nanotubes exhibit soft magnetic properties. The hysteresis loops were measured for samples with different FeNi to carbon ratios. A decrease in the size of the FeNi alloy nanoparticles results in a decrease in the saturation magnetization, which correlates well with the observed phenomenon of an increase in the saturation magnetizations from 2 to 12 at% followed by a decrease from 12 to 15 at%. This behavior can be explained by the increasing disorder of the magnetic moment orientation at different sites as the surface-to-volume ratio increases [44].

2.4.2 Structure of FeNi nanoparticles

FeNi nanoparticles can exhibit different structures on surfaces depending on various factors such as preparation method, surface chemistry and interaction with the substrate. FeNi nanoparticles can self-assemble on surfaces to form nanowires or nanorods, each wire consisting of many individual nanoparticles aligned along a common axis. The formation of nanowires can be influenced by the surface chemistry and the size and shape of the individual nanoparticles. They can form a continuous thin film on surfaces through processes such as sputtering or thermal evaporation. The structure of the thin film can be influenced by substrate temperature and deposition rate. In general, the bimetallic nanoparticles can form a core-shell or onion-like structure. The structural properties of FeNi nanoparticles have been studied using classical molecular dynamics combined with the Metropolis Monte Carlo free energy minimization method [45]. The absence of Ni atoms at vertex or edge sites suggests that these sites are more favorable for Fe atoms in the nanoparticles (see Figure 2.11). As the number of iron atoms increases, a complete Fe shell is formed. The additional Fe goes to the core and is homogeneously alloyed with Ni atoms. They named this structure quasicore shell structure. As the results show, whether the annealing process is gradual or abrupt, and whether they are molten or in a condensed state, the systems always evolve into the quasicore-shell structure.

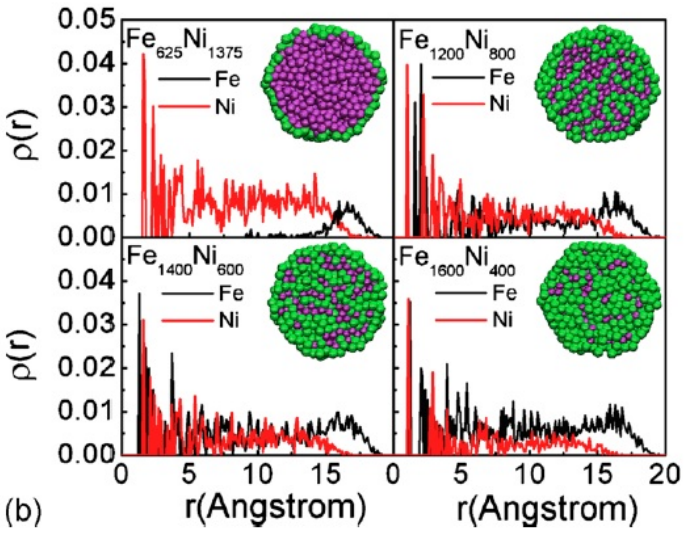

Figure 2.11: The radial distribution of nanoparticles containing 2000 atoms with different atomic compositions. The inset shows the cross-section of the corresponding nanoparticle (from [45])

FeNi nanoparticles have potential biomedical applications due to their magnetic properties. They can be used in magnetic hyperthermia therapy. Magnetic hyperthermia involves raising and maintaining the temperature of the target area between 42-44℃ for a period of time to ablate cancer cells without damaging normal cells [46]. Instead of using conventional superparamagnetic iron oxide nanoparticles, Xiyou Cui used ferromagnetic FeNi alloy as the encapsulated material in CNTs [47]. The results suggested that this nanostructure has the potential to be a promising cancer treatment. FeNi nanotubes with

a length of 12 µm, a diameter of 400 nm, and a wall thickness of about 120 nm were used to develop a device for precise drug and gene delivery [48].

FeNi nanoparticles exhibit good thermal stability and can withstand high temperatures, making them useful in high temperature applications.

2.5 Graphene: growth and structure

Carbon is the sixth element in the periodic table with four valence electrons. Three types of hybridization, specifically sp, sp^2, and sp^3, can be formed by the valence electron. A single layer of sp^2-bonded carbon atoms arranged in a honeycomb lattice is called a single layer graphene crystal. The carbon-carbon bonds in graphene are three inplane bonds, which are exceptionally strong and provide the rigid framework for the hexagonal lattice structure of graphene.

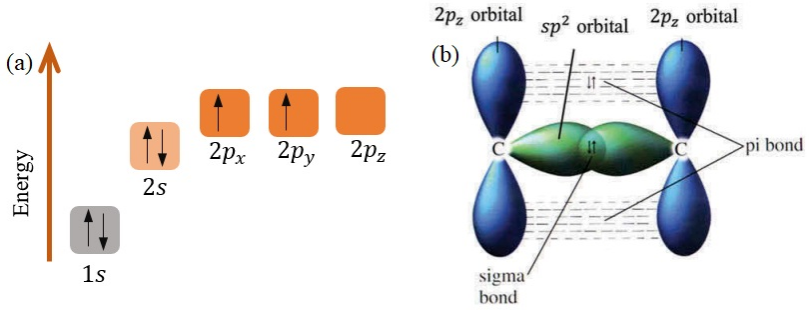

Figure 2.12: The energy levels of the outer electrons in carbon atoms, and the formation of σ and π bonds through sp^2 hybridization. Adapted from [49]

A π bond perpendicular to the planar structure is formed by the $2p_z$ orbitals as illustrated in Figure 2.12, while the sp^2 ($2s$, $2p_x$ and $2p_y$) hybridized orbitals form an in-plane σ bond. The partially occupied p_z orbitals are responsible for the electronic properties of graphene. The binding energy between carbon atoms within a single graphene layer is 4.3 eV. It is significantly large compared to the weak interlayer binding energy of 0.07 eV between two graphene layers [50]. The σ covalent bond in graphene is stronger than the sp^3 hybridized carbon-carbon bonds found in diamond, due to the shorter interatomic distance, resulting in the exceptional mechanical properties of monolayer graphene.

The unit cell of graphene consists of two carbon atoms. The primitive lattice vectors are

$$\vec{a}_1 = \frac{a}{2}(1, \sqrt{3}), \vec{a}_2 = \frac{a}{2}(1, -\sqrt{3})$$

where $a \approx 1.42$Å and both unit cell vectors a_1 and a_2 have an equivalent lattice constant of 2.46Å.

In each elementary cell of the honeycomb lattice there are two atoms belonging to two sublattices A and B. The three nearest neighbor vectors in real space are:

$$\vec{\delta}_1 = (0, \frac{a}{\sqrt{3}}), \vec{\delta}_2 = (\frac{a}{2}, -\frac{a}{2\sqrt{3}}), \vec{\delta}_3 = (-\frac{a}{2}, -\frac{a}{2\sqrt{3}})$$

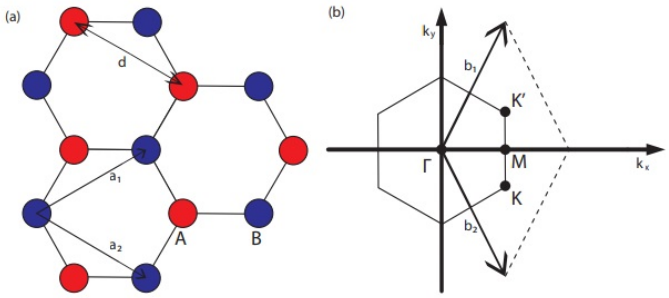

Figure 2.13: (a) A honeycomb lattice, the sublattices A and B. (b) Reciprocal lattice vectors and some special points in the Brillouin zone.

The reciprocal lattice of monolayer graphene is shown in Figure 2.13, where the arrows represent lattice vectors and the hexagon is the first Brillouin zone. The interlayer screening, band structure, and spin-orbit coupling of graphene films are strongly influenced by the different stacking orders of the planar structures in the honeycomb network [51–54]. There are three most common stacking orders: hexagonal or AA... stacking, Bernal or AB... stacking, and rhombohedral or ABC... stacking. Bernal stacking is the most common stacking arrangement and has the lowest energy in single crystal graphite [55]. The Bernal structure is formed by stacking two sheets on top of each other with a rotation of 60^0 of one sheet relative to the other.

The band structure of graphene consists of two overlapping energy bands, known as the valence band and the conduction band. It was first calculated by Wallace (1947) [56]. Figure 2.14 shows the result of a calculation of the band structure of graphene. These bands touch at six points in the Brillouin zone, called Dirac points, where the energy-momentum relation is linear; $E = \hbar k v_F$, similar to the energy-momentum relation for massless particles in relativistic quantum mechanics. Because of this linear dispersion relation, electrons in graphene behave like massless Dirac fermions, which have unique electronic properties such as high electron mobility.

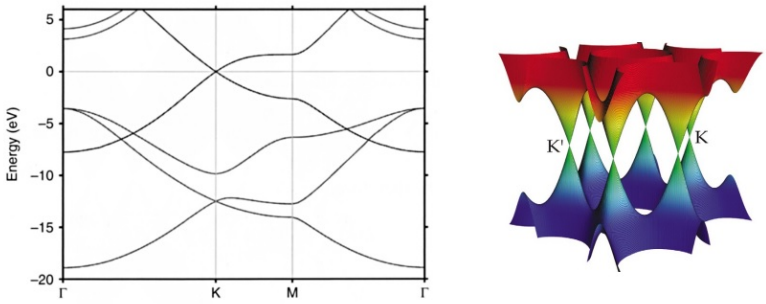

Figure 2.14: (a) The band structure calculation of graphene (from [57]). (b) The electron energy spectrum of graphene (from [58])

Graphene's exceptional electrical properties make it attractive for use in several fu-

ture electronic applications, including ballistic transistors, integrated circuit components, transparent conducting electrodes, and sensors. Graphene is also a good candidate for see-through electronic devices because of its high optical transparency [59]. Graphene is also interesting as a coating material. It can prevent the formation of oxides on the protected metal or provide effective surface resistance to hydrogen peroxide [60]. The performance of several promising electrode materials in electrochemical devices has been improved by the use of graphene. The prepared FeNi-doped and N-doped graphene can serve as a stable and efficient electrocatalyst for the oxygen reduction reaction process in acidic environments. This superior performance can be attributed to the strong attraction between the metal nanoparticles and nitrogen atoms with oxygen molecules and hydrogen ions, respectively [61].

2.5.1 The Moiré pattern

A Moiré pattern results from the interference between two mashes with slightly different lattice constants or angles. The hexagonal symmetry of the graphene lattice makes it particularly interesting for studying graphene growth on hexagonally packed transition metal surfaces and the consequent formation of the Moiré patterns [62, 63]. When graphene is placed on a metal surface, it can form a Moiré pattern due to the slight mismatch between the (111) hexagonal close-packed metal surface and the honeycomb structure of graphene. In crystallography, the notation 120^0 is usually used to describe two coincident hexagonal lattices. According to this notation, the real-space unit cell vectors are rotated by 120^0, while the reciprocal-space vectors are rotated by 60^0 relative to each other. Figure 2.15 illustrates the definition of grid vectors in both real and reciprocal space.

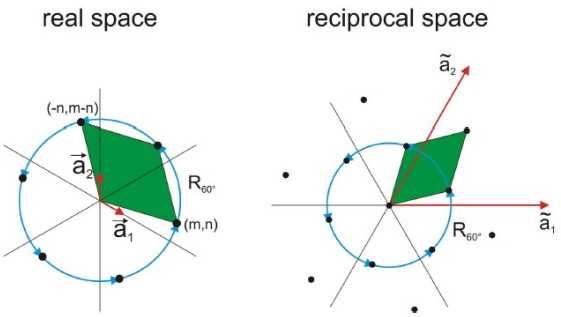

Figure 2.15: Definition of lattice vectors of a commensurate superstructure.

A unit cell vector of the Moiré supercell can be represented by the real space vector $\vec{v}_{\text{moiré}} = (m, n)$. Thus, the indexing of the Moiré pattern is given by $(m, n)_{TM}/(r, s)_g$. The Moiré pattern is caused by the alignment of the graphene lattice and the metal lattice, where the graphene lattice is rotated counterclockwise by an angle ϕ with respect to the metal lattice. The continuous rotation of the graphene lattice causes the first-order graphene-lattice frequencies to move in a circular motion in reciprocal space. The spatial beat frequencies of any first-order Moiré exhibit analogous circular trajectories. Using STM, one can obtain images of the surface in real space, which can be used directly to derive the unit cell. The disadvantage of STM data is that they usually suffer from drift

and piezo creep. Thus, obtaining lattice constants with an accuracy better than 10% error is a challenging task. Figure 2.16 shows an STM image of a graphene film on Ir(111) at a temperature of 300 K [64]. As a result, the lattice constant ratio of the graphene layer is $x = 1.108$ and it is rotated clockwise by -1.7^0 relative to the Ir lattice.

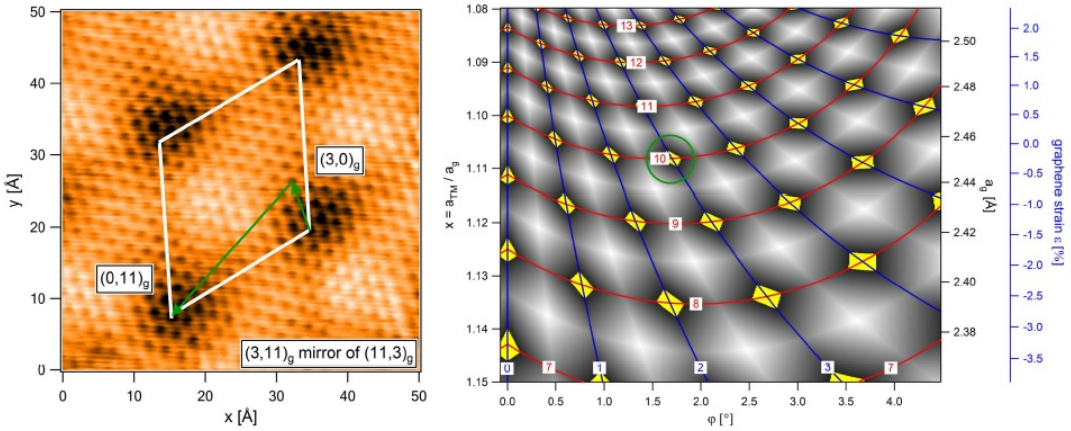

Figure 2.16: Moiré unit cell indexing from atomic resolution STM of graphene on Ir(111) at 300 K (from [64])

2.5.2 Preparation methods of graphene

Many interesting applications of graphene require the growth of a single layer of graphene on a suitable substrate and the creation of a controlled and practical bandgap. However, achieving this is quite challenging. There are numerous approaches to obtain high-quality single or multilayer graphene, including exfoliation, chemical synthesis, unzipping of nanotubes, thermal chemical vapor deposition, plasma-enhanced chemical vapor deposition, and decomposition of a SiC surface. This chapter explores graphene deposition through chemical vapor deposition (CVD), with a focus on the method employed to produce a monolayer of graphene on a cobalt thin film.

CVD is the process of depositing carbon atoms on a substrate through a chemical reaction in a controlled environment. The sample is heated to a controlled temperature in a chamber containing one of the hydrocarbon gases propylene (C_3H_6), ethylene (C_2H_4), methane (CH_4), or acetylene (C_2H_2). When the precursor gas encounters the heated substrate, the high temperature causes it to decompose into carbon and hydrogen atoms. The carbon atoms then diffuse and nucleate on the substrate surface, while the hydrogen is desorbed. The temperature depends on the selected hydrocarbon molecule and its corresponding binding energy.

CVD offers the ability to produce single layer or monolayer graphene by adjusting the temperature, while also facilitating the growth of graphene films or sheets on large area substrates. It allows scalability in the production process, and the growth parameters, including temperature, pressure, precursor concentration, and duration, can be easily controlled.

2.5.3 Graphene growth mechanism

The formation of graphene on metal surfaces is a catalytic process that occurs on the surface during chemical vapor deposition. Several transition metals have been used as substrates for the formation of graphene, either in single crystalline or polycrystalline structure [65]. The crystallinity of the metal plays a significant role in the formation of graphene as well as the resulting grain size. In addition, the surface roughness of the metal can also affect the formation of a homogeneous graphene film.

Nickel (Ni) is a well-known transition metal catalyst that exhibits segregation of carbon atoms on its surface when exposed to high temperatures. As a result, Ni nanoparticles and thin films are widely used as catalysts in the CVD process for the growth of carbon nanotubes.

2.5.4 Graphene on cobalt thin film

Graphene on Co(0001) exhibits structural properties very similar to graphene on Ni(111). The lattice constant of close-packed hexagonal Co is 250.71 pm, resulting in a lattice mismatch of less than 1%. This creates the potential for growing stable epitaxial layers without the formation of superstructure patterns. Like Ni, Co is a ferromagnetic metal (FM), which plays an important role in spintronic applications. However, the magnetic spin moment of Co is three times larger than that of Ni. Varykhalov et al. [66] used chemical vapor deposition (CVD) to fabricate graphene on bulk Co(0001)/W(110). The structural properties of graphene and Co were investigated by low-energy electron diffraction (LEED) and scanning tunneling microscopy (STM), as presented in Figure 2.17. Upon annealing, the Co layer on W(110) collapses into 3D islands, while the islands are

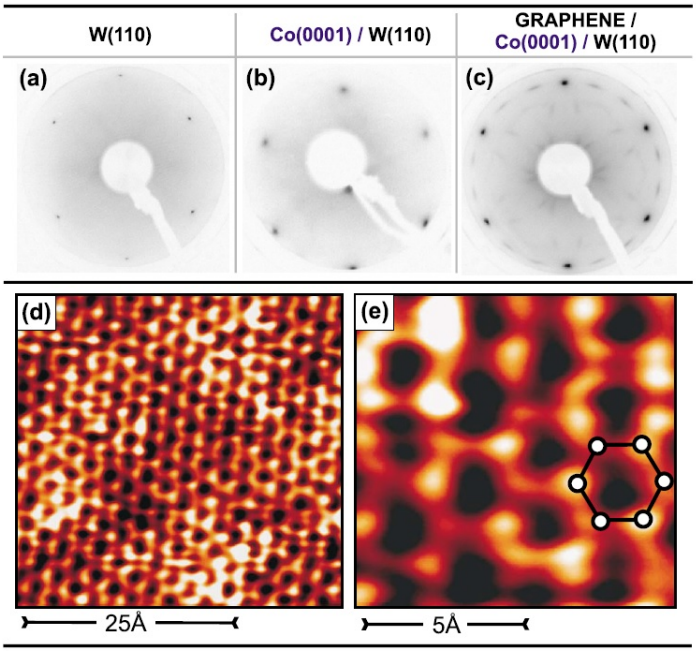

Figure 2.17: Structure of graphene on Co, LEED pattern of (a) W(110), (b) Co thin film on W(110), and (c) graphene/Co/W(110). (c and d) STM images of graphene (from [66])

separated by regions of W(110) substrate. The presence of straight monoatomic steps in the STM images and the LEED pattern clearly indicates the presence of W areas between the Co islands. After chemical vapor deposition at a temperature of 750 K, the LEED pattern suggests the presence of a graphene layer with domains that show a slight rotation relative to the Co lattice.

STM studies of this surface reveal the formation of graphene with a honeycomb structure. The high resolution STM image of graphene on Co shows triple symmetry, which is similar to the case of graphene on Ni.

3 Experimental background

In this chapter, the experimental setup and the procedures that will be used in this thesis work will be outlined.

In the field of surface science, it is important to have a clean surface free of any extraneous molecules that may interfere with the measurements or alter the properties of the nanoparticles. UHV chambers are designed to achieve extremely low pressures by removing gas molecules and contaminants from the environment. Nanoparticles are highly sensitive to their environment. Even trace amounts of gases and other contaminants can interfere with the accurate characterization and manipulation of nanoparticles on a surface. In addition, in an high-vacuum environment, nanoparticles are less susceptible to oxidation, decomposition, or other chemical reactions that can occur in the presence of reactive gases. UHV chambers are often equipped with various surface analysis techniques such as scanning tunneling microscopy (STM), X-ray photoelectron spectroscopy (XPS), and low-energy electron diffraction (LEED). These techniques require UHV conditions to obtain accurate and reliable data on the structure, composition and properties of nanoparticles on a clean surface.

3.1 Ultra high vacuum

Ultra-high vacuum (UHV) refers to a state of extremely low pressure and minimal molecular density, typically in the range of 10^{-7} to 10^{-12} mbar. Under UHV conditions, the pressure of residual gases and vapors is so low that they have little or no effect on material surfaces or processes taking place inside a vacuum chamber. The UHV pressure range has been achieved through the use of widely adopted processes and technologies. The reader is encouraged to consult the available literature [67, 68].

This section provides an overview of the experimental setup used to achieve the required vacuum level. The system consists of two main UHV chambers: the preparation chamber and the analysis chamber. Figure 3.1 shows a schematic projection in the horizontal plane.

Each chamber is equipped with a set of four vacuum pumps. A combination of a turbo molecular pump ($hiPace700$) and a two-stage rotary vane pump is used for pump-down and high gas load operation. When the two turbo pumps are off, the ion getter pump ($IGP, Starcell300$) effectively maintains the base pressure without causing disruptive vibration. The Titan sublimation pumps help reduce the presence of gases in the chamber, resulting in a cleaner and more stable vacuum environment. They are particularly useful for removing gases that cannot be effectively evacuated by other vacuum pumps. However, during measurements, it is important to turn off the TSPs to prevent titanium vapor from reaching the sample. The titanium vapor released can contaminate the sample under test. A Bayard-Alpert hot cathode ion gauge is installed in each chamber to measure the

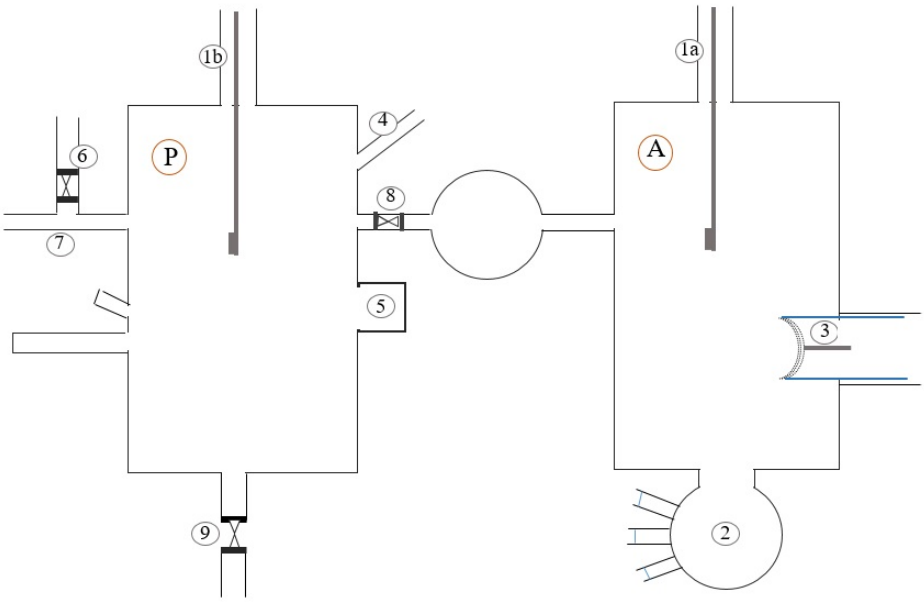

Figure 3.1: Schematic projection to the horizontal plane of the UHV system's main chambers: A analysis chamber, P preparation chamber, 1 main manipulators, 2 STM, 3 LEED/AES, 4 triple evaporator, 5 electron bombardment heater, 6 load lock with magnetic transporter, 7 magnetic transporter for interchamber transport, 8 gate valve to separate chambers, 9 connection to magnetron sputtering source.

pressure. There is a gate valve in each chamber that can isolate the chamber from its turbopump. A Vacuum Generators manipulator is installed in each chamber with a built-in sample heater and Type K thermocouples for temperature measurement. Samples are transferred between the manipulators and other instruments using magnetic transporters and wobble sticks.

The preparation chamber is equipped with a triple rod evaporator (EMF 3T, Omicron) and a gas inlet for thin film preparation. To achieve a clean substrate, there is a sputtering gun and an electron bombardment heater when temperature above 900 °C is required. The analysis chamber is equipped with surface analysis tools such as LEED/AES (SpectaLEED, Omicron) and STM (MicroSPM, Omicron).

3.2 Low energy electron diffraction

Low Energy Electron Diffraction (LEED) is a technique used to analyze and characterize a surface structure. It involves directing a beam of low energy electrons onto a sample surface and analyzing the diffraction pattern formed by the scattered electrons. LEED provides valuable information about the atomic arrangement and surface symmetry of crystalline materials.

In LEED, a beam of low energy electrons, typically in the range of 30-200 eV, is directed at the sample surface. This energy is approximately equal to the minimum inelastic mean free path length required to achieve maximum surface sensitivity. However, the standard setup is depicted in Figure 3.2, uses an electron gun, such as a heated filament or field emitter, to generate a beam of low energy electrons. The electron beam is accelerated

by an electric field and then passed through a series of adjustable lenses that help shape and focus the electron beam into a narrow, collimated beam. The beam is diffracted at a sample. A detector system, such as a hemispherical fluorescent tube with a set of four grids, is positioned to capture the scattered electrons.

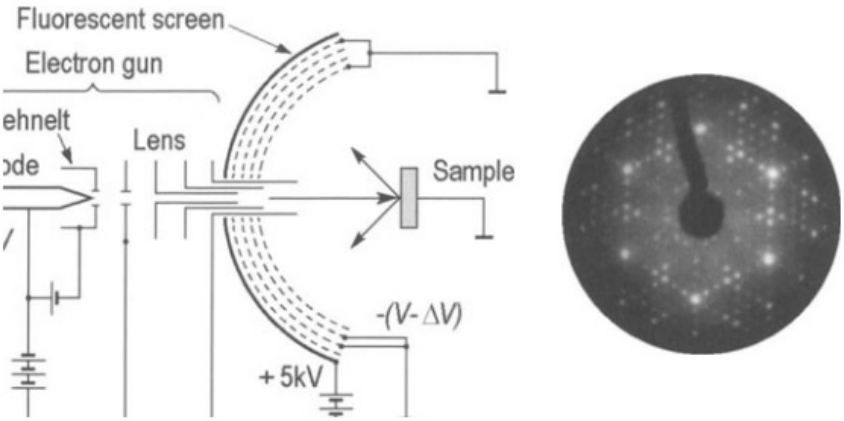

Figure 3.2: Schematic of standard four-grids LEED setup (from [36])

The first (innermost) grid is connected to ground, ensuring that there are no electric fields in the space between the sample and the screen. The second and third grids, called suppressor grids, are set at a negative potential to repel low energy electrons resulting from inelastic scattering. The fourth grating is grounded to shield against the high potential of the fluorescent screen, allowing the elastically scattered and diffracted electrons to be accelerated to a high energy level as they pass through the suppressor grids. This acceleration induces fluorescence in the screen, and the resulting diffraction pattern can then be observed on the screen.

The elastically scattered electrons must fulfill the conditions

$$\vec{k} - \vec{k}_0 = \vec{G}_{hkl}$$

$$|\vec{k}| = |\vec{k}_0|$$

where $\vec{k}$ is the diffracted wave, $\vec{k}_0$ is the incident wave and $\vec{G}_{hkl}$ is a reciprocal vector of the crystal lattice.

In the typical energy range used in LEED, the electrons have a wavelength (about $1 - 2$Å) that satisfies the atomic diffraction condition, where the wavelength is on the order of or smaller than the interatomic spacing. As a result, LEED mainly provides information about the two-dimensional atomic arrangement of the sample surface.

LEED pattern

The diffraction pattern in LEED arises from the scattering of electrons at specific angles, which are determined by Bragg's Law. According to Bragg's Law, for constructive interference to occur, the path difference between two scattered electrons from adjacent atomic planes must be an integer multiple of the electron's de Broglie wavelength. This condition gives rise to specific diffraction spots in the LEED pattern. Analyzing a LEED

pattern involves interpreting the diffraction spots to extract information about the crystal structure of the surface. If the diffraction pattern were obtained from an ideal crystal surface, perfectly rigid and infinitely stretched, and measured with a perfect instrument, the diffraction spots would appear perfectly sharp. The intensities of the spots in the pattern are related to the scattering amplitudes of the electrons and the arrangement of the atoms on the surface. The presence of structural defects and imperfections in the crystal lattice causes the diffraction spots to broaden and the background intensity to increase. If no spots are observed in the LEED pattern, it indicates that the surface may be disordered, amorphous, or composed of finely dispersed polycrystalline structures.

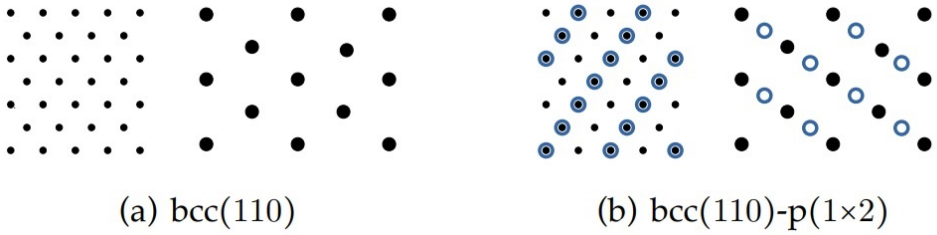

Figure 3.3: Different surfaces in real space and LEED patterns.

As mentioned above, the LEED pattern is a reciprocal representation of the surface lattice. A simple crystal structure such as bcc(110) can be easily translated (see Figure 3.3), while there are more complicated superstructure patterns. Identifying a superstructure based on a given LEED pattern can be quite challenging because there may be several similar structures.

The LEED system does not require the calibration process, but it does require some consideration. To prevent charging, each substrate was grounded and the central spot of the electron gun was blocked in all images. The energy of the incident electron beam was specified for each LEED image taken and the beam was aimed at the center of the substrate. Sharp spots were obtained by adjusting the lens voltages.

The patterns were captured with a digital camera. ImageJ software was used to crop, adjust brightness, convert to grayscale, and invert the images. Blurriness in the images is primarily due to camera shake or improper focusing, unless otherwise noted.

3.3 Scanning tunneling microscopy

Scanning Tunneling Microscopy (STM) is a powerful imaging technique used to visualize surfaces at the atomic scale. STM was first developed in the 1980s by Gerd Binnig and Heinrich Rohrer and has since become a widely used tool in the fields of materials science, nanotechnology, and surface science. This section outlines the basics of a scanning tunneling microscope.

The STM works by scanning a sharp metal tip across a surface of interest, typically a conductive material such as a metal or semiconductor. The basic principle of the STM is the quantum tunneling effect (Figure 3.4). The fine tip is brought very close to the surface of a conductive sample. The tip and sample are biased with a voltage difference,

creating an electric field between them. When the voltage is applied, electrons can tunnel between the tip and the sample. This occurs within tip-sample gaps of $5 - 10$Å. The tunneling current density is given by:

$$j = \frac{D(V)V}{d} \cdot \exp(-A\Phi_B^{\frac{1}{2}}d)$$

where d is the tunneling gap, Φ_B is the effective barrier height of the gap. $D(V)$ are the electron state densities, and A is a constant factor [36]. The tip is held at a very small distance (typically a few Å) from the surface by a feedback mechanism that adjusts the height of the tip based on the tunneling current. The tunneling current is extremely sensitive to the distance between the tip and the surface, making it possible to map the surface topography with atomic resolution.

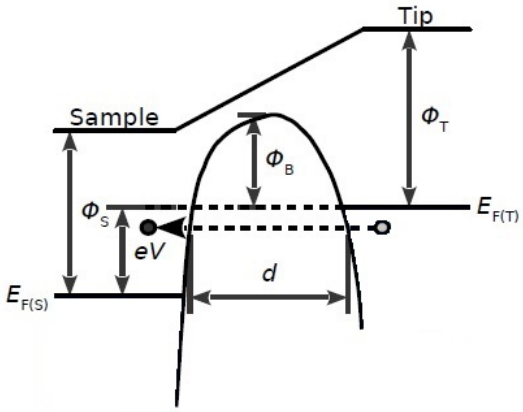

Figure 3.4: Energy diagram of STM tip and metallic sample tunneling. Adapted from [36]

Resolution in STM is determined by several factors. One is the precise position of the STM tip relative to the sample surface. Piezoelectric ceramics provide this precise control. They are capable of converting electrical signals in the range of 1 mV to 1 kV into mechanical motion in the range of sub-angstroms to a few microns. Various sources of noise, such as thermal fluctuations, electronic noise, and vibration noise, can degrade the resolution. To ensure stable operation of the STM, it is essential to limit changes in tip-sample separation caused by vibration to less than 0.01 Å. Techniques such as damping systems are used to reduce mechanical vibrations. By carefully optimizing these factors and employing advanced techniques, STM can achieve atomic-scale resolution, allowing it to reveal the spatial arrangement of atoms by capturing the variations in electron density associated with their positions. STM can also be used to image the electronic structure of surfaces by measuring the local density of states (LDOS) of surface electrons. By analyzing the tunneling current as a function of tip position and voltage, STM can reveal detailed information about the electronic properties of surfaces, such as the band structure and distribution of surface states. One of the major advantages of STM is its ability to image surfaces under ambient conditions, allowing materials to be studied in their native environment. STM can also be used to study a wide range of surfaces, from single atoms to complex nanostructures, and has been used to investigate the properties of materials in fields such as catalysis, surface chemistry and nanoelectronics.

In constant height mode, the tip is held at a fixed distance from the sample surface and the tunneling current is allowed to vary as the sample is scanned. This mode is useful for imaging the topography of the sample because the distance between the tip and the surface is kept constant, allowing a more accurate representation of the surface topography. One of the advantages of using the constant height mode is the ability to acquire images quickly. It is less susceptible to interference from external noise sources, such as vibration or electromagnetic fields, because the tunneling current is allowed to vary. However, in this mode, the tunneling current can become very large when the tip encounters high points on the sample surface, which can cause the tip to crash into the sample and potentially damage it.

In constant current mode, the tunneling current is kept constant by adjusting the height of the tip as it scans the sample surface. This mode is useful for imaging the electronic properties of the sample because the tunneling current is proportional to the local density of states (LDOS) of the sample. The feedback mechanism adjusts the height of the tip to maintain a constant current, resulting in a three-dimensional map of the surface topography with atomic resolution. In this mode, the distance between the tip and the surface is not kept constant, which can result in some distortion of the surface topography due to changes in tip-sample distance.

An STM image is the result of a combination of the surface topography and the shape of the microscope tip. When the tip is blunt, the surface features become less distinct or blurred. In the case of a multi-tip, where the tip has multiple ends, each surface feature may appear multiple times corresponding to each tip end. Detecting such a condition can be difficult and in some cases impossible.

Multi-tips pose a significant challenge when imaging high aspect ratio surfaces, such as individual nanoparticles on a flat surface. Figure 3.5 provides an illustration of a multi-tip issue, which becomes evident in STM image of nanoparticles deposited on a surface. This is because the presence of multiple tips can lead to complex interactions between the tips and the surface features. However, when imaging a flat surface, a multi-tip may not have a significant impact. This is because the longest tip is always positioned close to the surface, while the secondary tips are positioned further away. Due to the exponential dependence of the tunneling current on distance, the effect of the shorter tip is relatively small.

Various methods have been used to improve the sharpness of STM tips, but the details of these techniques will not be discussed in this context.

The presence of adsorbates on the sides of a tip can present an additional challenge. This can lead to intermittent tunneling behavior as the tip approaches a steep object, such as a nanoparticle, resulting in significant vertical oscillation of the tip.

As many STM users can attest, STMs are prone to drift. Drift refers to the gradual movement or displacement of the microscope tip during imaging, resulting in distorted images along one or more axes. These drifts become more pronounced and noticeable when there are large changes in position in the respective directions. For example, after large movements in the X direction, the X drift becomes particularly strong, causing distortion along the X axis. Similarly, large position changes in the Y direction result in more Y drift and distortion along the Y axis. After a few scans at a particular position, the drift, along with the associated image distortion, will gradually decrease and eventually

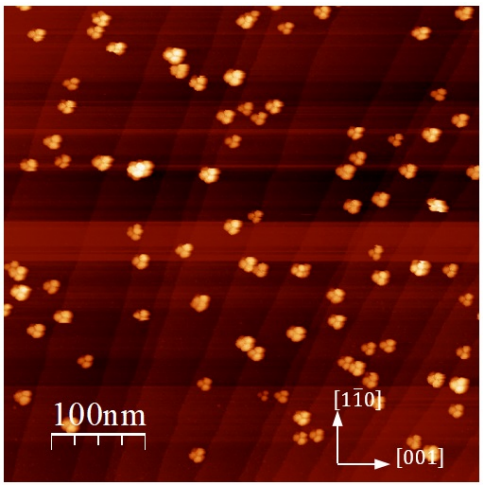

Figure 3.5: Images of FeNi nanoparticles on W(110), multi tip, 1.0 V, 0.8 nA.

disappear. It is important to note that Z-direction drift is very difficult to detect during the scanning process and is typically observed during post-measurement evaluation.

During the imaging process in scanning techniques, both mechanical vibration and electronic noise can have an impact. These factors can introduce unwanted signals and affect the quality of the acquired images. Mechanical vibrations can be caused by various sources, such as nearby equipment, building vibrations, or even the operation of the microscope itself. These vibrations can manifest themselves as periodic signals in the spatial domain due to the scanning process. To minimize their effects, two sets of dampers are typically used to reduce mechanical noise. In addition, efforts are made to eliminate or isolate vibration sources whenever possible. For example, turbopumps and booster pumps should be turned off, and booster pumps in adjacent laboratories may be placed on steel springs to minimize their contribution to vibration.

Electronic noise is generated by the electronic components and circuits in the microscope and controller. Several measures are taken to reduce electronic noise. Filters are used to reduce unwanted frequencies, ground loops are minimized to prevent interference, and shielding is used to reduce external electromagnetic influences. Together, these measures aim to reduce electronic noise and maintain the integrity of the acquired data.

It is important to consider the coarse position when evaluating STM images. Unlike the fine position, which moves along the X, Y, and Z axes, the coarse position moves along the R, θ, and Z axes. This means that any lateral movement will result in a slight rotation. The coarse XY motion is limited to a circular area 6 mm in diameter, which limits the rotation of the sample to approximately $\pm 6.7°$. In addition, the substrate itself may have a slight rotation with respect to its holder. By changing the coarse position, different areas of the substrate can be scanned. It is important to note that different areas of the sample may yield different results depending on the homogeneity of the sample treatment. When analyzing the orientation of surface structures, the rotation of the sample must be taken into account. The crystal surface axes shown in the images are aligned without considering these effects. It should be noted that while the tungsten crystal itself is mostly in perfect condition, there may be some areas with scratches that hinder imaging. Therefore, images were only taken when tungsten step edges were identified. The etched

tungsten tips were used for imaging and each STM image presented in this thesis will include information about the gap voltage and tunneling current.

STM data evaluation

This subsection outlines the typical steps involved in processing an STM image. The STM images are analyzed using WSxM and Gwyddion. The first step in processing an STM image is to perform plane or facet levelling to compensate for the tilt of the substrate relative to the STM. A simple way to determine the height of nanoparticles is to draw a profile line across a selected nanoparticle and measure the height difference between the substrate and the peak of the nanoparticle. It is important to draw the profile line in the fast scan direction, and the substrate should be flat and level around the nanoparticle. The profile must accurately intersect the peak of the particle, which requires careful selection of the peak position of the nanoparticle. The average elevation of the substrate must be determined from a single profile.

The faster method for processing the nanoparticles is Gwyddion's automated grain analysis. This method divides the height data of an entire image into two classes. Areas with high data values are assumed to correspond to particles. While this method works effectively on flat surfaces, it can fail on highly curved surfaces. To overcome this, extensive flattening is required, often accomplished by low-order polynomial background subtraction. The Mark by Otsu method provides several parameters for the detected grains. To calculate the height of each nanoparticle, the average surface elevation is subtracted from its maximum height.

The error bars of this method are determined by the root mean square elevation of the substrate. In cases where nanoparticles are close together, they may be detected as a single grain. Manual splitting of grains is the standard solution to this problem and is not overly time consuming. Analysis of the single monolayer high islands formed after melting the nanoparticles is essential and requires several steps.

The first step is to determine the area A of a given island using a technique called thresholding or flooding. In this technique, pixels or regions with values above the specified threshold are marked or highlighted, while those below the threshold are considered background. It becomes possible to extract and analyze specific regions or structures of interest within an image, such as the single monolayer high islands. Once the surface area is obtained, it can be converted into a number of atoms. Surface density can be estimated by considering pseudomorphic growth on the W(110) surface. This means that the number of atoms per unit area in the island is equal to the number of surface atoms on the W(110) surface. Fe and Ni atoms are smaller than W atoms. Consequently, the surface density of these atoms is expected to be greater than or equal to that of W(110). The total number of atoms in a given island must be converted to the corresponding volume:

$$V = n_{atom} \cdot \frac{M}{\rho}$$

where M is the atomic weight. Finally, the volume can be converted to the diameter of a nanoparticle.

$$V = \frac{4\pi}{3} \cdot \frac{d^3}{2}$$

In some cases, islands were observed to be accompanied by a nanoparticle. To estimate the volume of the nanoparticle, its apparent height was taken into account. In addition, the equivalent diameter was calculated by considering the combined volume of the island and the nanoparticle. By considering these factors, a more comprehensive understanding of the size and properties of the island-nanoparticle system can be obtained.

3.4 Transmission electron microscopy

Transmission electron microscopy (TEM) is a type of microscopy that uses a beam of electrons passed through a thin sample to produce a magnified image of the sample's internal structure. The basic principle of TEM is that a beam of electrons is emitted from an electron source, typically a heated filament or field emission gun, and focused onto the sample by a series of electromagnetic lenses. The sample is typically a thin film or small particle that has been cut and polished to a thickness of a few hundred nanometers or less. After passing through the sample, some of the electrons are absorbed or scattered by the atoms in the sample, while others pass through with little or no interaction. The electrons that pass through the sample are then focused through a series of lenses onto a fluorescent screen, or detector, which produces an image of the sample.

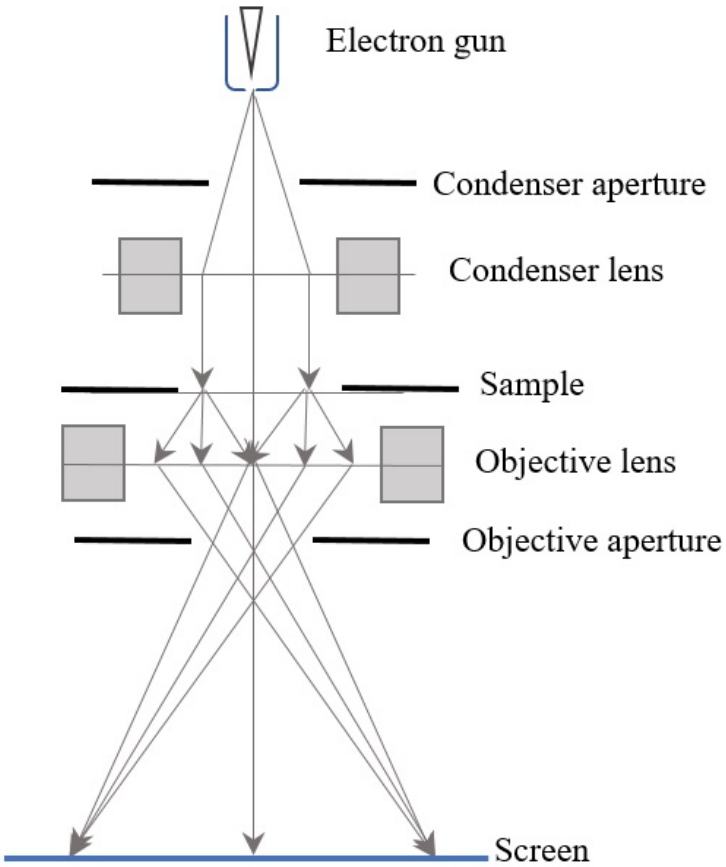

Figure 3.6: Image formation in TEM

Scattering within a sample causes a partial loss of intensity in the electron flux as it

passes through. This loss of intensity is more pronounced in thicker regions or regions containing higher atomic number elements. By effectively blocking the scattered electrons with the objective aperture, the thicker regions and those with higher atomic numbers appear dark in the image; using a smaller aperture increases contrast but results in a loss of resolution. The high magnification and resolution of TEM images make it possible to observe details of the sample at the atomic level. The principle of TEM imaging is shown in Figure 3.6.

High-resolution transmission electron microscopy (HRTEM) is a specialized technique within the field of transmission electron microscopy (TEM) that allows the observation of atomic-scale details with exceptional clarity and resolution. HRTEM allows the visualization of individual atoms, crystal lattice structures, and defects in materials. The wavelength of the electrons used in HRTEM is much smaller than that of visible light, allowing for higher resolution imaging. The de Broglie wavelength of electrons depends on their energy, and high-energy electrons (typically in the range of 100-300 keV) have smaller wavelengths, allowing for better spatial resolution. HRTEM uses magnetic lenses and correctors to minimize aberrations and improve beam convergence. By achieving a small, tightly focused beam, resolution is increased. High-resolution imaging requires ultrathin samples with minimal defects or contamination. Thinning the sample reduces the amount of material through which the electrons must pass, allowing for improved resolution. As depicted in Figure 3.7, we can observe a high-resolution image captured using a conventional transmission electron microscope (TEM) operating at a relatively high beam energy of 400 keV. The image highlights the presence of a single AgI nanoparticle resting on a carbonaceous support. The nanoparticle's positioning ensures that the electron beam is parallel to the [110] zone axis, an alignment corroborated by the Fast Fourier Transform (FFT) displayed as an inset. The nanoparticle takes on a truncated octahedral form, featuring well-defined [100] and [111] facets. Cross-sectional TEM

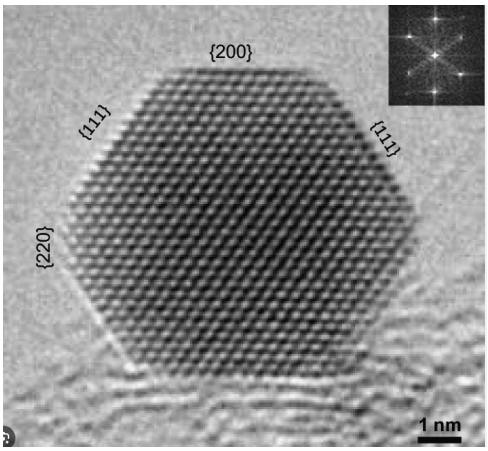

Figure 3.7: A high-resolution TEM image of a nanoparticle composed of AgI, with the inset depicting the Fast Fourier Transform (FFT) of the same nanoparticle (from [69])

imaging is commonly used to study buried interfaces. The sample is cut perpendicular to the surface and thin slices are prepared by chemical etching or ion milling. Using high-resolution TEM, it is possible to produce images that reveal the atomic structure of the sample.

Sample preparation for TEM imaging can be difficult and time-consuming because the sample must be thinned to a thickness of a few hundred nanometers or less. The electron beam can damage the sample over time, especially when imaging organic or biological materials. In this work, we deposited $Fe_{1-x}Ni_x$ on the carbon-coated lattices and analyzed the crystal structure of the nanoparticles using HRTEM microscopy.

3.5 Energy dispersive X-ray spectroscopy

Energy dispersive X-ray spectroscopy (EDS or EDX) can be performed using a transmission electron microscope (TEM), including high-resolution transmission electron microscopy (HRTEM). In high-resolution transmission electron microscopy (HRTEM), a high-energy electron beam is passed through a thin sample and the electrons interact with the atoms in the sample. Figure 3.8 shows a schematic representation of this electron-atom interaction. As the electrons interact with the atoms, they can either be scattered or absorbed by the atoms. If an electron is absorbed, it can knock out an inner-shell electron of the atom, creating a vacancy in the inner shell. The vacancy can be filled by

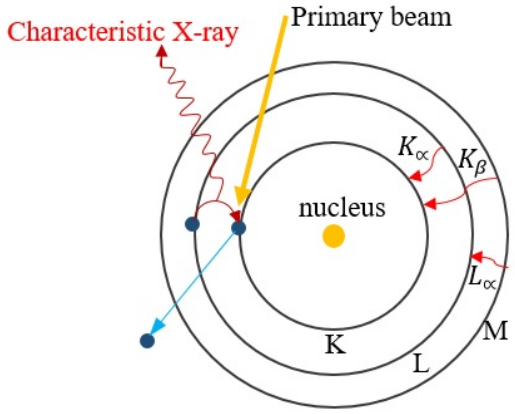

Figure 3.8: Principle of energy dispersive X-ray.

an outer-shell electron, resulting in the emission of an X-ray. The energy of the emitted X-ray is characteristic of the element in which the vacancy was filled. The emitted X-rays are detected by an energy dispersive detector placed in the column of the microscope. The detector records the energy and intensity of the X-rays emitted by the sample. The energy dispersive detector measures the energy and intensity of the X-rays emitted by the sample and produces a spectrum that shows the characteristic X-ray peaks of the elements present in the sample. The spectrum provides information about the elemental composition of the sample and allows the identification of the elements present. It is worth noting that when an atom in an excited state containing a hole transitions to its ground state, there is a possibility of emitting an Auger electron instead of the characteristic X-ray radiation. As the atomic number increases, the probability of emitting characteristic X-rays also increases. Therefore, EDS becomes more useful for heavy elements, especially at low abundances.

To generate an elemental map, the electron beam is scanned across the sample surface. At each point, the EDS detector records the X-ray signals, allowing for the simultaneous acquisition of elemental spectra for multiple points. The acquired elemental spectra are assigned to their respective spatial positions, creating a map that visualizes the distribution of elements across the sample surface.

Figure 3.9 shows the elemental mapping image of core shell Co-Ni. HRTEM allows the

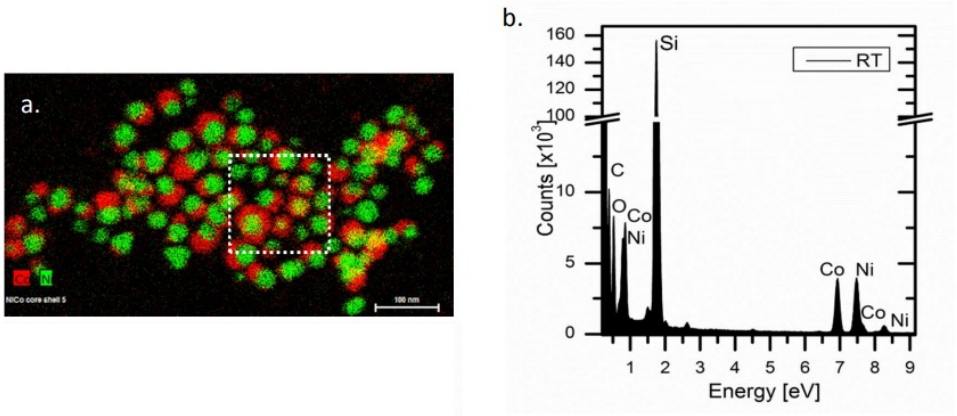

Figure 3.9: EDS elemental map (a) of Ni-Co core-shell nanoparticles (NPs) with corresponding spectrum (b) from the marked area in (a) (from [70])

sample to be viewed at atomic resolution, which means that the composition of individual atoms or atomic columns can be identified using EDS. HRTEM-EDS can be used to study the elemental distribution in complex materials, such as alloys or semiconductor heterostructures, and can provide information on the chemical bonding of the sample at the atomic level. The analysis time of HRTEM-EDX can be long, especially for complex samples, which can lead to electron beam damage and sample degradation.

3.6 Electron energy loss spectroscpy

Electron energy loss spectroscopy (EELS) is a technique used in transmission electron microscopy (TEM) to examine the contents of a sample. EELS was originally developed in the mid-1940s by James Hillier and RF Baker. However, it was not widely used for about 50 years after its development. Recently, due to the high performance detectors and energy filtering system installed on the electron microscopes, EELS has attracted much attention for new applications. In this section, the principle and application of EELS spectrum will be explained.

As mentioned in the last section, the electrons passing through a sample can be divided into two different groups: the first group consists of transmitted and elastically scattered electrons, while the second group consists of electrons that undergo inelastic scattering as a result of their interaction with the sample. The typical energy loss process can be described as follows: Lattice vibration (phonon excitation), less than 0.1 eV. Interband transition, less than 10 eV. Inner shell electron excitation, more than 13 eV. Collective excitation of valence electrons (plasmon excitation), less than 30 eV. Free electron excitation, less than 50 eV. Bremsstrahlung (emission of continuous X-ray).

As an example, the energy-loss spectrum obtained from an iron oxide particle is shown in Figure 3.10 There is a sharp peak on the left side of the spectrum, called the zero-loss

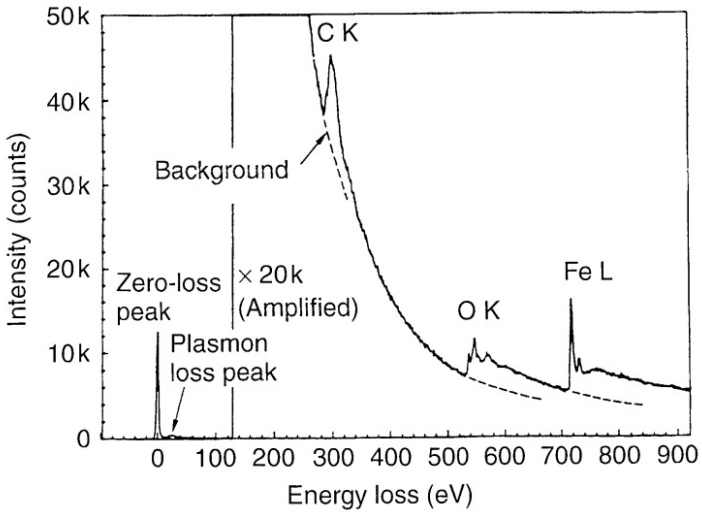

Figure 3.10: Energy loss spectrum of an iron oxide particle (from [71])

peak. When an incoming electron interacts with an atomic nucleus, the large mass difference between the electron and the nucleus results in a minimal energy exchange and falls below the detectable range of the EELS. This interaction contributes to the appearance of the zero loss peak. Near the zero loss peak there is a distinct peak due to plasmon excitation. Plasmon excitation results from the interaction between incident electrons and the delocalized outer-shell electrons, leading to the displacement of the outer-shell electrons and the subsequent creation of positively charged holes. The attractive force exerted by these holes contributes to the energy loss of the incident electrons. Within a higher energy loss region, the peaks in the energy loss spectrum are due to inner shell excitation of the constituents present in the microgrid supporting the sample, namely oxygen, iron, and carbon. The inner shell excitation process is typically associated with significantly higher energy loss. This is because the binding energies of the core-shell electrons are typically in the range of hundreds to thousands of electron volts. If an incident electron transfers sufficient energy, it can excite a core-shell electron from its initial core level to an unoccupied state above the Fermi level. By analyzing the energy values and intensity distribution of these two peaks, it is possible to identify the elements present and determine the composition of the sample. The interband transition does not show distinct peaks in the spectrum, it has a significant impact on the low energy loss region, but its information can still be obtained. Detecting the signal from phonon excitation is also challenging using a conventional spectrometer with an energy resolution of approximately 1 eV. Free electron excitation and Bremsstrahlung do not produce distinct peaks in the spectrum. Instead, they contribute to the background signal. To achieve high energy resolution and signal-to-noise ratio in TEM-EELS analysis, it is essential to have a high current density and a small kinetic energy distribution of the TEM electron source. A higher current density provides a better signal-to-noise ratio, while a smaller kinetic energy distribution improves energy resolution.

To gather electron energy loss spectra, an essential component is a spectrometer

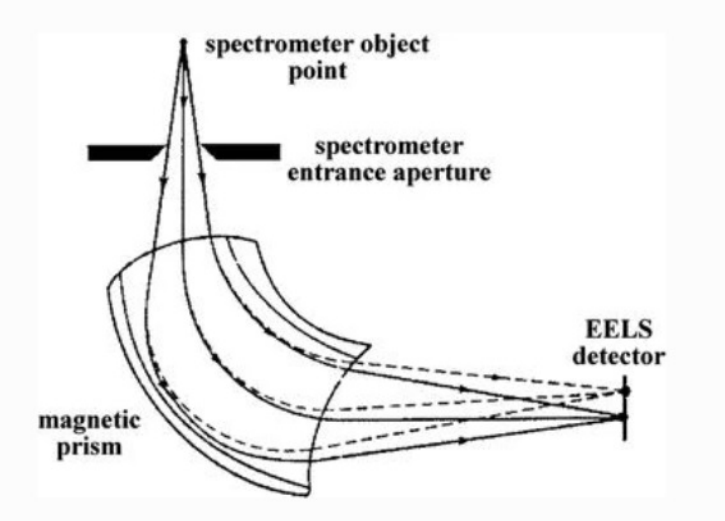

Figure 3.11: Schematic of the geometry of the EELS spectrometer and the electron trajectory (from [72])

unit, often positioned beneath the imaging column of a transmission electron microscope (TEM). At the heart of this unit lies a magnetic prism, as depicted in Figure 3.11. Within the prism, a uniform magnetic field is generated via an electromagnet. The Lorentz force causes electrons traversing the prism to disperse, ultimately leading to the formation of an energy loss spectrum, which is then captured by a detector.

In advanced EELS analysis, monochromators can be used to further reduce the energy distribution of the electron source, improving energy resolution to about 0.2 eV. The spectrometer unit, located below or inside the TEM imaging column, is critical to the acquisition of electron energy loss spectra. It consists of a magnetic prism that generates a uniform magnetic field via an electromagnet. The prism separates the electrons passing through it by the Lorentz force, forming an energy loss spectrum. The spectrum is detected by a charge-coupled device (CCD), usually located in the energy-dispersive plane. An energy-dispersive mechanical slit can be used to select the energy loss.

EELS can be used to study a wide range of materials, including semiconductors, metals, and biological samples. One of the major advantages of EELS is that it provides complementary information to other TEM techniques, such as high-resolution imaging and diffraction. However, EELS requires careful sample preparation and imaging conditions because electron beam damage can alter the electronic structure of the sample.

3.7 Magnetron sputtering source

The magnetron sputtering source, also known as the Haberland source (Figure 3.12), was first used by Haberland [73]. The cluster source consists of a magnetron sputtering system and an aggregation region. The magnetron can be operated in either DC or radio frequency (RF) mode, allowing to produce nanoparticles or nanoclusters of various materials in the nanoscale range. In DC mode, metallic or conductive clusters can be produced, while RF mode is required for insulator or semiconductor materials to prevent charging. A dense plasma is generated inside the magnetron by sustained electrical discharge in an

argon gas environment. The plasma contains positively charged argon ions that are accelerated toward the target surface. When these ions collide with the target material, they transfer momentum and energy, causing atoms or small clusters of atoms to be ejected from the target. The atoms condense and aggregate in the plasma to form nanoclusters. Nanoparticle growth within the aggregation region is influenced by diffusion and drift mechanisms. Diffusion occurs due to the elevated pressure, which promotes nanoparticle formation through collisions. Drift, on the other hand, is induced by the gas flow originating from the gas inlets and flowing toward the expansion nozzle. The growth process stops when the nanoparticles are carried away by the gas flow.

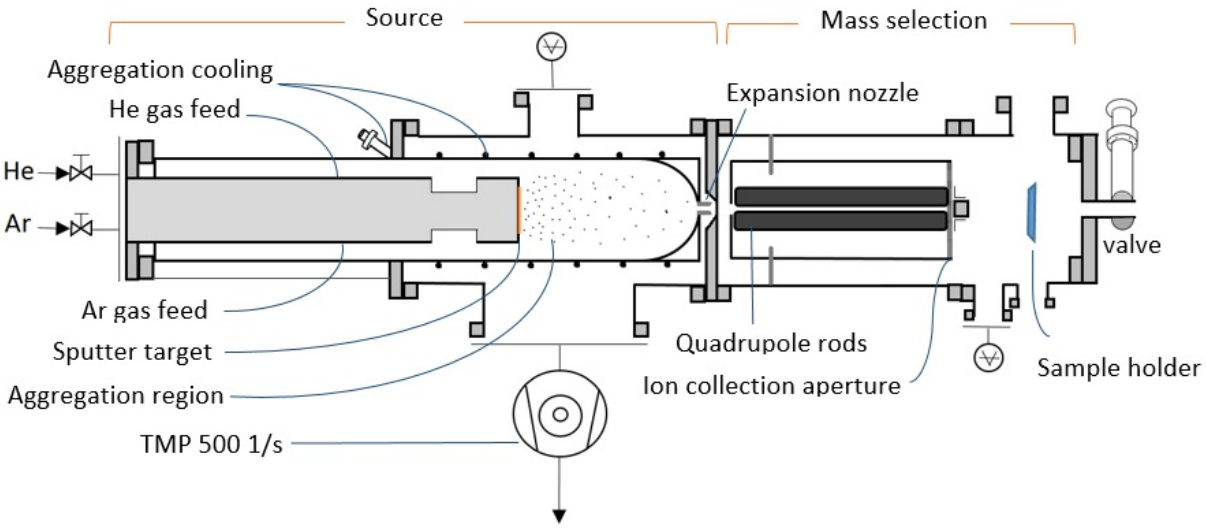

Figure 3.12: Schematic view: Magnetron sputtering source NCU200U and quadrupole mass filter QMF200.

The performance of the nanocluster source and the properties of the nanoparticles leaving the nozzle have been studied by several groups. Kousal et al. [74] have studied the charge and velocity of nanoparticles produced by a gas aggregation source, using the combination of TEM micrograph and and electrostatic deflection setup. The velocity of the nanoparticles was found experimentally to be 30-200 $m \cdot s^{-1}$ depending on their size, in agreement with the simulations. They also found that most of the initial charge is typically dissipated or lost in the afterglow parts of the plasma. Smirnov et al. [75] studied charged clusters after an aperture of the magnetron chamber both experimentally and theoretically. They found that the magnetron cluster plasma exhibits non-equilibrium evolution, leading to increased cluster density near the orifice and the formation of a unipolar plasma. Optimizing the chamber design, wall voltages, and orifice shape can increase the cluster yield from the magnetron plasma. Understanding and controlling these processes can improve the performance of the cluster source.

3.7.1 Sputtering process

Sputtering is a process in which atoms or molecules are ejected from a solid surface when it is bombarded with energetic particles, typically ions. It is commonly used in

various fields such as thin film deposition, surface modification, and the fabrication of microelectronic and optical coatings. Ions from a plasma or gas are accelerated toward the target material. When these ions collide with the target surface, they transfer energy and momentum to the atoms or molecules in the surface layer. To effectively sputter a substrate, their kinetic energy must exceed the binding energy of the substrate, typically by a factor of 10 to 100. The pressure in the chamber determines the mean free path of the sputtering ions. Therefore, the pressure of the inert gas should be low enough to accelerate the ions, but high enough to initiate plasma formation [76].

A configuration of small ring magnets is positioned below the sputtering target in the magnetron system. These magnets create magnetic lines that exert a perpendicular force on the electrons, causing them to follow a circular path over the sputtering target. As a result, sputter erosion is significantly higher in an annular ring region, while erosion is reduced in other areas. Figure 3.13 illustrates the impact of sputtering on a target.

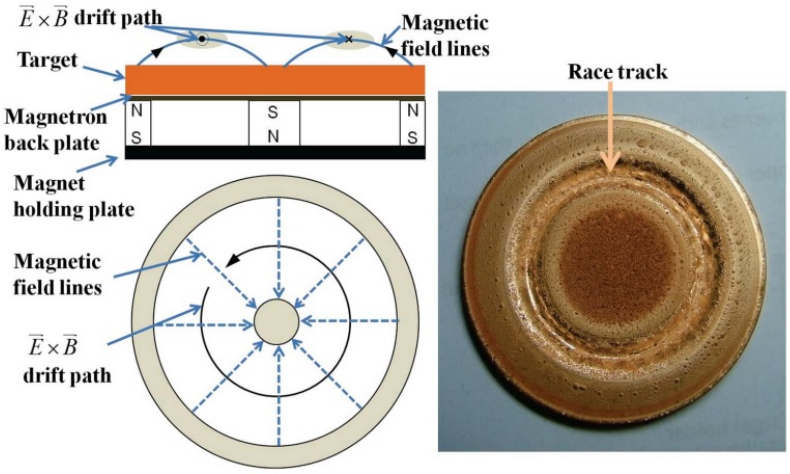

Figure 3.13: Target erosion (from [77])

The sputtering yield, which represents the amount of material sputtered from the target per incident ion, is directly proportional to the number of free metal atoms sputtered from the target in a given time period. Goeckner et al. [78] showed that for a fresh, flat target, the Ar^+ ions hit the cathode surface at nearly perpendicular angles. If we assume that the angle of incidence of the impinging Ar^+ ions increases as the target erodes, then the sputtering yield will vary accordingly based on the changing angle of incidence throughout the life of the target. Ganeva et al. [77] found that cluster formation stops well before the target material is completely sputtered. The main factor influencing this phenomenon is the change in sputtering yield based on the angle at which the ions hit the target surface. This in turn affects the density of free metal atoms. Once a certain angle of incidence is reached, the sputtering rate decreases rapidly.

3.7.2 The quadrupole mass filter-size selection

A quadrupole mass filter is commonly used as part of the mass spectrometry system to separate and analyze nanoclusters based on their mass-to-charge ratio. The operation

of a quadrupole mass filter involves applying radio frequency (RF) and direct current (DC) voltages to a set of four rods arranged in a square or rectangular configuration. The quadrupole mass filter is positioned after the cluster source to select a specific mass from the charged clusters produced in the aggregation zone. The diagonally opposed rods within each set are electrically connected. The pairs of rods are subjected to a voltage of

$$V_{quad} = U + V \cdot \cos(\omega \cdot t)$$

which includes both DC and AC components, with a frequency ranging from 1 to 100 kHz. Each rod has a radius (r_{rod}) that is 1.144 times larger than the field radius (r_0), which is half the distance between opposite rods. The pairs are biased so that one pair is in phase opposition to the other. The cluster ions first enter the quadrupole mass filter through an electrically grounded aperture plate (see Figure 3.14). They then pass through the central axis of the quadrupole and undergo an oscillatory motion caused by the AC and DC components of the applied voltage as described by the Mathieu equation. The Mathieu equation, which describes the trajectories of the ions, is solved using two parameters:

$$a = \frac{8Q \cdot U}{mr_0^2 \cdot \omega^2}$$

$$q = \frac{4Q \cdot V}{mr_0^2 \cdot \omega^2}$$

where Q is the charge of an ion with mass m. If the amplitude of a trajectory is less than r_0, it is considered stable. However, if an ion has a larger amplitude, it comes into contact with a quadrupole rod and is neutralized. A collector plate positioned between two electrically grounded plates measures the cluster current, which serves as an indicator of the number of clusters of the selected size passing through per second. The mass of

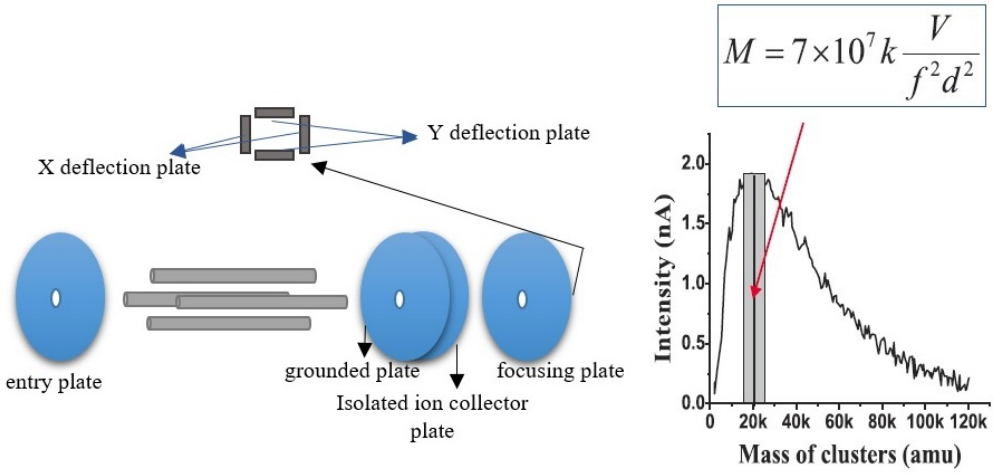

Figure 3.14: Quadrupole mass filter and an example of the cluster mass.

the cluster selected by the quadrupole mass filter (QMF) is determined by

$$M = 7 \times 10^7 k \frac{V}{f^2 \cdot d^2}$$

where V is the amplitude and f is the frequency of the AC voltage, d is the diameter of the poles, and k is a correction factor that is approximately equal to one. To obtain a specific cluster mass or size, the AC voltage, frequency, and DC component of the applied voltage must be adjusted.

3.7.3 Size distribution

Controlling the size of nanoclusters is a critical factor in determining the properties of the film formed on a substrate. Within a nanocluster source, several components influence the size distribution of the clusters during production. By adjusting various parameters such as Ar and He gas flow, aggregation zone length, cooling time, magnetron power and others, a narrow and concentrated size distribution of the clusters can be achieved. The result is a lognormal size distribution, which can be represented by a Gaussian distribution plotted against an exponential abscissa. This type of distribution has been discussed by Granqvist et al. [79].

Kiss et al. presented an explanation of the mechanism occurring within the gas aggregation region, which was further validated by numerical simulations [80]. Their model is based on two assumptions: (1) particle growth is directly proportional to its surface area, and (2) the residence time within the growth zone follows a log-normal distribution. These assumptions hold when both diffusion and drift effects are considered. The log-normal height distribution $f(d)$ can be expressed mathematically as:

$$f(d) = f_0 + \frac{A}{\sqrt{2} \cdot \ln \sigma} \exp(-\frac{(\ln d - \ln d_0)^2}{2 \cdot (\ln \sigma)^2})$$

The symbol d_0 stands for the mean diameter, σ for the standard deviation, and A for a scaling factor. The parameter f_0 represents the vertical offset of the distribution, e.g. the mean value below a certain reference point. It is important to note that in the size distribution of nanoparticles, there is no such reference point below which the distribution has a non-zero offset.

A more in-depth discussion of the various parameters affecting the growth/deposition process will follow, using test data from Oxford Applied Research for clarification. The NC200U was utilized in all these tests, with argon (Ar) as the sputtering gas and copper (Cu) as the target material. Figure 3.15 shows the mass spectra of Cu nanoclusters for different values of Ar flow rate (in sccm). As the gas flow increases, the average cluster size increases, reaches a maximum, and then decreases. Initially, the cluster size (or number of atoms in a cluster) increases as a result of the enhanced formation of Ar ions, which promotes the growth of larger clusters due to the availability of more sputtered particles. However, as the gas flow rate continues to increase, the excess Ar gas no longer contributes significantly to the sputtering process and quickly passes through the aggregation zone without participating in cluster growth. Consequently, this phenomenon results in the cluster having a shorter residence time within the aggregation zone or leaving the zone relatively faster. As a result, the growth of larger clusters is restricted, preventing them from increasing in size.

The He gas flow in the aggregation region can affect the cluster size. The relationship between cluster mass and the He gas flow rate is shown in Figure 3.16.

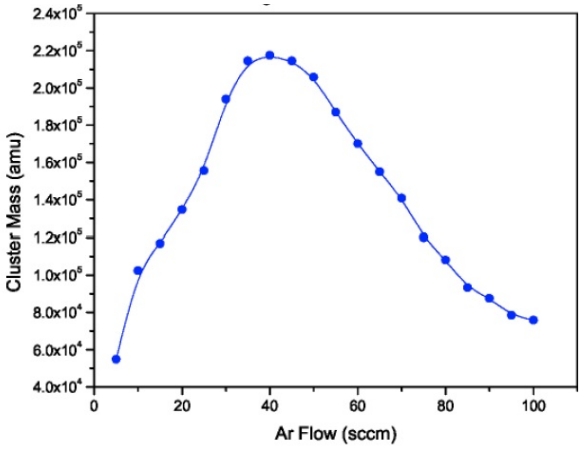

Figure 3.15: Mean cluster mass of Cu clusters as a function of Ar gas flow (from [81])

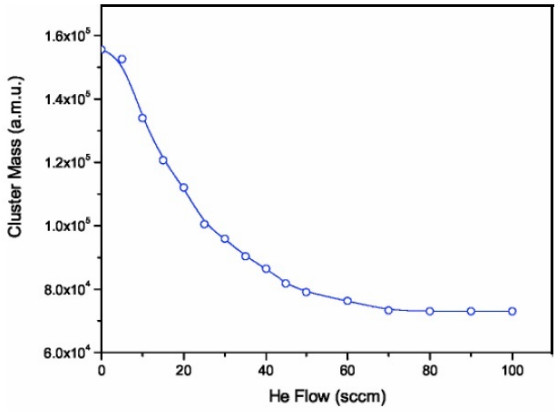

Figure 3.16: Mean cluster mass of Cu clusters as a function of He gas flow (from [81])

The flow of helium (He) plays an important role in initiating the process of cluster condensation in the gas phase. Pratontep et al. [80] referred to the initial small clusters as "seeds", which subsequently grow into larger clusters. The growth of smaller clusters is a result of three-body collision processes that occur due to an increase in the drift velocity of the clusters and a decrease in the mean free path of collisions in the aggregation region.

The cluster size distributions are also affected by another parameter known as the aggregation length. The effect of the aggregation length on the cluster mass is shown in Figure 3.17. This is the distance between the magnetron sputtering target and the exit nozzle connected to the quadrupole mass filter. Cluster growth within the aggregation region is determined by collisions between sputtered atoms and pre-existing atoms or clusters. When the aggregation length is shorter, there are fewer collisions between the atoms or clusters, resulting in the production of smaller clusters. Conversely, longer aggregation lengths result in longer dwell times for the clusters, allowing the formation of larger clusters. Another parameter that significantly affects the cluster is the power of magnetron. As the power is increased, a greater number of metal ions are sputtered, resulting in increased aggregation of atoms into clusters. As a result, the cluster size tends to increase. However, there is a point at which the cluster size begins to decrease.

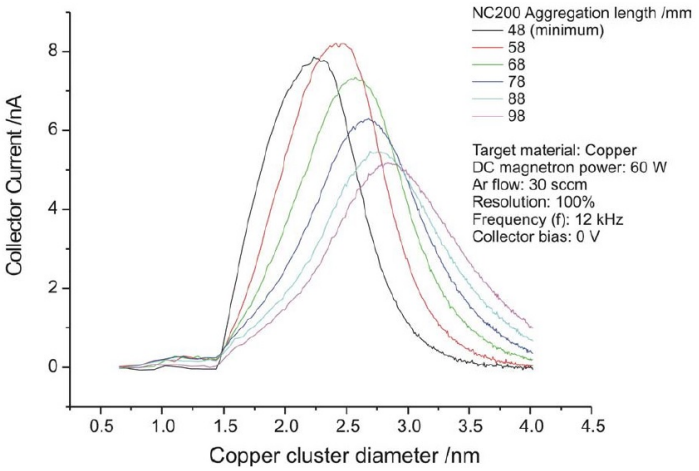

Figure 3.17: Effect of aggregation length on cluster size distribution (from [81])

However, it is important to note that the exact relationship between magnetron power and nanocluster size distribution can be complex and depends on various factors such as gas pressure, deposition conditions, and the nature of the target material.

3.7.4 Nanocluster formation

The sputtering process results in the release of atoms, and possibly small clusters, as a highly concentrated vapor. This vapor is in a metastable state and collisions involving three atoms occur. Two atoms come from the sputtering, while the third atom comes from the buffer gas. When the gas atom interacts with the sputtered atoms, it absorbs the excess energy, satisfying the conservation of energy and momentum and allowing the atoms to form a dimer, called a nucleus. The dimer can grow further by additional collisions. Depending on the experimental conditions, smaller nuclei can also decay. The critical size is the size at which the nucleus becomes stable. This phenomenon is commonly referred to as nucleation. When nucleation occurs, primary clusters or nuclei are formed. The growth of larger clusters from nuclei can occur through various mechanisms and processes. The primary clusters typically have a particular structure or arrangement of atoms. In some cases, when two primary clusters come close enough together, they can interact and merge to form a larger cluster. This merging process is called aggregation. During aggregation, it is possible for the individual primary clusters to partially retain their original structures. This means that the resulting larger cluster may have a fractal-like structure [82]. Another possible process is coagulation.

Coagulation refers to the process by which two separate liquid droplets, called nuclei, come into contact and coalesce to form a single, larger droplet. During the coalescence process, two initially separate clusters come into direct contact and merge to form a single, larger cluster. The shape of the newly formed cluster is influenced by the mobility of the atoms along the edges. If the mobility of the edges is low, the clusters will stick together without being reshaped. In many cases, however, the mobility is sufficient to allow the forming cluster to regain its equilibrium shape. Atom attachment refers to the phenomenon of individual free atoms colliding with existing nuclei and becoming part of the growing cluster [36].

In this work, a magnetron sputtering source provided by Oxford Applied Research, the NC200U, was used. This commercially available source has been specifically designed for ultra-high vacuum (UHV) environments and optimized to achieve high sputtering rates. The quadrupole mass filter is a QMF200 from Oxford Applied Research designed to analyze and filter the charged particles from the NC200U. The QUVI2 software provided by Oxford Applied Research allows computer controlled manipulation of the source parameters. This control includes all parameters related to nanoparticle generation except the aggregation length. The software also allows control of the QMF. The frequency (f) can be adjusted in the range of 3 to 100 kHz and the AC voltage (V) in the range of 1 to 250 V. After adjustment, the software calculates the corresponding mass, allowing us to select the favorable mass for deposition of nanoparticles. In addition, the software calculates the atomicity of the nanoparticles based on their atomic weight and determines the expected diameter based on the density of the sputtering target material. The filter width ($\Delta m/m$) can be adjusted between 2% and 100% and the U-V ratio is automatically adjusted accordingly.

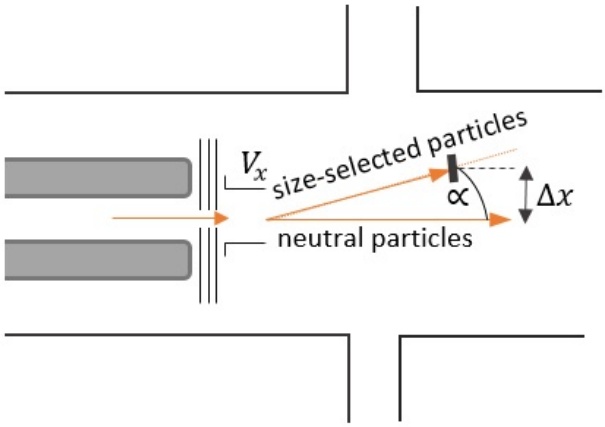

Figure 3.18: Deflection of nanoparticles

The required deflection voltage for the XY control plates was determined experimentally [83]. The voltage was systematically varied in the range of 0 to 100 V while keeping the particle mass constant. The goal was to determine the voltage at which the current on the sample reached its maximum value. The value of the voltage to deflect a nanoparticle of n_{Fe} Fe atoms is:

$$V_x = 0.6427\text{V} \cdot \frac{n_{Fe}}{1000} \cdot \frac{\Delta X}{1\text{ mm}} \cdot \frac{80\text{ mm}}{\Delta Z}$$

The sample is positioned ΔX away from the central beam and at a distance ΔZ from the deflection plates (Figure 3.18).

3.8 Evaporator

The EFM typically uses a rod-shaped material source made of the desired material to be evaporated. The rod is placed in the evaporation chamber. Electron bombardment heating is the primary method used to heat and vaporize the material in the evaporator. High energy electrons are generated and directed at the material rod. Upon impact with

the rod, the electrons transfer their energy, resulting in increased atomic vibration and eventual vaporization of the material. The EFM has an internal flux monitor that continuously monitors the evaporation rate.
The EFM 3T, a triple evaporator manufactured by Omicron, is used in this work. The setup of the heating filament and rod can be observed in Figure 3.19. A notable feature of this system is its crucible-free evaporation method, which ensures a high level of cleanliness. In addition, the evaporator is equipped with an internal flux monitor that allows accurate rate adjustment after calibration, ensuring precise control of the evaporation process.

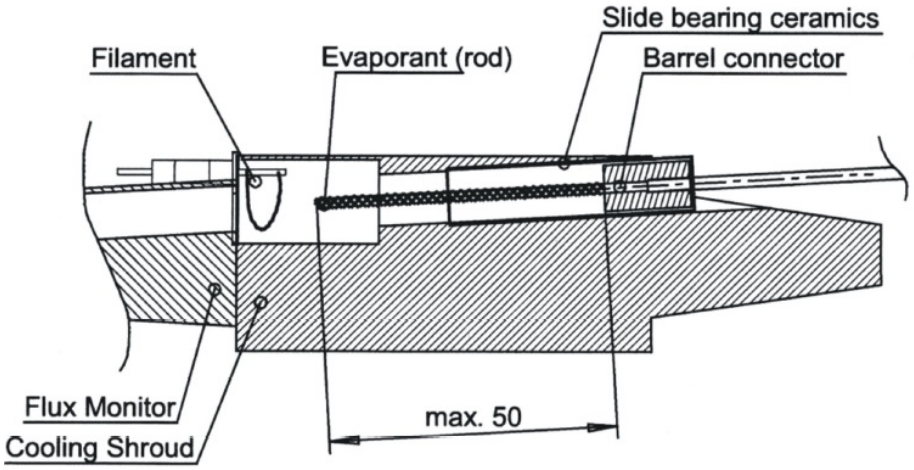

Figure 3.19: Diagram illustrating a single cell within the Omicron triple evaporator EMF 3T (from [84])

Rate calibration

In order to obtain an accurate measurement of the number of monolayers, it is necessary to calibrate the evaporation rate of the equipment. In this work, LEED is used to determine the deposition rate.

The change in crystal structure at a given area coverage or number of monolayers can be detected using LEED. This change in crystal structure needs to be understood and validated by comparison with other techniques. The accuracy of this calibration depends on the materials used, as certain materials initially exhibit pseudomorphic growth and the restructuring of the crystal structure may be a transient process. For Co deposited on W(110), the initial monolayer forms a commensurate structure with the substrate. However, at about 1 monolayer (ML), there is an abrupt transition to the densely packed basal plane of Co(0001). The W(110) crystal has lattice parameters of 3.16Å and 4.467Å along the [001] and [110] directions of W, respectively. The transition from the commensurable structure to the densely packed basal plane of Co(0001) leads to a significant distortion of the lattice parameters of the Co layer compared to its bulk values. This distortion is caused by pseudomorphic growth, where the Co layer adapts to the lattice structure of the substrate, resulting in deviations from its typical lattice parameters. As the Co coverage increases, additional speckles appear in the LEED pattern. The pattern described

is denoted as (4×1) relative to the W lattice parameters [001] and [110] [85]. It indicates that the Co overlayer is closely aligned with the W substrate in a Nishiyama-Wassermann orientation. As the coverage increases, the additional spots gradually disappear and the LEED pattern transitions to a simple 1×1 hexagonal pattern, which is expected for the Co basal plane. These additional spots can be observed up to a coverage of 4 monolayers (ML) of Co.

The evaporation rate can also be determined by using STM to measure surface coverage at sub-monolayer levels after deposition. The accuracy of this method is limited by several factors. Small-scale deposition uniformity is not always guaranteed and is influenced by substrate properties such as step size, temperature distribution, and the presence of surface defects such as adatoms or dislocations. Quantitative determination of surface coverage becomes challenging when the thin film accumulates primarily from step edges. To minimize these limitations, surface coverage is typically determined by averaging measurements from multiple locations on the surface.

3.9 Surface preparation

The experiments carried out in this work were based on a tungsten crystal with a (110) orientation. It was used as a substrate for the deposition of nanoparticles, thin films of cobalt and graphene. A two-step flashing process was used for cleaning. First, cycles of low power flashes are performed at a temperature of about 950 °C under an oxygen partial pressure of $p_{O_2} = 6 \times 10^{-8}$mbar where the heating power is alternately turned on for 15 s and turned off for 60 s. This is done to remove any remaining carbon from the surface. In the second step, a single high power flash is applied at a temperature of about 2200 °C. Figure 3.20 shows the LEED pattern of the tungsten crystal after low power flashes in an oxygen atmosphere s well as a high power flash at 2200 °C.

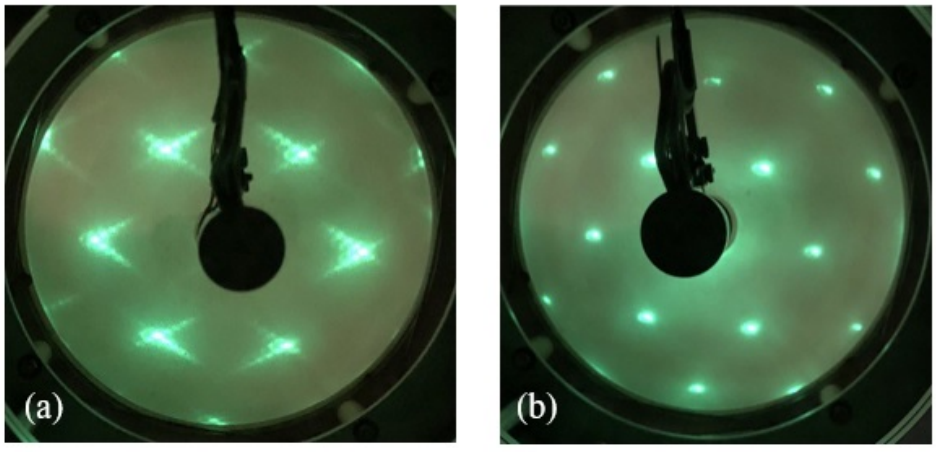

Figure 3.20: LEED images of a) W(110) after low power flashes in an oxygen atmosphere (122 eV), b) W(110) after a single high power flash at 2200 °C (189 eV)

The single high power flash was performed prior to each deposition of nanoparticles and thin films. There was no change in the LEED pattern after flashing, so additional oxygen annealing was rarely necessary.

3.10 Sample heating

It is important to understand the characteristics and capabilities of the heating systems being used. Different heating systems can have unique features, limitations, and performance characteristics. The temperature of a sample has a significant effect on its dynamic behavior. Variations in temperature can affect the properties and characteristics of the sample. Understanding these aspects allows for better control and manipulation of the sample temperature during experimentation or analysis.

This section provides an overview of the different types of thermometers that can be used to accurately measure temperature. It also introduces different types of heaters used to control and adjust the temperature of the sample. A thermocouple is a type of temperature sensor based on the Seebeck effect, which involves the generation of a voltage in a conductor when there is a temperature gradient along its length. To accurately measure temperature with a thermocouple, it must make physical contact at the point of measurement. The manipulators are equipped with two Type K thermocouples. These thermocouples are positioned adjacent to the sample, where the distance between the substrate and the thermocouple results in a discrepancy between the actual temperature and the temperature reading obtained from the thermocouple. This is due to the thermal gradient and heat dissipation effects that occur across the gap between the thermocouple and the sample.

Radiation thermometers, often referred to as pyrometers, offer a contactless approach to measuring temperature. They work by measuring the infrared radiation emitted by an object. When an object is heated to a non-zero temperature, it emits infrared light, and the spectral density of this emission follows Planck's law. In theory, a black body is an idealized object that absorbs all incident radiation and emits radiation with maximum efficiency at all wavelengths. However, real objects have optical properties that differ from those of a black body. These objects are called gray bodies because they absorb and emit less radiation than a black body. The difference in emission between a gray body and a black body is expressed as the emissivity $\epsilon(\lambda, T)$, which depends on the material and temperature of the object.

To accurately determine the true temperature of an object using a radiation thermometer, it is necessary to know the emissivity of the object. The emissivity factor accounts for the deviation from idealized blackbody behavior and allows the temperature of the object to be calculated based on its spectral emission. By accounting for emissivity and applying appropriate corrections, radiation thermometers can provide valuable temperature measurements without the need for physical contact with the measured object.

Two pyrometers were used for the temperature measurements. One is the Ircon Ultimax Plus UX 20P, a narrow band radiation thermometer. It works by measuring the emission at a single, fixed wavelength. Specifically, the wavelength of measurement is 0.96 μm . This pyrometer is capable of measuring temperatures in the range of 600 to 3000 °C. These pyrometers were used in electron bombardment heating (flashing) and oxygen annealing processes performed on tungsten substrates.

Several experiments have been performed to determine the exact emissivity of various metals. This factor is influenced not only by the composition of the material, but also by variables such as temperature, emission angle, and surface roughness [86]. Until further advances are made in this area, the emissivity for measurements on polished tungsten

crystals is set at 0.3. The other pyrometer used in this work for sample annealing is the Raytek MI3 2M, which operates at $\lambda = 1.6\mu$m . In the analysis or preparation chamber (see section 3.1), samples were typically annealed on the manipulator's built-in heater. A laboratory power supply was used to adjust the current with a precision of 0.01 A. To achieve the desired temperature, the current was selected based on a calibration sheet (see Table A.1), taking into account previous measurements. If necessary, the current was modified during the annealing process.

4 Result and discussion

The aim of this work is to prepare size-selected nanoparticles on tungsten and graphene surfaces and to analyze their melting behavior after temperature treatment. This chapter presents the results of the experiments performed. It includes the deposition of iron-nickel nanoparticles with different compositions and the subsequent annealing of these nanoparticles. The exemplary HR-TEM images, EDX maps, and STM images taken after each of the deposition and heating cycles will be analyzed. The final section provides a summary and a brief discussion of all the results obtained.

4.1 FeNi nanoparticles on W(110)

In this section, we will discuss the preparation of iron-nickel nanoparticles using magnetron sputtering as a source, their deposition on tungsten, and the subsequent annealing process.

Sample preparation

W(110) was cleaned by flashing prior to nanoparticle deposition. The specific procedure is described in section 3.9.

Iron-nickel nanoparticles were produced using the magnetron sputtering source. Three types of FeNi alloys were used: $Fe_{0.75}Ni_{0.25}$, $Fe_{0.5}Ni_{0.5}$, $Fe_{0.25}Ni_{0.75}$, as well as pure nickel and iron. Mass selection was performed on the quadrupole mass filter and is controlled by frequency and amplitude of an AC voltage. The deposition parameters and the average size of the nanoparticles for each sample are given in Figure 4.1.

After deposition, the first STM images were taken. The STM images and height distribution of FeNi with three different compositions and Ni and Fe nanoparticles after deposition are shown below. The majority of the nanoparticles have a size in the range of 3 - 5 nm. All particles were spherical in shape. In all cases, the nanoparticles were found to have no preferred adsorption sites. Instead, they accumulate randomly on both flat surfaces, called terraces, and on step edges.

4.2 Melting behavior of FeNi nanoparticles on W(110)

This section of the chapter deals with the melting behavior of the nanoparticles by describing and analyzing the STM images taken after each heating cycle.

4.2.1 Annealing at 540 K

In the first heating cycle, the nanoparticles were heated to 540 K for 30 minutes. Figure 4.2 shows a section of the particles after heating. The first change is the height of

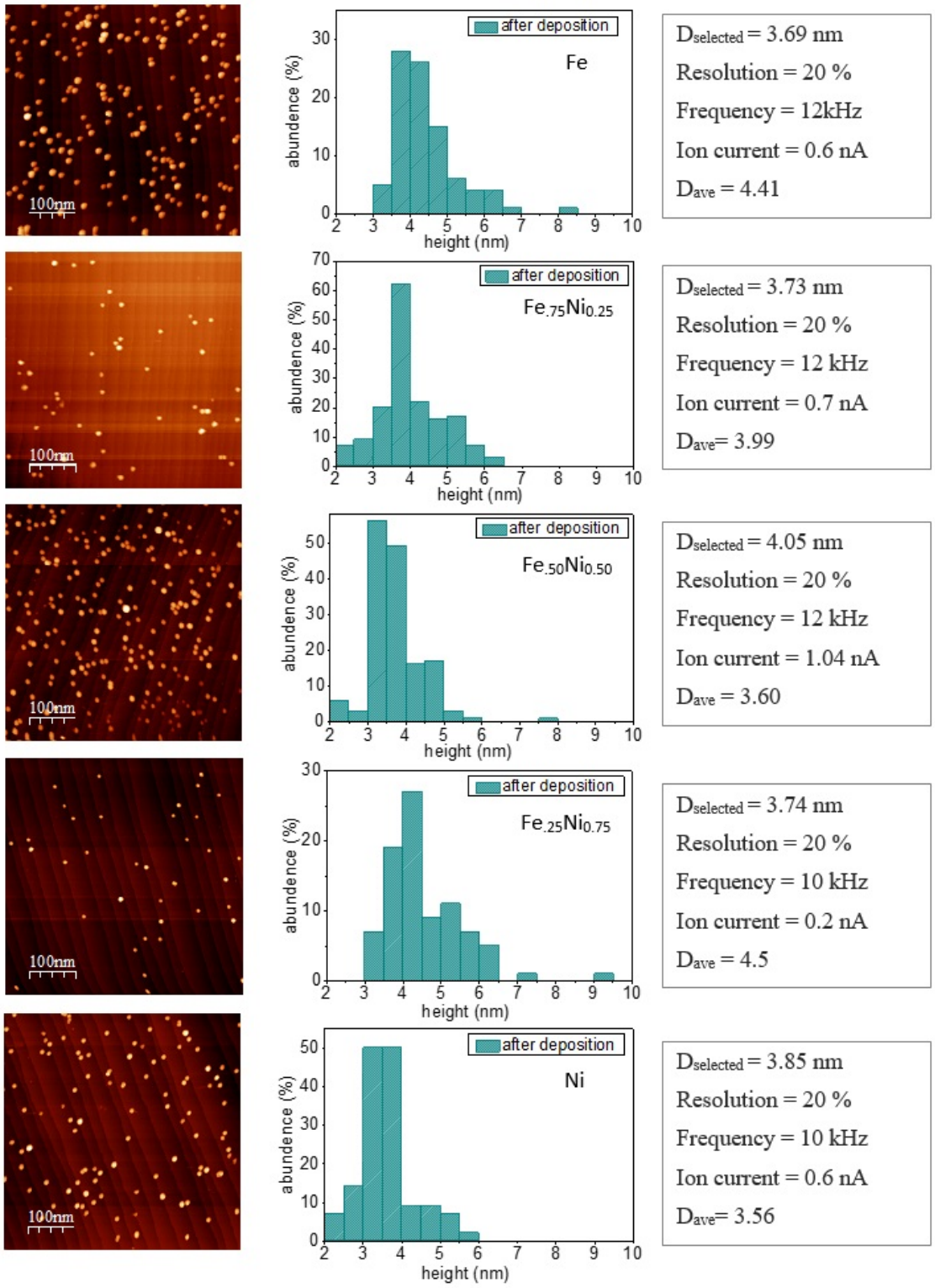

Figure 4.1: STM images and the height distribution of the nanoparticles after the deposition process.

the nanoparticles: compact islands have been formed, all with a height of about 2.5 Å. Comparing this value with the diameter of an iron atom, $d_{Fe} = 248.2$ pm, and a nickel

atom, $d_{Ni} = 249.2$ pm, it becomes clear that the compact islands consist of only one monolayer. Thus, the nanoparticles are already completely melted, which is why only the term "island" is used in the following.

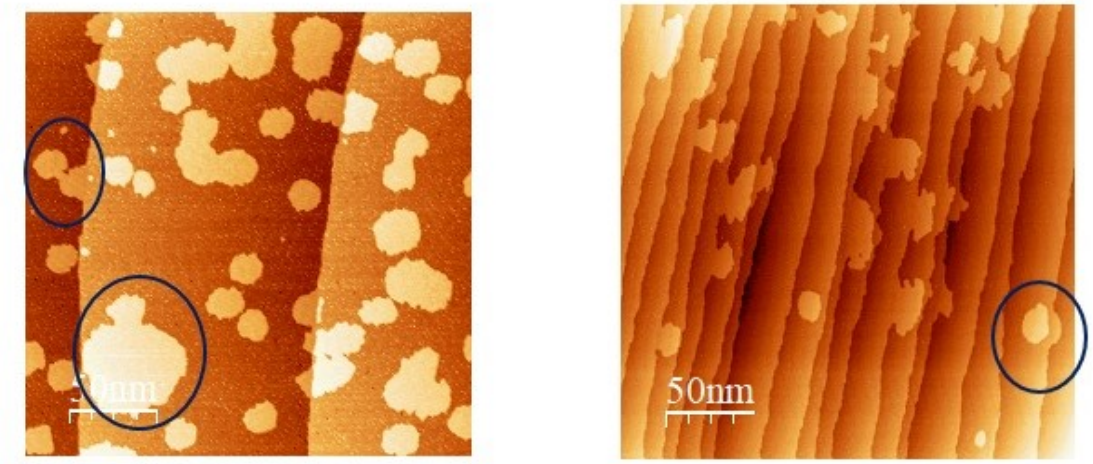

(a) Fe nanopartcles after heating at 540 K

(b) $Fe_{0.75}Ni_{0.25}$ nanoparticles after heating at 540 K

Figure 4.2: STM image of Fe and $Fe_{0.75}Ni_{0.25}$ nanoparticles on W(110) after annealing. Preselected particle diameter of iron particles was d=3.69 nm and $Fe_{0.75}Ni_{0.25}$ particles was d=3.73 nm .

Fe

The diffusing atoms have agglomerated at the step edges of the substrate. This indicates the high mobility of Fe atoms at 540 K. In Fig. 4.2, the merging of two islands can be observed, which probably proceeds according to the principle of dynamic coalescence. It can occur as a result of the collision of two islands, where mobile island diffuse across a surface to form a larger island when they collide [36].

$Fe_{0.75}Ni_{0.25}$

Just like the Fe islands, the $Fe_{0.75}Ni_{0.25}$ islands exhibit a similar behavior by agglomerating at the step edges of the substrate within narrow terraces. These islands maintain their compact shape after undergoing a melting process. This observation highlights the similarity in island growth behavior between Fe islands and $Fe_{0.75}Ni_{0.25}$ islands.

$Fe_{0.5}Ni_{0.5}$

Islands with a monoatomic height around some $Fe_{0.50}Ni_{0.50}$ nanoparticles can be observed due to the unrolling carpet behavior (Figure 4.3). For both Fe and Ni, this implies that a film of a single monolayer thickness, defined by a distinct boundary, extends across the surface. The assumption is made that the atoms within the initial layer remain stationary.

Beyond this initial layer, atoms undergo diffusion, once they reach the edge of the diffusion area and make contact with the substrate, where they become stuck.

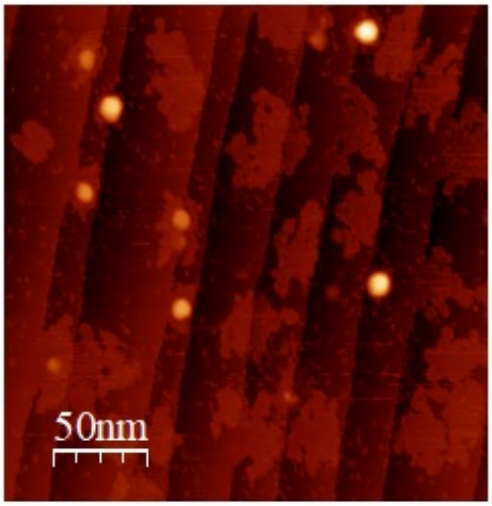

Figure 4.3: STM image of $Fe_{0.5}Ni_{0.5}$ nanoparticles on W(110) after annealing. Pre-selected particle diameter was d=4.05 nm .

$Fe_{0.25}Ni_{0.75}$

The $Fe_{0.25}Ni_{0.75}$ particles are completely melted and they have a ramified shape (Figure 4.4). The complex structure of the ramified shape poses a challenge in determining the precise location of the original nanoparticle. It's important to note that the temperature and duration of the tempering process is responsible for the formation of ramified islands after tempering.

Ni

Compared to iron atoms at the same temperature, nickel atoms exhibit lower mobility or have a stronger binding energy with the surface. In other words, nickel atoms are less likely to move or diffuse across the surface and are more strongly attracted to the surface compared to iron atoms. The change from a fractal to a compact shape takes place by increasing the temperature. As the temperature rises, the atoms begin to diffuse along the island's edges and cross the corner if it is favorable for the atoms. This results in the formation of compact islands.

4.2.2 Annealing at 580 K

Fe

The next higher temperature step was carried out for 30 minutes at a temperature of approximately 580 K. All samples showed islands of one monolayer in height. There

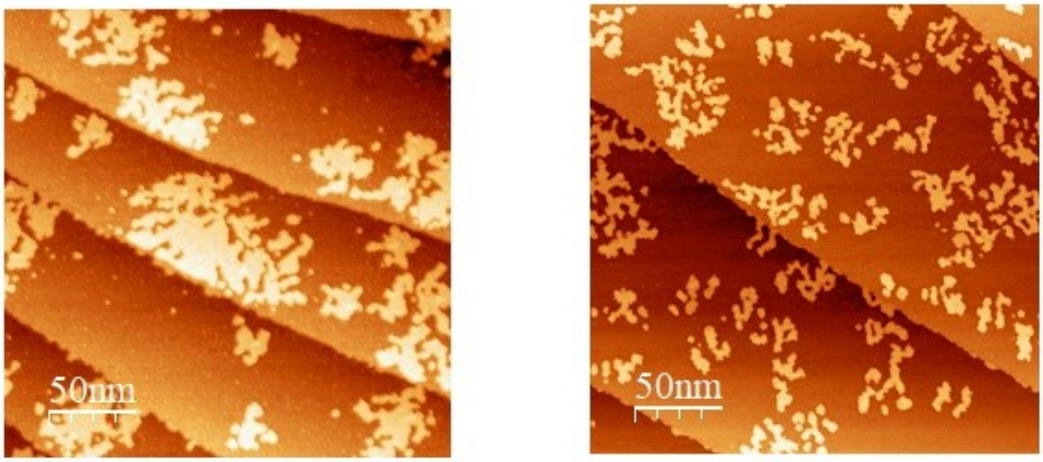

(a) $Fe_{0.25}Ni_{0.75}$ nanopartcles after heating at 540 K (b) Ni nanoparticles after heating at 540 K

Figure 4.4: STM image of $Fe_{0.25}Ni_{0.75}$ and Ni nanoparticles on W(110) after annealing. Pre-selected particle diameter of $Fe_{0.25}Ni_{0.75}$ particles was d=3.74 nm and Ni particles was d=3.85 nm.

is no change in the shape of the iron islands as shown in Figure 4.5(a). They are all agglomerated at the step edges in narrow terraces.

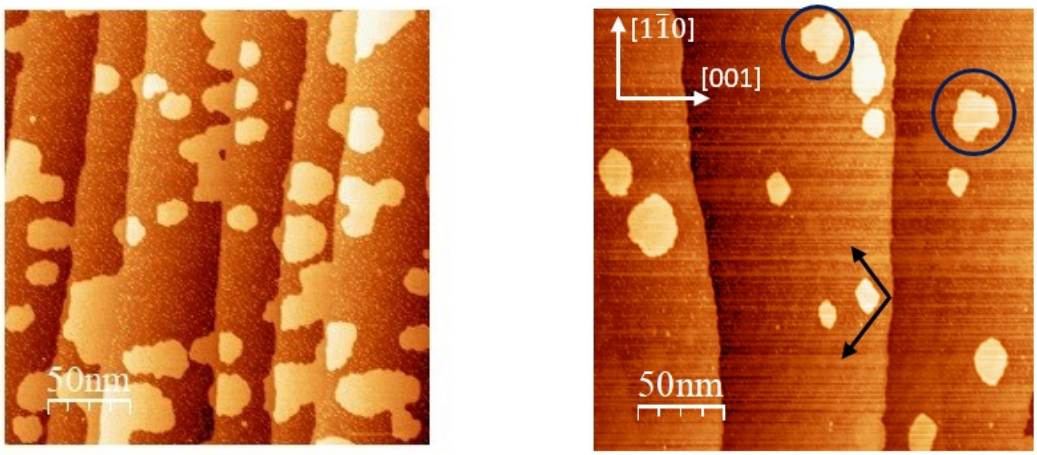

(a) Fe nanopartcles after heating at 580 K (b) $Fe_{0.75}Ni_{0.25}$ nanoparticles after heating at 580 K

Figure 4.5: STM image of Fe and $Fe_{0.75}Ni_{0.25}$ particles on W(110) after subsequently annealing

$Fe_{0.75}Ni_{0.25}$

Some islands of $Fe_{0.75}Ni_{0.25}$ are showing anisotropic spreading along the W[111] axes (Figure 4.5), caused by the crystallographic structure of the substrate. A noticeable feature

is an island with a bulge on the side, shown in Figure 4.5(b), which probably represents the merging of a larger island with a smaller one (coalescence). If this were to occur as a result of the collision of the two islands, this process would probably follow the principle of Smoluchowski ripening (dynamic coalescence).

The so-called Ostwald ripening might not be the underlying process in this particular case, since it involves a flow of material from a smaller to a larger island occurs, which is triggered by the system's drive for energy minimization [36]. In contrast, the bulge seen in Figure 4.5 (b) can presumably only occur when two islands collide, and consequently during Smoluchowski rifting. To check for the presence of Ostwald ripening, we investigatee whether the frequency of small islands decreases in subsequent experiment stages. Smoluchowski ripening likely contributes to the development of larger islands. However, clear indications supporting this, based on all the provided images, are exceptionally rare. Thus, Smoluchowski ripening alone cannot be solely responsible for the growth of the islands. Instead, it appears that Ostwald ripening is the primary driving force behind most of the island growth. This conclusion is drawn from the consistent presence of smaller-than-average islands in nearly all images, with their sizes remaining unchanged from the start to the end of the experimental stages. Since islands generally increase in size over the heating cycles, the consistent presence of small islands can only be attributed to Ostwald ripening and the subsequent evaporation of material.

$Fe_{0.5}Ni_{0.5}$, $Fe_{0.25}Ni_{0.75}$ and Ni

The islands present in the remaining samples exhibit a distinctive branched configuration, as shown in Figures 4.6 and 4.7. These graphical representations illustrate an important observation, the thermal conditions at 580K were apparently insufficient to facilitate the transformation of the islands into a more tightly integrated structure. An interesting observation arises from the analysis of the images. There is a discernible pattern where wider terraces tend to host a greater number of islands compared to narrower terraces.

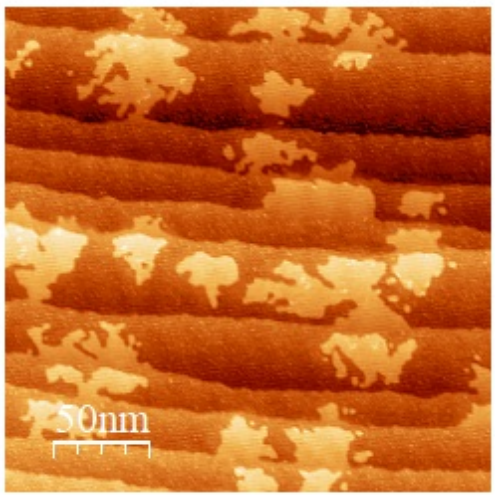

Figure 4.6: STM image of $Fe_{0.5}Ni_{0.5}$ nanoparticles on W(110) after subsequently annealing at 580 K.

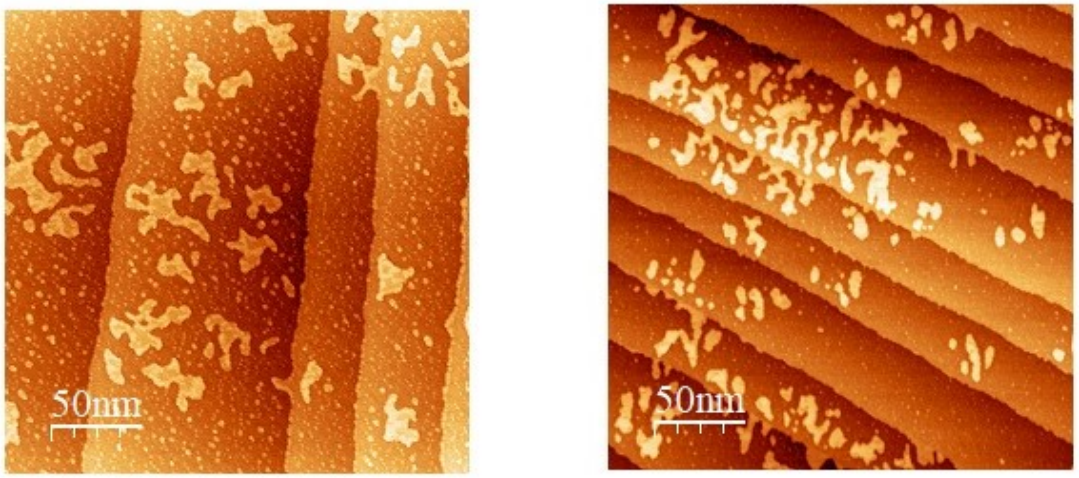

(a) $Fe_{0.25}Ni_{0.75}$ nanopartcles after heating at 580 K (b) Ni nanoparticles after heating at 580 K

Figure 4.7: STM image of $Fe_{0.25}Ni_{0.75}$ and Ni nanoparticles on W(110) after subsequently annealing.

4.2.3 Annealing at 840 K

Fe

All islands have compact shape by tempering at 840 K for 30 min. Figure 4.8 (a) shows that the Fe islands are even larger than before. A comparison of the STM images of Fe and Ni islands shows that the iron is able to form larger islands than nickel. This can be interpreted as a consequence of the higher mobility of iron in comparison with nickel.

$Fe_{0.75}Ni_{0.25}$

Figure 4.8 shows that some $Fe_{0.75}Ni_{0.25}$ islands have a hexagonal shape, with the edges and angles being of different lengths and sizes. A possible explanation could be that in large islands the stress on atoms located at the edges of the island is not as great as in smaller islands. Therefore, the effort to leave this shape is not as strong as in smaller islands. In addition, the restructuring of larger islands involves a correspondingly larger number of atoms, so the process necessarily takes longer. It is also noticeable that wider terraces tend to host a greater number of larger islands compared to their narrower counterparts. Additionally, a notable observation is that the material is found exclusively on the terraces and is no longer present on the step edges. Finally, stretching in the $[1\bar{1}0]$ direction can be caused by anisotropic diffusion of atoms on the tungsten surface. The surface of the W(110) crystal itself is anisotropic. As can be seen in Figure 2.7, the distance between two surface atoms in the [001] direction is exactly one lattice constant a, while in the $[1\bar{1}0]$ direction it is $\sqrt{2}$ times the lattice constant. An impurity atom now has several ways to diffuse across the surface. However, direct jumps over a tungsten atom are very unlikely because of the high energy required, so an impurity atom will mainly travel by [111] jumps. Now, diffusion in the [001] and $[1\bar{1}0]$ directions is a combination of two

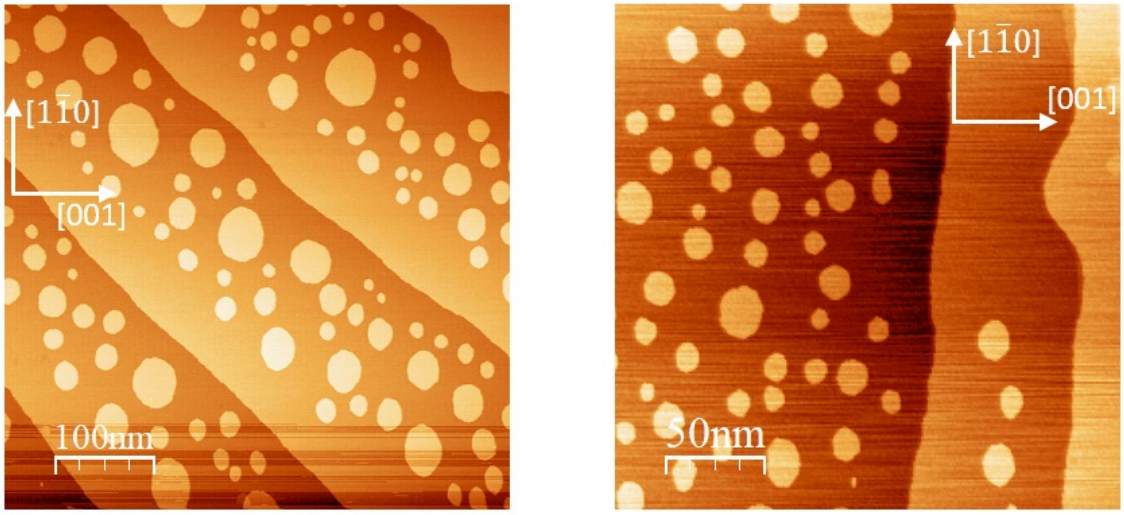

(a) Fe nanopartcles after heating at 840 K

(b) $Fe_{0.75}Ni_{0.25}$ nanoparticles after heating at 840 K

Figure 4.8: STM image of Fe and $Fe_{0.75}Ni_{0.25}$ nanoparticles on W(110) after subsequently annealing

jumps in the [111] direction, so it is equally likely for both directions. However, since the W(110) surface is inherently anisotropic, this inevitably affects the structure of the islands, making them elliptical in the [1$\bar{1}$0] direction by a factor of $\sqrt{2}$ compared to the [001] direction.

Since the stretching of the islands in the [1$\bar{1}$0] direction also occurs when the step edges are not aligned with this direction, it can be concluded that the observed stretching is solely influenced by the geometry of the W(110) surface. Furthermore, considering that the heating was carried out at temperatures around 840 K, this is in agreement with the findings of Reuter et al. on the diffusion of nickel [39]. Additionally, it should be noted that the iron-nickel alloy adapts the behavior exhibited by iron and nickel alone at this temperature.

$\mathbf{Fe_{0.50}Ni_{0.50}}$

Regarding the $Fe_{0.50}Ni_{0.50}$ islands, it should be noted that the islands have formed only in a very narrow, defined area on the terraces, which is slightly shifted towards the sloped side (Figure 4.9). This and the fact that no islands can be observed at all on the narrow terraces leads to the assumption that material melts at the step edges of the tungsten substrate if it is close enough to them and is therefore no longer visible in the STM images. On the other hand on narrow terraces, the distance to the step edges is necessarily smaller/too small, hence no material is located there. In addition, the melting of an island on a step edge can be directly observed, which confirms the assumption made before.

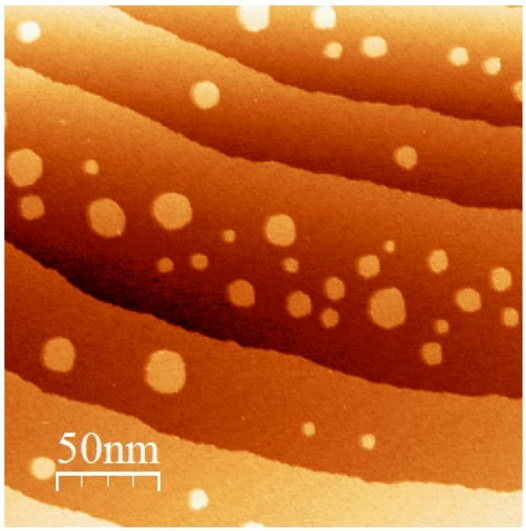

Figure 4.9: STM image of $Fe_{0.50}Ni_{0.50}$ nanoparticles on W(110) after subsequently annealing at 840 K.

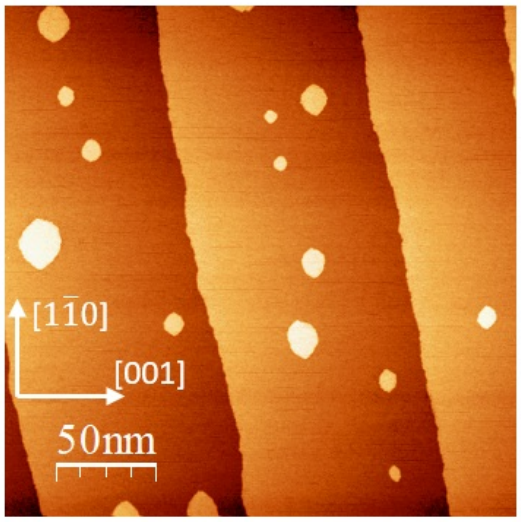

(a) $Fe_{0.25}Ni_{0.75}$ nanoparticles after heating at 840 K

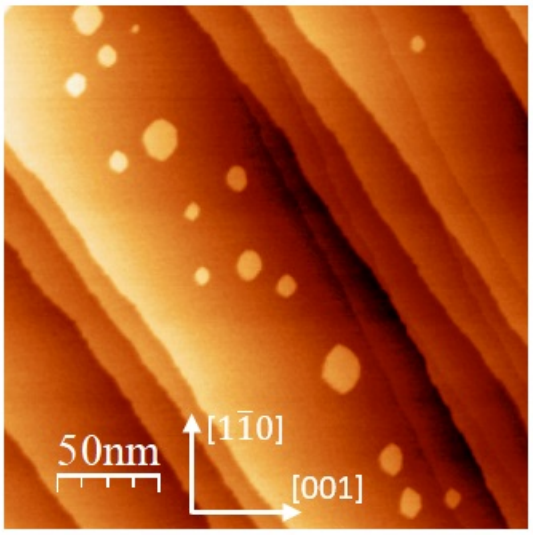

(b) Ni nanoparticles after heating at 840 K

Figure 4.10: STM image of $Fe_{0.25}Ni_{0.75}$ and Ni nanoparticles on W(110) after subsequently annealing.

$\mathbf{Fe_{0.25}Ni_{0.75}}$

In the context of $Fe_{0.75}Ni_{0.25}$ islands, it's worth noting that a hexagonal structure is emerging, as indicated by the distinct edges observed in some of these islands. This structural transformation is evident over a wide range of island sizes. However, it's intriguing to observe that exceptionally large islands within this composition show no discernible signs of such structural reorganization. In contrast, $Fe_{0.25}Ni_{0.75}$ islands consistently adopt a

hexagonal structure across all size variations, as shown in Figure 4.10 (a). This observation suggests that, the transition process in $Fe_{0.25}Ni_{0.75}$ islands appears to be independent of island size, highlighting the unique behavior of this composition.

Ni

As shown in Figure 4.10 (b), Ni islands consistently take on a hexagonal form across various sizes, similar to $Fe_{0.25}Ni_{0.75}$. There are no islands present on the narrow terraces, and the step edges are rough. From this observation it can be concluded that the islands that were once on these terraces have undergone melting at these step edges.

4.2.4 Annealing at 840 K for 60 minutes directly after deposition

In order to assess whether variations exist in the ultimate shape of islands following sequential heating or immediate heating after deposition, samples were prepared under identical conditions. These samples were subjected to direct heating at 840 K for 60 minutes. Similarly, the same experimental protocol was used to study the melting of the nanoparticles when heated directly after deposition, maintaining a temperature of 840 K for 90 minutes. Following a 60-minute heating at 840 K, a limited number of hexagonal $Fe_{0.25}Ni_{0.75}$ islands remain visible, with the majority featuring flattened edges, as depicted in Figure 4.11. These islands predominantly uphold their hexagonal structure, appearing relatively compact. The height of the islands is also unchanged. A narrow terrace can be observed on which there are no islands. Since the step edges are very rough, it can be assumed that any material that was on this terrace after deposition has now melted off at the step edges.

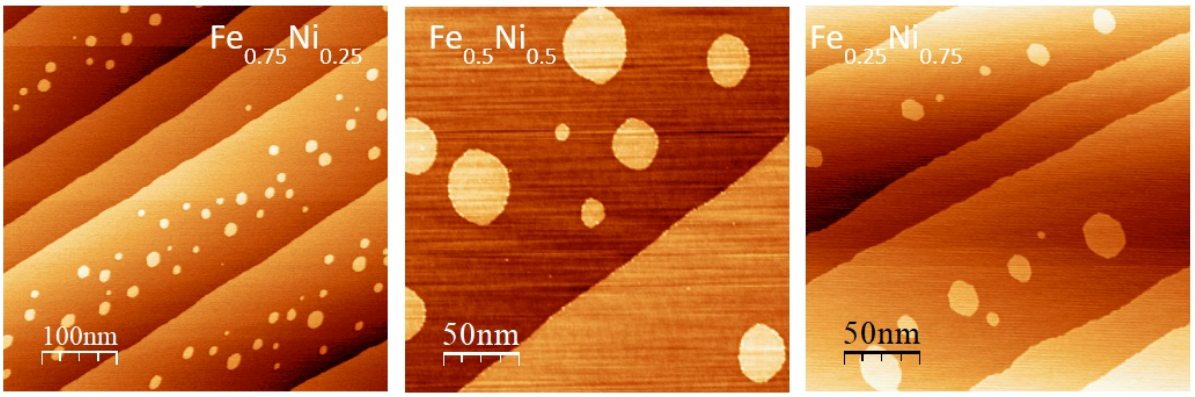

Figure 4.11: STM image of Fe_xNi_{1-x} islands on W(110) after 60 min annealing at 840 K directly after deposition.

4.2.5 Annealing at 840 K for 90 minutes directly after deposition

Fe and Ni

The last heating cycle results in a total heating time of 90 minutes. As can be seen in Figure 4.12, hexagonal islands are no longer present. As predicted by Reuter et al.

[39], the spreading behavior of Fe proved anisotropic, characterized by rapid expansion along the [110] direction and more gradual expansion along the [100] direction at 970 K. Remarkably, the configuration of the diffusion zone for Fe remained invariant, unaffected by both the initial material placement on the substrate and the annealing temperature up to 1070 K. As expected, the Fe nanoparticles melt completely and form a monolayer of uniform height after heating for 90 minutes immediately after deposition. These Fe islands have a compact and elliptically shape with the long axis along the $[1\bar{1}0]$. In contrast to Fe, the Ni islands begin to develop edges oriented in the [111] direction.

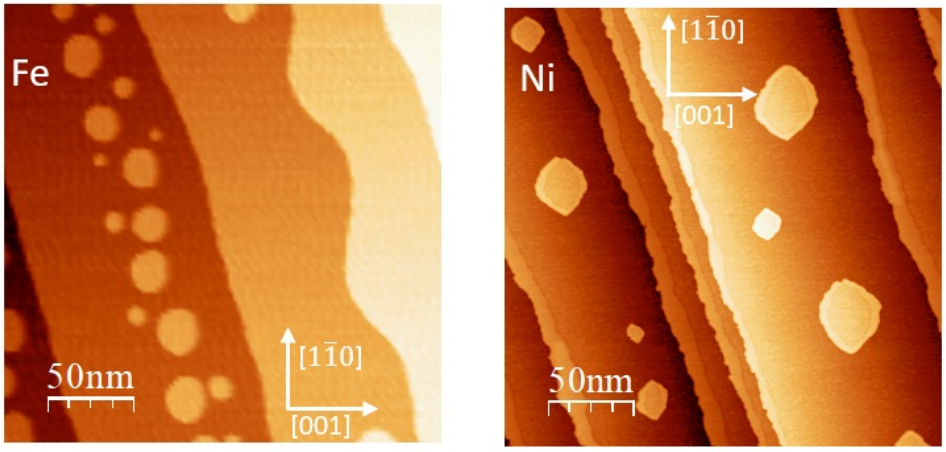

Figure 4.12: STM image of Fe and Ni islands on W(110) after 90 min annealing at 840 K, directly after deposition.

$Fe_{0.75}Ni_{0.25}$

All $Fe_{0.75}Ni_{0.25}$ islands have an anisotropic stretching in the $[1\bar{1}0]$ direction, as shown in Figure 4.13, which is caused by the crystallographic structure of the W(110) surface. Based on deductions drawn from experimental data obtained during growth experiments [87], it becomes evident that, in the cases of Fe and Ni, the initial monolayer undergoes pseudomorphic growth on the W(110) substrate, So they have bcc(110) structure. The inherent twofold symmetry of the bcc(110) surface naturally leads to anisotropic spreading, which accounts for the shape observed for FeNi islands.

$Fe_{0.50}Ni_{0.50}$

As observed in Figure 4.13, Similar to our previous observations, the height of the islands corresponds to the one monolayer. There is no noticeable change in the case of $Fe_{0.5}Ni_{0.5}$ with respect to the 60 minute heat treatment.

$Fe_{0.25}Ni_{0.75}$

The melting of a $Fe_{0.25}Ni_{0.75}$ island at a step edge can be directly observed in Figure 4.13. The islands have exclusively formed in a region slightly shifted to the sloped side, confirming the previous assumption. However, $Fe_{0.25}Ni_{0.75}$ have formed elongated islands.

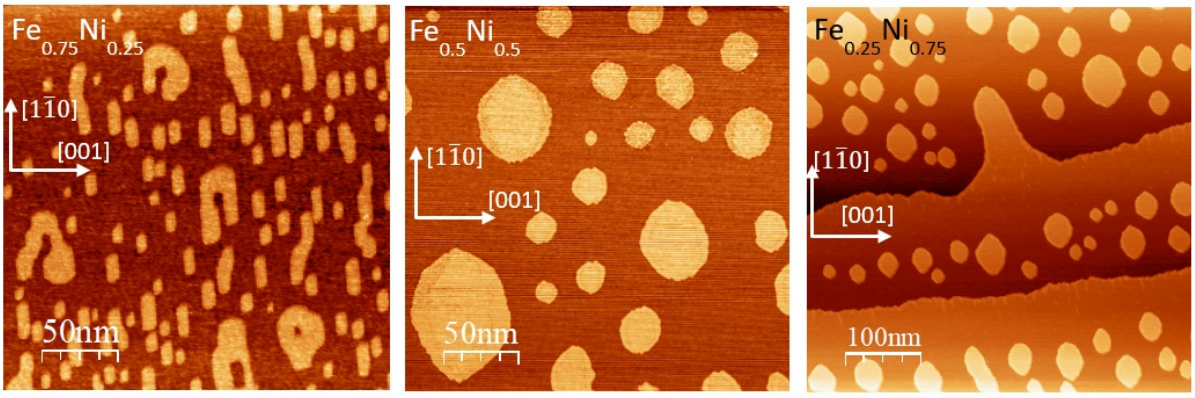

Figure 4.13: STM image of Fe_xNi_{1-x} islands on W(110) after 90 min annealing at 840 K, directly after deposition.

The arrangement of the islands' edges can be understood by referring to Figure 2.7. As previously mentioned, when an isolated atom 1 on the tungsten surface moves, it can diffuse in the [111] directions. If another atom 2 is positioned at an edge, located in the [1$\bar{1}$0] direction, relative to an already existing island or monolayer, it cannot diffuse along that edge because it cannot overcome an obstacle in the form of an on-top position. Instead, the atom 2 can only separate from the edge. On the other hand, an atom 3 can easily travel along the [111] edges of the island until it reaches a specific point 4, where it becomes attached. Consequently, the islands eventually develop edges in the [111] directions. Additionally, stable edges in the [1$\bar{1}$0] direction can be readily formed, as depicted in the figure, and presumably contribute to maintaining elongation while the [111] edges are being formed. Despite occasional instances of a decrease in aspect ratio in the [1$\bar{1}$0] direction, which remains somewhat unclear, the overall explanation stands.

Throughout the heating process, both the nickel and iron-nickel islands exhibit distinct variations in their structures, suggesting significant mobility of the edge atoms within these islands. In both cases, elongated elliptical and elongated hexagonal to hexagonal shapes are formed. The crucial difference, however, lies in the sequence of these shapes. Initially, after the first heating cycle, the nickel islands show both hexagonal and elongated elliptical shapes, while the iron-nickel islands show only elliptical shapes.

The behavior of melting in Ni and $Fe_{0.50}Ni_{0.50}$ nanoparticles was studied at 15-minute intervals at 830 K, and subsequent STM images were acquired after each cycle. This study was conducted as a bachelor's thesis [88]. Significant difference arose in the development of different island shapes. The occurring structures initially appeared similar for both sets of experiments, with elliptical structures elongated in the [1$\bar{1}$0] direction and hexagonal forms also elongated in the [1$\bar{1}$0] direction. However, the sequences in which these forms were developed differed. Nickel islands presented both shapes after the first heating cycle, gradually transitioning predominantly into the hexagonal form (with a few nearly hexagonal) before fully transitioning into the elliptical form. In contrast, FeNi islands first adopted the elliptical form entirely, followed by a size-dependent shift (small islands faster than large ones) to the hexagonal structure over an approximately 45-minute process (again, with a few nearly hexagonal), which they maintained until the end (Figure 4.14). The FeNi alloy was capable of forming significantly larger islands compared to nickel.

Moreover, a proportionally greater portion of the $Fe_{50}Ni_{50}$ alloy melted at the step edges compared to nickel. These observations collectively suggested higher mobility of the FeNi alloy compared to nickel. Furthermore, the transformation process of the iron-nickel

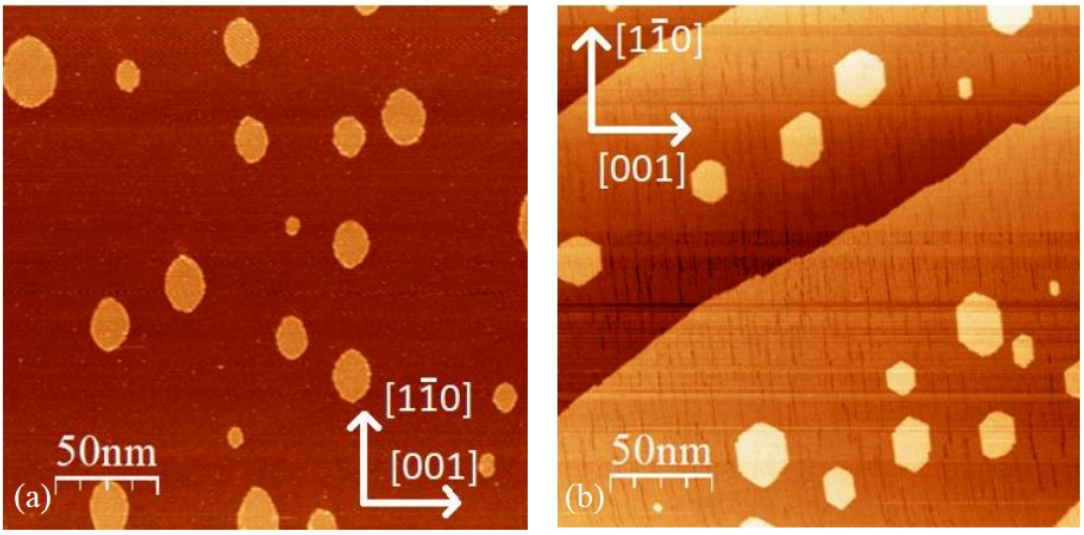

Figure 4.14: STM images of (a) Ni islands, U=0.05 V; I=0.8 nA, and (b) $Fe_{0.5}Ni_{0.5}$ islands, U=0.16 V; I=0.8 nA, after 120 minutes heating. Reprinted from the bachelor thesis supervised by me [88].

islands follows a size-dependent pattern, as smaller islands adopt the hexagonal structure more quickly. This size dependence is not observed for nickel islands. However, due to the overall smaller size of the islands and the slight blurring of the scanning tunneling microscopy (STM) images, which makes it more difficult to detect changes in the island edges, this observation cannot be definitively confirmed.

4.3 Crystal structure of the nanoparticles

The melting temperature of FeNi nanoparticles depends on both their size and their specific structural configuration. In order to elucidate and improve our understanding of the melting behavior of these particles with different stoichiometric compositions, we performed a crystal structure analysis and elemental mapping of the nanoparticles. The aim of this approach was to gain insight into the underlying factors that influence the way in which these nanoparticles undergo the melting process.

Therefore, this section of the chapter focuses on investigating the composition and form of the nanoparticles through a detailed description and analysis of the HRTEM images captured following deposition.

Sample preparation

$Fe_{0.75}Ni_{0.25}$, $Fe_{0.5}Ni_{0.5}$, $Fe_{0.25}Ni_{0.75}$ nanoparticles were produced using the magnetron sputtering source and deposited onto Graphene oxides on Lacy carbon on Cu grids (Plano, 400 mesh). The data presented in Figure 4.15 was obtained using a FEI Titan 80-300 transmission electron microscope (TEM) equipped with image aberration correction. The

microscope operates at an voltage of 300 keV and achieves a point resolution of 0.08 nm in TEM mode.

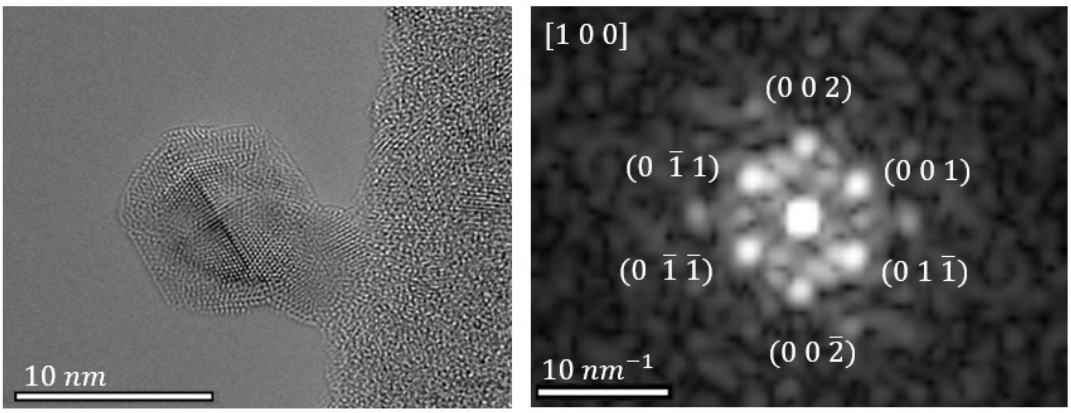

Figure 4.15: High resolution HAADF-TEM image of a $Fe_{0.5}Ni_{0.5}$ nanoparticle on the TEM grids.

The High-Angle Annular Dark-Field Transmission Electron Microscopy (HAADF-TEM) images provide visual evidence that the nanoparticles have a spherical shape and display a smooth surface. Additionally, the HRTEM images provide clear evidence of a distinct shell with lower contrast surrounding a darker core. Notably, lattice fringes are observed in both regions, indicating the presence of a crystalline structure. Furthermore, by applying the Fast Fourier Transform (FFT) analysis to the images, distinct reflections are identified, and their alignment with the [100] zone axis is confirmed. The FFT analysis helps in extracting and analyzing the spatial frequency information from the images. The presence of these prominent reflections at specific orientations indicates the crystallographic alignment of the nanoparticles.

A notable issue arises when subjecting the nanoparticle to an electron beam, as it experiences alterations in its structure, specifically involving the decrease in size of the core enriched with bright nickel (Figure 4.16). Consequently, conducting extended analysis under such conditions increases the likelihood of introducing errors.

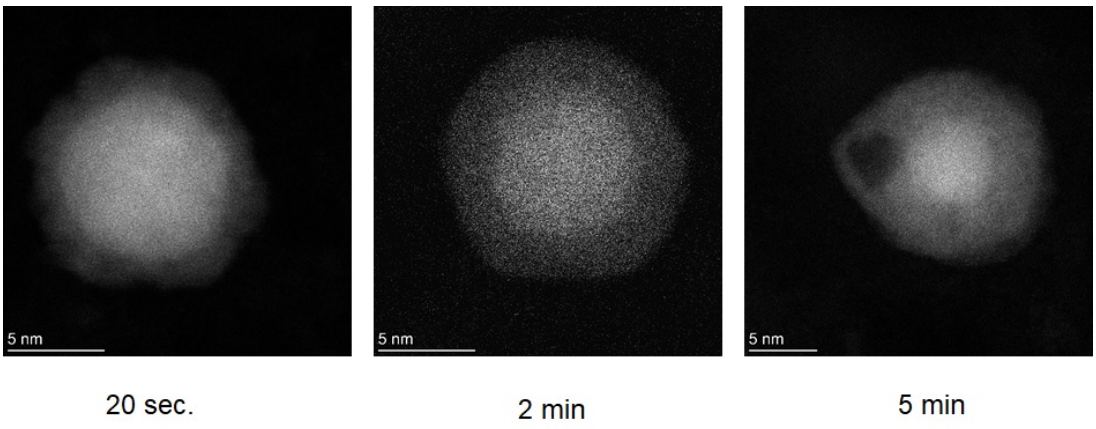

Figure 4.16: HAADF images of the states after electron irradiation

To address this issue, a proposed solution suggests cooling the sample to a temperature of -160 °C during the testing process. By decreasing the temperature, the aim is to

minimize or slow down the structural changes and subsequent reduction in core size. This cooling approach is intended to establish a more stable and dependable environment, ensuring the accuracy of the nanoparticle's structural analysis. The samples were subjected to microscopy at a temperature of -160 °C. However, despite the low temperature, the shape of the particles continues to undergo alterations. It means that the desired stability of the particle structure is not achieved even at this reduced temperature.

Considering this challenge, the only viable option that comes to mind is to change the microscopy conditions. Specifically, it is suggested to adjust the accelerating voltage from the standard 300 kV to a lower value of 60 kV. The rationale behind this change is to explore if using a lower accelerating voltage can help preserve the integrity of the particle shape during microscopy and potentially provide more accurate results. Regrettably, the nanoparticle measurement yielded no observable changes even with a lower high voltage. The persisting issue remains that the particle's structure undergoes alterations during the measurement, and this occurs within a few minutes. However, for a meaningful Energy-Dispersive X-ray Spectroscopy (EDX) measurement, a duration of 30-60 minutes is necessary to obtain a sufficient count of measurements. To address this challenge, the solution lies in utilizing the latest generation of EDX detectors capable of capturing numerous EDX counts within a short measurement time. Therefore, for this study, we have exclusively utilized measurements conducted with higher voltage settings (300 kV).

4.4 Elemental distribution

Figure 4.17 shows the Energy dispersive X-ray spectrum (EDX) acquired from a nanoparticle showing both Fe and Ni peaks suggesting that both element are present in the sample, C peak is from the graphene oxide grid and O from the air. The EDX line scan profile was

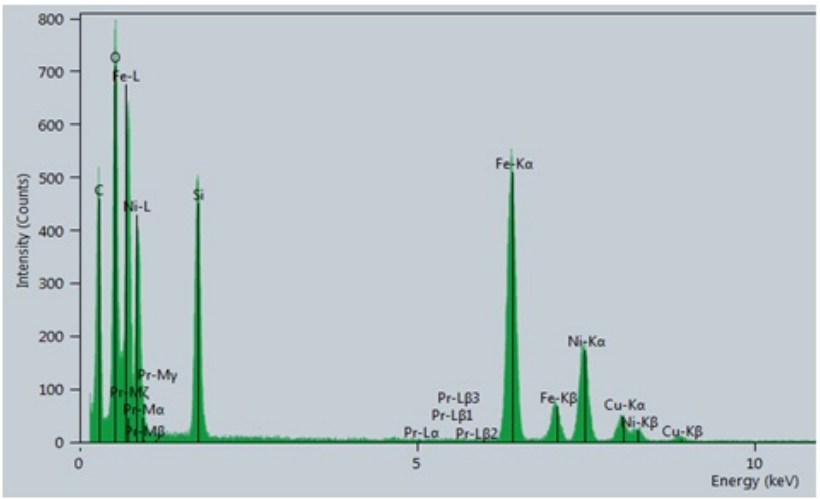

Figure 4.17: EDS spectrum of a $Fe_{0.5}Ni_{0.5}$ nanoparticle on the TEM grids.

utilized to determine the distribution of different elements within a single nanoparticle composed of two metals.

Figure 4.18 visually displays the elemental mapping and the line profile across a particle with a composition of $Fe_{0.75}Ni_{0.25}$. This line profile illustrates the intensity of Fe and

Ni in both the vertical and horizontal directions. Two different directions were chosen to examine whether there are any variations in the elemental composition along the line scan. The line profile of Ni demonstrates a distinct peak precisely at the location of the bright particle core, while the spectra on both sides of the core are predominantly influenced by Fe. At the core, the intensities of Fe and Ni are roughly equal. However, at the shell, there is a higher concentration of Fe, suggesting that Fe atoms are more likely to be found in those regions. On the other hand, the intensity of Ni at the edges is nearly zero. This increased Fe percentage at the edges can be explained by the nanoparticles having a higher atomic percentage of Fe compared to Ni, indicating a preferential distribution of Fe atoms towards the edges of the nanoparticle.

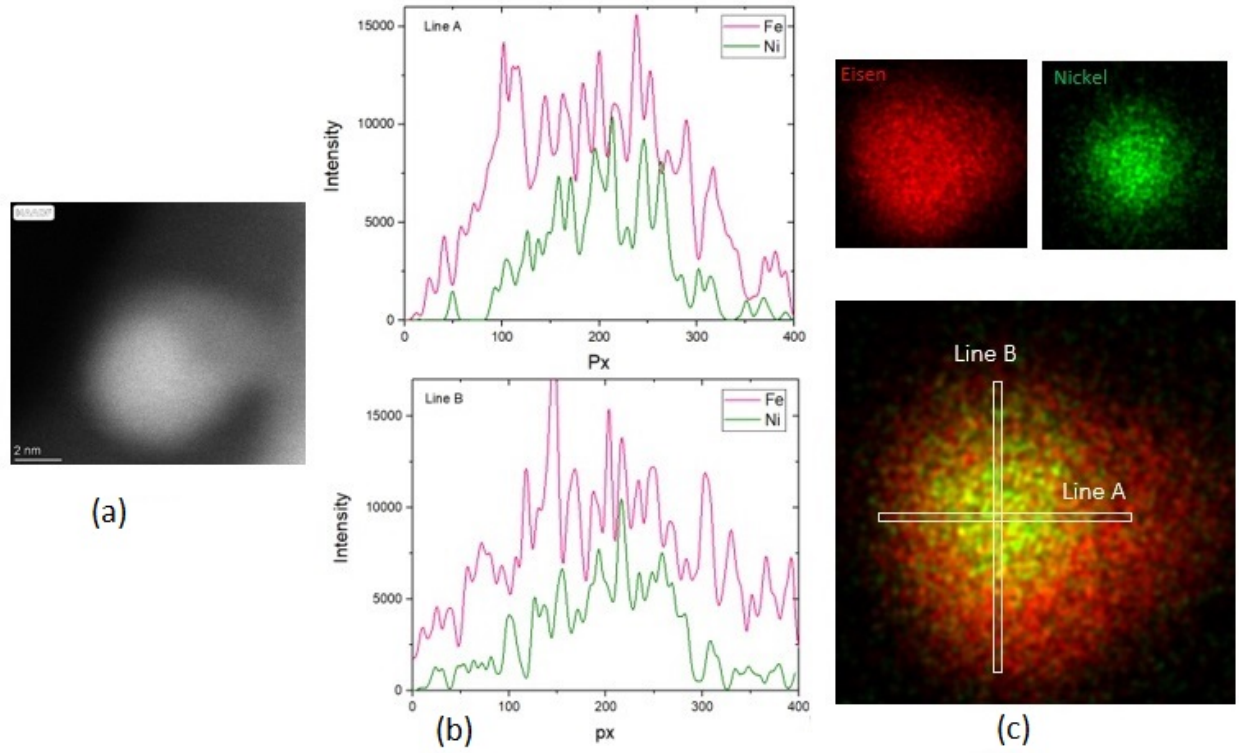

Figure 4.18: (a) High resolution HAADF-TEM image of a $Fe_{0.75}Ni_{0.25}$ nanoparticle on the TEM grids, (b) EDX line scan profile of a nanoparticles and (c) the elemental map of Fe and Ni with arrows indicating the EDX line scan direction.

Achieving this quantification is not possible due to two main reasons. Firstly, the poor signal-to-noise ratio makes it challenging to accurately measure and quantify the nanoparticles. The signal-to-noise ratio refers to the ratio of the desired signal (information about the nanoparticles) to the background noise or interference during the measurement. When the signal-to-noise ratio is low, it becomes difficult to obtain precise measurements and distinguish the nanoparticles' signal from the surrounding noise.

Secondly, the orientation of the nanoparticles can introduce a significant error in the quantification process. If the particles are oriented in different directions, it can lead to inconsistent measurements because the orientation affects the measurement outcome. This variation in orientation introduces additional uncertainty and can make it challenging to obtain reliable and reproducible results.

The EDS line profile of $Fe_{0.50}Ni_{0.50}$ demonstrates an equivalent intensity of Fe and Ni across the entire particle in both directions (Figure 4.19). This finding suggests that nanoparticles with an equal composition of Fe and Ni exhibit a uniform structure. The distribution of Fe and Ni elements within the particles is evenly dispersed, which is corroborated by the elemental mapping of the particle. This means that there is no significant variation in the concentration or arrangement of Fe and Ni atoms across the particle. Such a uniform distribution suggests that the Fe and Ni atoms have mixed thoroughly, forming a homogeneous alloy structure rather than distinct segregated regions of Fe and Ni.

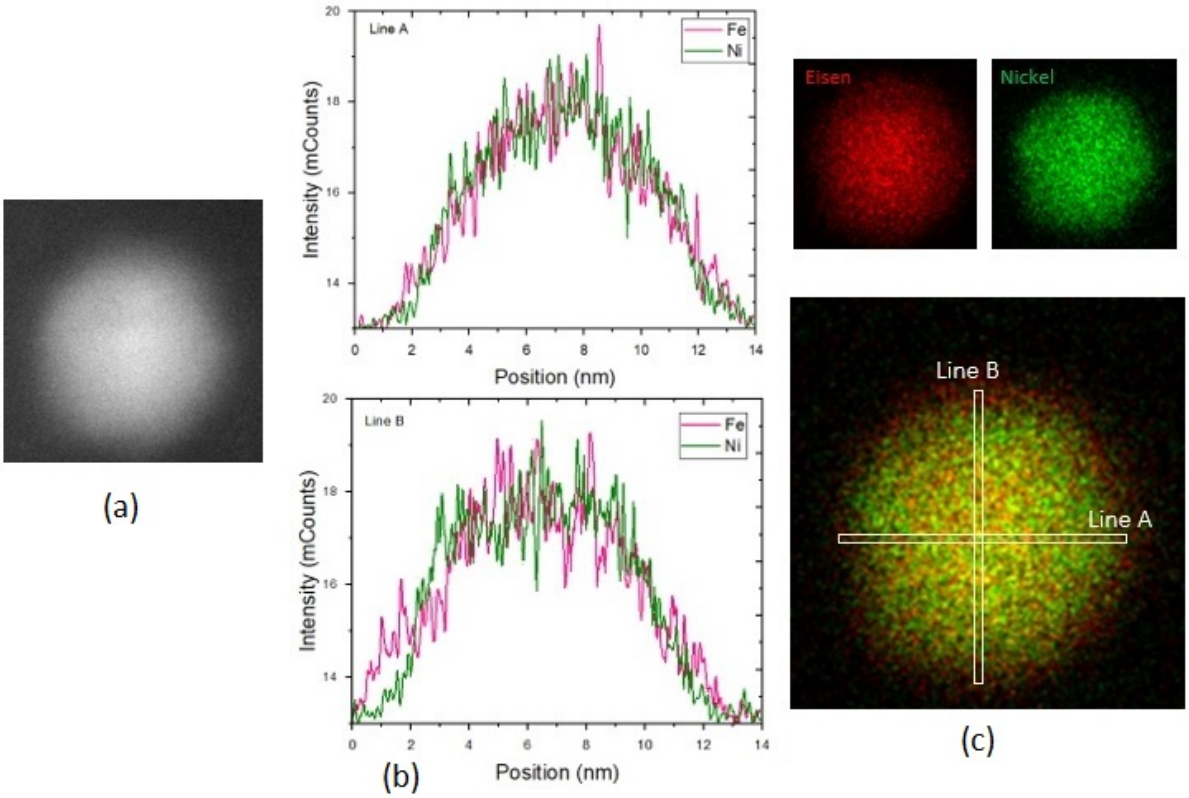

Figure 4.19: (a) High resolution HAADF-TEM image of a $Fe_{0.5}Ni_{0.5}$ nanoparticle on the TEM grids, (b) EDX line scan profile of a nanoparticles and (c) the elemental map of Fe and Ni with arrows indicating the EDX line scan direction.

An alternative method for acquiring detailed chemical information about intricate nanostructures involves obtaining a complete energy loss spectrum from multiple points across the particle in a HRTEM setup. This technique enables the extraction of linear variations in composition. It is important to note that in this setup, images are captured using a HAADF detector, which produces contrast based on density. Consequently, the particle cores appear brighter due to their higher probability of scattering. The EELS line scan profile presented in Figure 4.20 provides further insights into the elemental composition and distribution within the $Fe_{0.25}Ni_{0.75}$ particle. The graph displays the intensity variations of Fe and Ni across the particle's length. From the graph, it is evident that the intensity of Ni exhibits a distinct peak at the position of the particle's core. This

suggests that the core region predominantly consists of Ni atoms. On the other hand, the intensity of Fe is spread throughout the entire particle, indicating a more uniform distribution of Fe atoms.

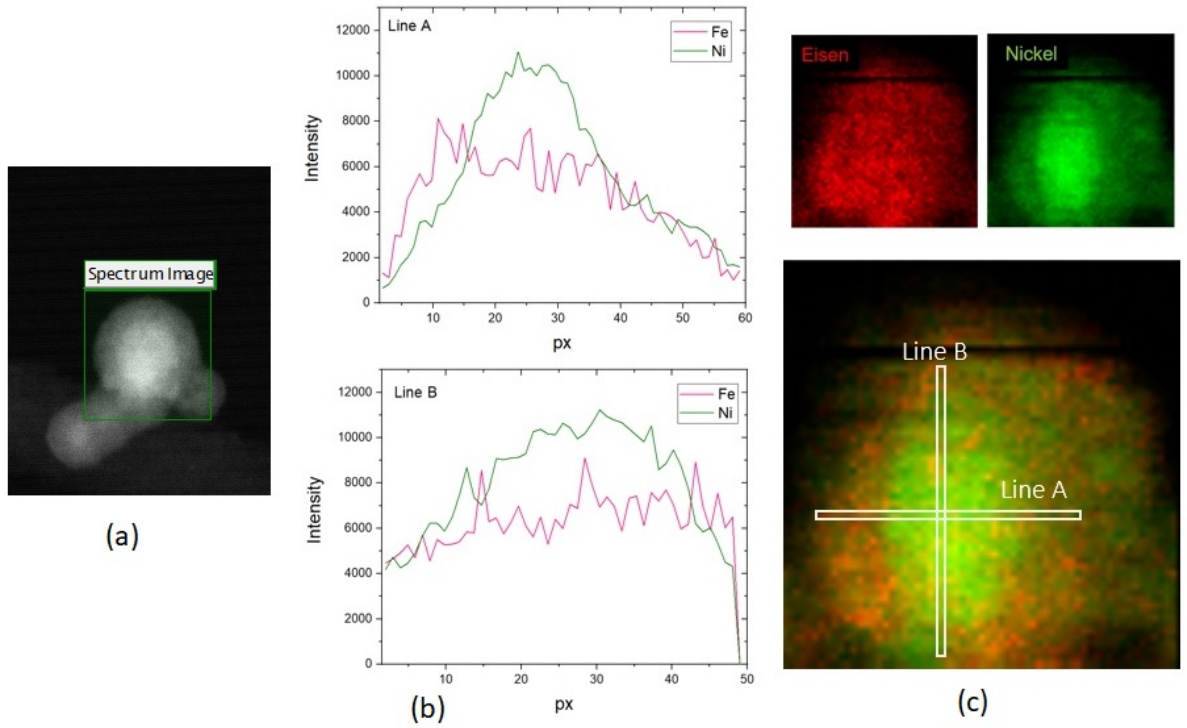

Figure 4.20: (a) High resolution HAADF-TEM image of a $Fe_{0.25}Ni_{0.75}$ nanoparticle on the TEM grids, (b) EELS line scan profile of a nanoparticles and (c) the elemental map of Fe and Ni with arrows indicating the EDX line scan direction.

The discrepancy in intensity distribution implies that Ni atoms have a higher concentration within the particle, while Fe is more evenly distributed. This observation suggests that the composition of the $Fe_{0.25}Ni_{0.75}$ particle is skewed towards Ni, with a greater fraction of Ni atoms compared to Fe. Furthermore, the gradual decrease in the intensity of Ni from the core towards the edge indicates that the presence of Ni becomes less pronounced as one moves away from the core region. This trend suggests a transition in the elemental composition or a shift in the atomic arrangement from the core to the particle's surface.

In the $Fe_{0.25}Ni_{0.75}$ case, Ni accounts for a larger proportion of the overall composition, while Fe represents a smaller fraction. This stands in contrast to the previous sample, where the opposite was observed. However, in both cases, it is evident that Ni atoms tend to occupy the core sites of the particle, while Fe atoms are predominantly found at the surface sites.

To better understand the results, a mathematical approach using error functions was utilized. This method helps us depict how materials are distributed within a core-shell structure. Imagine a round particle: as you go from its center towards the surface, we are interested in how the concentration of different materials alters. The radius of the core is denoted as r_1 and the radius of shell is denoted as r_2 (see Figure 4.21). So the radial

distribution of material in the core is expressed as:

$$s_1 = 2\sqrt{2r_1(x-d) - (x-d)^2}$$

likeweis the radial distribution of material in the shell is expressed as:

$$s_2 - s_1 = 2\sqrt{2r_2x - x^2} - 2\sqrt{2r_1(x-d) - (x-d)^2}$$

Where d represents the thickness of the shell. In theory, the set of these two functions

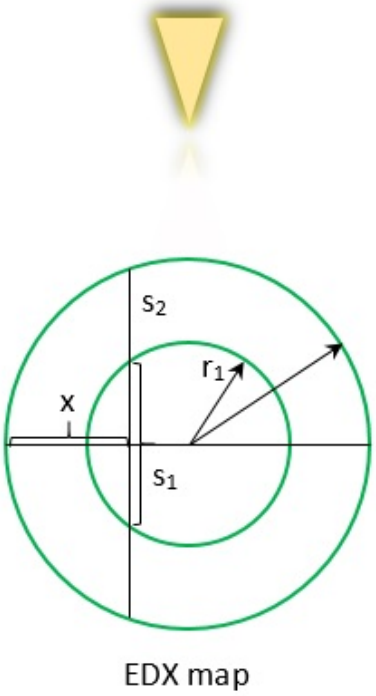

Figure 4.21: Schematic representation of the acquisition of a HRTEM-EDX map of a core-shell nanoparticle.

has the potential to characterize any TEM-EDX map derived from a spherical core/shell particle with a distinct interface and surface. In the specific systems that were investigated in this research, a notable portion of the material from the core is found within the shells of the particles. Additionally, the material constituting the shell is dispersed throughout the structure. This complex arrangement contrasts with the ideal scenario of a clear distinction between the core and shell. To tackle this complex configuration and the absence of a well-defined core-shell boundary, certain modifications are made to the equations, so the radial distribution of Fe and Ni is expressed as:

$$c_{Ni} = s_1 + p(s_2 - s_1)$$

$$c_{Fe} = s_2 - qs_1$$

where p and q represents the proportion of the remaining core material in the shell. We also used error functions to estimate the boundary between the core and the shell.

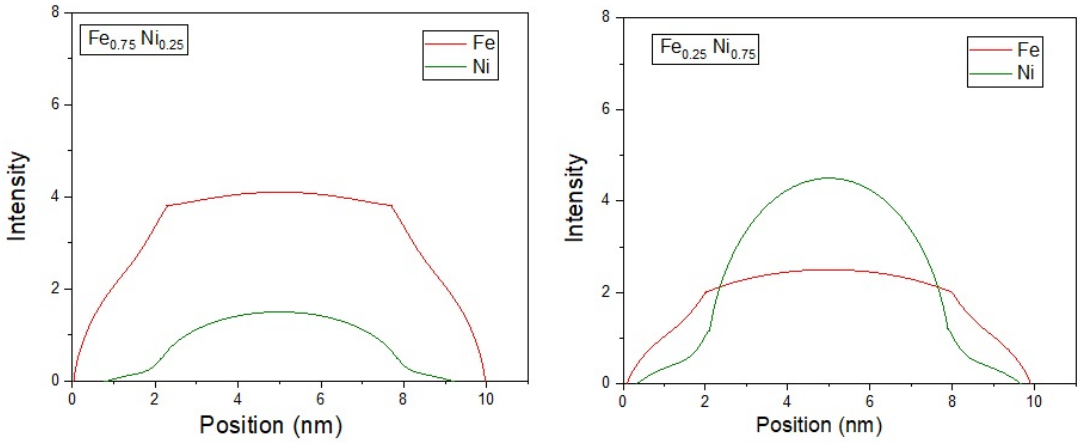

Figure 4.22: Radially averaged EDX data with corresponding stoichiometry include δ-function for a nonsharp interface.

The distribution pattern of elements as revealed by this analysis is depicted in Figure 4.22. The measurement identified a broadening of 0.3 nm at the core/shell interface. The core primarily contains Ni atoms, and the fraction of Ni is higher in the core compared to Fe. This means that Ni atoms prefer to be concentrated in the core region. As we move from the core to the shell, the fraction of Ni atoms gradually decreases, creating a decreasing gradient of Ni concentration. However, even in the shell, there are still some Ni atoms present, but their fraction is lower compared to the core. In contrast, the arrangement of Fe atoms is different. Fe atoms have a greater tendency to disperse throughout the particle. However, the proportion of Fe atoms within the shell is significantly greater than that within the core. It's worth noting that a noticeable fraction of Fe remains in the core, and its contribution is particularly pronounced in the case of $Fe_{0.75}Ni_{0.25}$ particles. To achieve a higher level of precision in the outcome, it is necessary to match the generated graph with the pattern derived from EDX or EELS analysis. This matching would enable the determination of the precise proportions of iron and nickel atoms within the nanoparticle. However, for the reasons mentioned above, quantification was not possible. In this calculation, the atomic composition of iron and nickel has been taken into account exactly according to stoichiometry.

This observation (Figure 4.22) suggests a preferential distribution of Ni towards the core region, indicating that Ni atoms have a higher affinity for occupying the central positions within the particle structure. On the other hand, Fe atoms tend to reside closer to the outer regions, resulting in their prevalence at the particle's surface. So, the core of the nanoparticle is enriched with Ni atoms, while the shell has a higher fraction of Fe atoms. The transition from the core to the shell leads to a gradual decrease in Ni concentration and a relative increase in Fe concentration.

Typically, the melting point of bimetallic systems falls between that of their monometallic counterparts, depending on the size and stoichiometry of the system and possibly its structural arrangement. As can be seen in this work, variations occur in bimetallic systems with the same size range but different compositions upon heating. In the case of $Fe_{0.75}Ni_{0.25}$ and $Fe_{0.25}Ni_{0.75}$, where a Ni core is surrounded by a Fe shell,

all nanoparticles completely liquefy upon the first heating cycle (540 K). Islands with a higher Fe fraction consolidate into compact formations, while $Fe_{0.25}Ni_{0.75}$ adopt more branched structures. This difference is attributed to the robust bonding between Ni and the surface, as discussed earlier. In contrast, the $Fe_{0.50}Ni_{0.50}$ nanoparticles, characterized by an alloy structure, where Fe and Ni are homogeneously dispersed within the particle—initiate melting around 540 K. During this process, they exhibit an unrolling carpet behavior. This phenomenon indicates that the FeNi nanoparticles with an alloy structure possess a higher melting temperature than those with a core-shell configuration. This holds true when compared to particles with either a higher or lower Ni content.

In addition, the nanoparticles begin to melt from their outermost shell. In the case of $Fe_{0.75}Ni_{0.25}$ nanoparticles, it's important to note that the outermost layer is predominantly Fe. This structural feature is responsible for the remarkable similarity between the way these nanoparticles melt on tungsten and the behavior of pure Fe nanoparticles during melting processes.

4.5 FeNi nanoparticles on graphene

When metal nanoparticles are deposited onto a metal surface, such as tungsten, there exists a considerable similarity in crystal lattice structures and electronic properties. This similarity leads to the establishment of strong metal-metal bonds, as the electronic configurations of both the nanoparticles and the metal surface align favorably. However, when metal nanoparticles are deposited onto a nonmetal surface like graphene, a notable departure in electronic structure becomes apparent. Graphene, being nonmetallic, possesses distinctive electronic properties that contrast with those of metal nanoparticles. This electronic mismatch impedes the establishment of strong chemical bonds between the nanoparticles and the graphene surface. Instead, weaker interactions, particularly van der Waals forces, play a more significant role due to the absence of shared electronic states. To explore this phenomenon, we undertook an investigation focused on the melting behavior of FeNi nanoparticles. Our initial focus was on observing their response on a tungsten surface, which has a metallic character, with the aim of unraveling the nuanced interactions inherent to metal-metal interfaces. Subsequently, driven by the intention to capture the contrasting dynamics, we delved into the melting behavior of FeNi nanoparticles on a graphene surface - a quintessential example of interactions involving non-metallic substrates. This investigation allowed us to identify the distinct characteristics that govern the mobility of the nanoparticles after heating cycles.

In this section, the synthesis process of graphene on a thin Cobalt film using CVD methods is outlined. The effects of varying conditions, such as temperature and pressure of Propene gas, are discussed. Furthermore, the structural transformation of size-selected FeNi nanoparticles on the graphene surface upon heating is investigated. These experiments were conducted as a component of a PhD project, two master's projects, and one bachelor's project.

4.5.1 Cobalt thin film on W(110)

The initial stage in the synthesis of graphene on a Cobalt thin film involves preparing the thin film. The deposition rates and resulting surface structure are assessed using STM (Scanning Tunneling Microscopy) and LEED (Low-Energy Electron Diffraction). LEED can be employed for structural analysis to identify any alterations in the crystal structure within the thin film. Figure 4.23 (a) depicts Cobalt (Co) on the W(110) surface with a coverage below approximately 1 monolayer (ML). At this stage, there are no significant qualitative changes visible in the LEED pattern. However, as the Co coverage increases, additional spots emerge in the LEED pattern, as demonstrated in Figure 4.23 (b) These extra spots gradually diminish with further coverage until the LEED pattern transforms into a simple 1×1 hexagonal pattern, representing the expected Co basal plane. These extra spots remain observable up to a Co coverage of 4 ML.

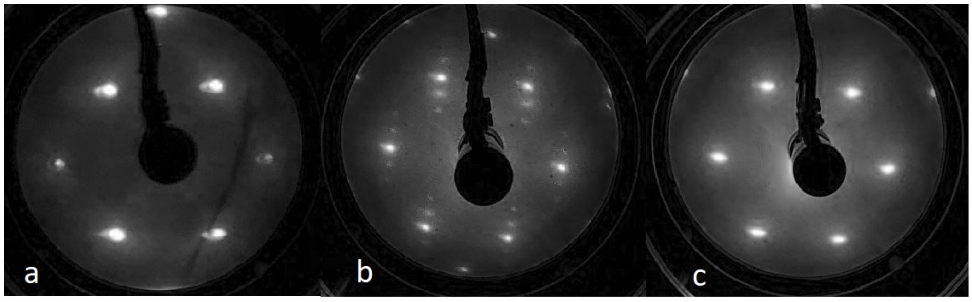

Figure 4.23: LEED images of a) Co overlayer below 1 ML (96 eV), b) less than 4 ML (96.6 eV), c) 4 ML Co/W(110) (89 eV)

Therefore, the LEED pattern undergoes two drastic changes at specific coverages: the first one occurs at 1 ML coverage, transitioning from pseudomorphic W(110) to a (4×1) pattern. The second significant change occurs at 4 ML coverage when the extra spots completely fade, as explained in section 3.9.

Figure 4.23 illustrates the LEED pattern, which clearly shows the close-packed Co(0001) structure. This pattern was observed after a deposition period of 7 minutes. As a result, the deposition rate can be calculated as 4 monolayers (ML) every 7 minutes at constant cobalt ejection rate of 70 nA.

After the initial two monolayers, Cobalt (Co) demonstrates three-dimensional island growth. Consequently, an unannealed Co thin film comprising 16 closed monolayers exhibits a highly rough surface, as shown in Figure 4.24 (a). The islands found in the thin film have diameters ranging from 10 to 30 nm, and their heights vary between 2 and 5 nm. When the thin film is annealed at 673 K, the islands become slightly larger, with diameters reaching up to 50 nm, but their height remains unchanged. The STM image depicted in Figure 4.24 (b) displays significantly larger islands compared to the STM images of Co thin film before annealing. These islands form after annealing 16 monolayers (ML) of Cobalt (Co) at 773 K for 60 minutes. The islands have diameters measuring several hundred nanometers and reach a maximum height of 20 nm. They possess an almost atomically flat surface, making them ideal for graphene synthesis.

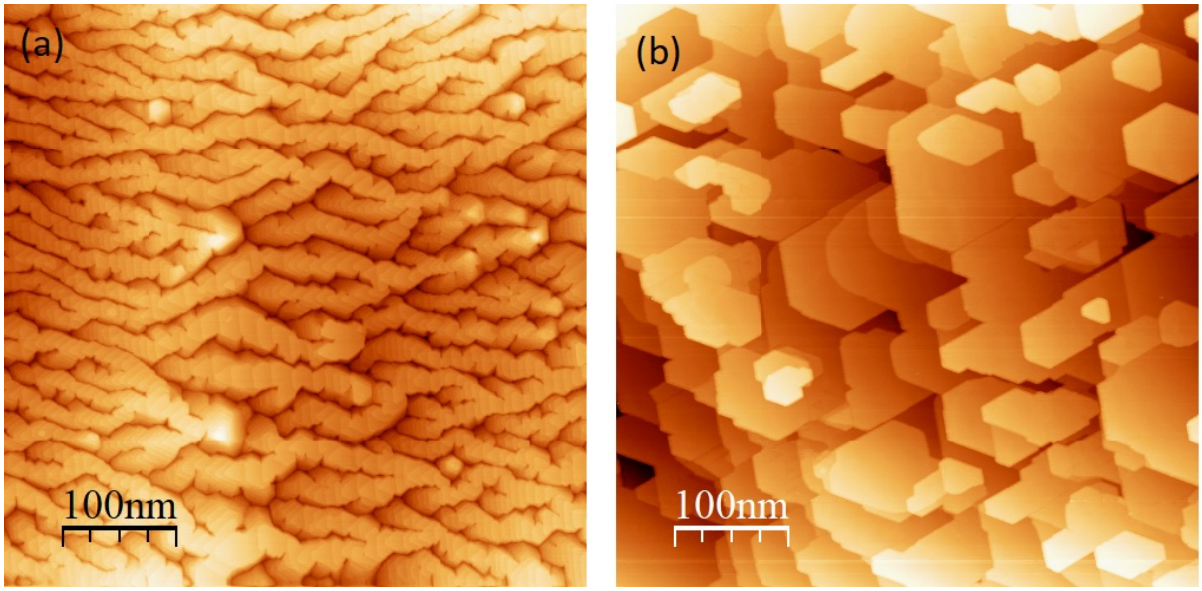

Figure 4.24: STM images of 16 ML Co on W(110), a) after deposition and b) after heating at 673 K (1 V, 0.8 nA).

4.5.2 Graphene on a cobalt thin film

Once again, the process of synthesizing graphene involves using CVD (Chemical Vapor Deposition) with propylene at a substrate temperature of 773 K. The formation and characterization of graphene on a thin Co film under different conditions was investigated as a bachelor thesis [89]. The investigation involved varying the propene gas pressure, annealing time, and annealing temperature with the aim of developing a technique to achieve a complete monolayer of graphene on Co islands. Following the preparation of a smooth Co(0001) thin film through the deposition of 16 ML Co on W(110) and subsequent annealing at 773 K, the CVD process is carried out in a propylene atmosphere at a pressure of 10^{-7} mbar for a duration of 6 minutes. The STM images taken after cooling the surface to room temperature suggest that the amount of propene gas used is insufficient. Figure 4.25 shows the corresponding STM image.

The annealing duration was carefully chosen to be between 5 and 10 minutes, while the annealing temperature ranged from 720 to 820 K. The amount of propene gas was varied between 10^{-7} and 10^{-6} mbar. However, in the pursuit of a uniform graphene layer on Co(0001), the subsequent course of action requires increasing the available carbon, and the optimal annealing temperature for achieving the most favorable result was determined to be 500 °C [89]. The outcome of heating the Co thin film to 773 K and substantially augmenting the carbon content under a pressure of 1.6×10^{-6} mbar is illustrated in the STM image in Figure 4.26. The graphene layer appears to be uniform and consistent, exhibits good quality, and a Moiré pattern is visible. The Moiré pattern arises due to the slight mismatch in periodicity between the two materials, resulting in an interference pattern when they are overlaid. This result is quite interesting because it shows that graphene prefers to grow on the flat surface rather than on the step edges. Also, the mobility of atoms seems to be high enough to allow the formation of a large graphene sheet, leaving large areas almost free of carbon. LEED analysis shows a graphene layer

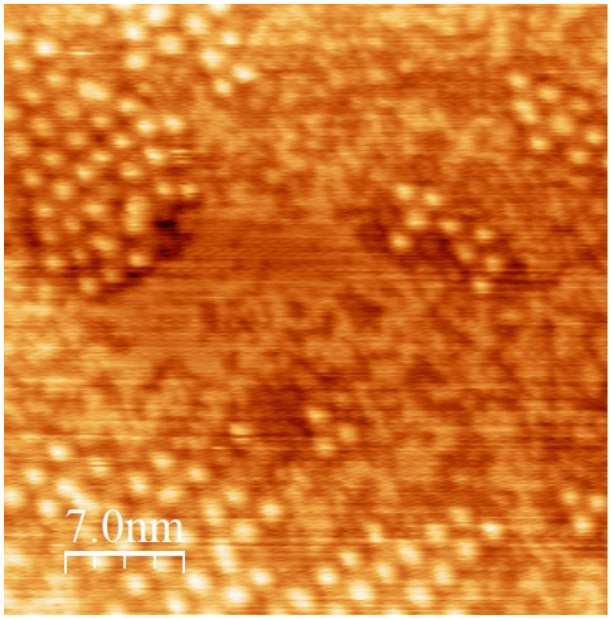

Figure 4.25: STM images of incomplete graphene on Co/W(110) (1 V, 0.08 nA). From the bachelor thesis supervised by me [89].

with the Moiré pattern, hexagonal cobalt and the tungsten spots (Figure 4.27).

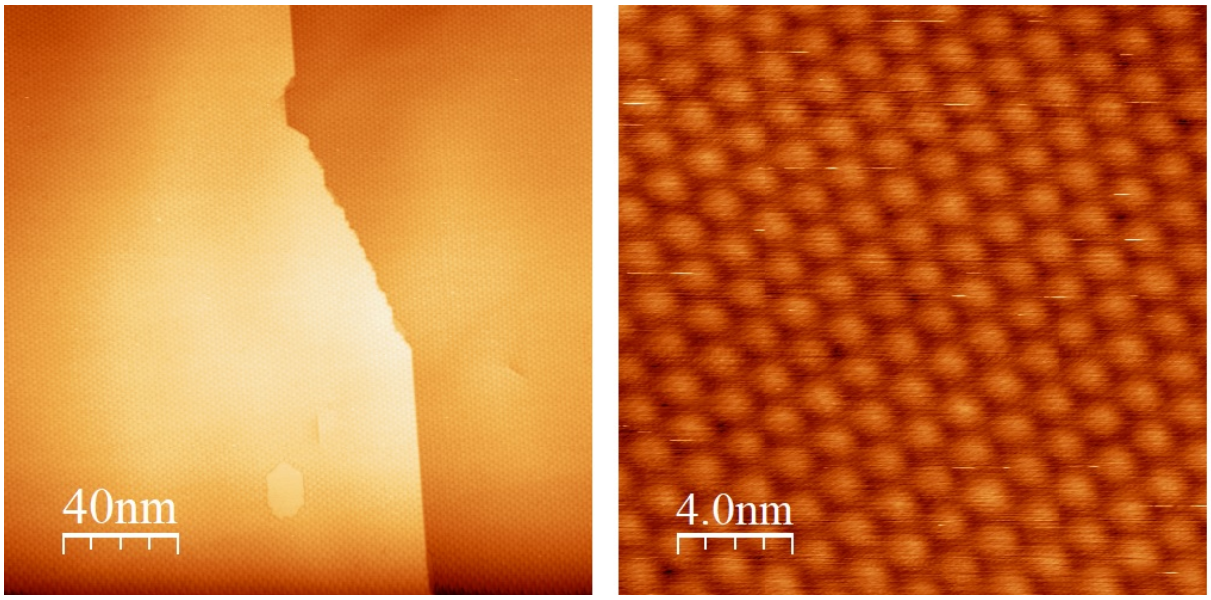

Figure 4.26: STM images of graphene on Co/W(110) (1 V, 0.8 nA).

4.5.3 FeNi nanoparticles on graphene/ Co(0001)/ W(110)

The nanoparticles are examined through their deposition at a perpendicular angle onto the prepared graphene surfaces, following the outlined procedure in section 4.2.2. Using a magnetron cluster source, $Fe_{0.50}Ni_{0.50}$ nanoparticles are introduced onto the graphene

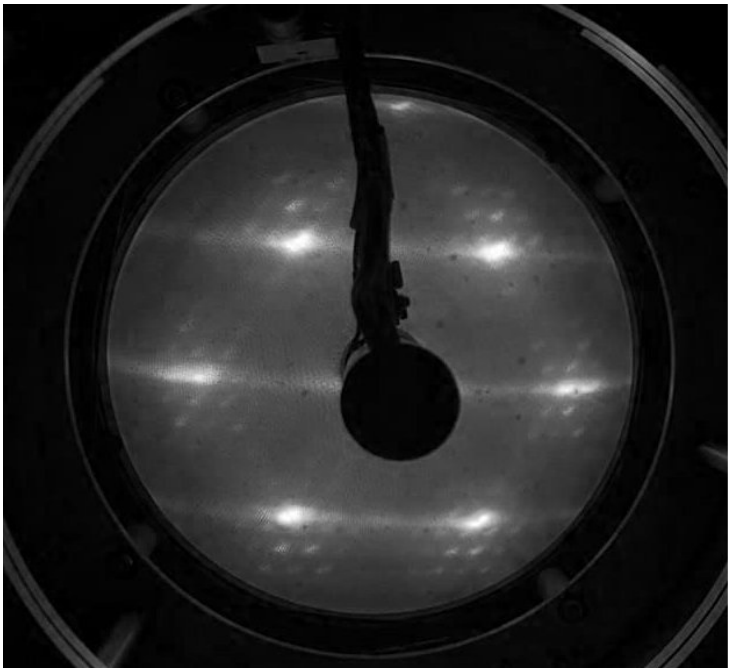

Figure 4.27: LEED image of graphene on Co/W(110) (E=92 eV).

layer. As part of a master's project, the investigation was centered on the behavior of these size-specific nanoparticles after subsequently heating on the graphene surface.

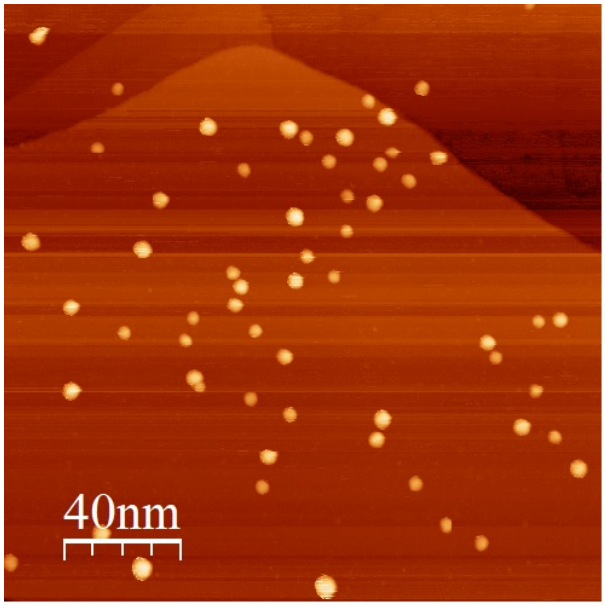

Figure 4.28: STM image of $Fe_{0.50}Ni_{0.50}$ nanoparticles deposited on graphene on Co/W(110) at room temperature (1 V, 0.08 nA).

We aimed to investigate particles having sizes of 2 nm or smaller as part of our objective. Figure 4.28 displays an STM image of $Fe_{0.50}Ni_{0.50}$ nanoparticles deposited on graphene at room temperature with the selected size of 1.8 nm. The image section contains approximately 60 nanoparticles that are randomly distributed across the sub-

strate. Notably, no specific preference for terraces or step edges as deposition sites for the nanoparticles is observed. Furthermore, there is no noticeable agglomeration (accumulation at certain locations) of the particles. The considerable mobility of particles on the graphene surface posed a challenge, preventing the capture of STM images of individual particles. As a result, the STM image presented in Figure 4.28 stands as the sole attainable representation. so we decided to produced larger nanoparticles to see the melting behavior after tempering. Nanoparticles of $Fe_{0.50}Ni_{0.50}$ with size of (3.0±0.6) nm, (3.5±0.7) nm, and (4.77±0.59) nm were selected in this project. Surprisingly, no discernible differences in results were observed between the samples after heating. The most favorable outcome from this experimentation is depicted below [90].

The majority of the nanoparticles exhibit similar shapes and sizes. Importantly, neither the graphene substrate nor the nanoparticles show any visible signs of damage caused by the deposition, indicating that the soft landing condition is met.

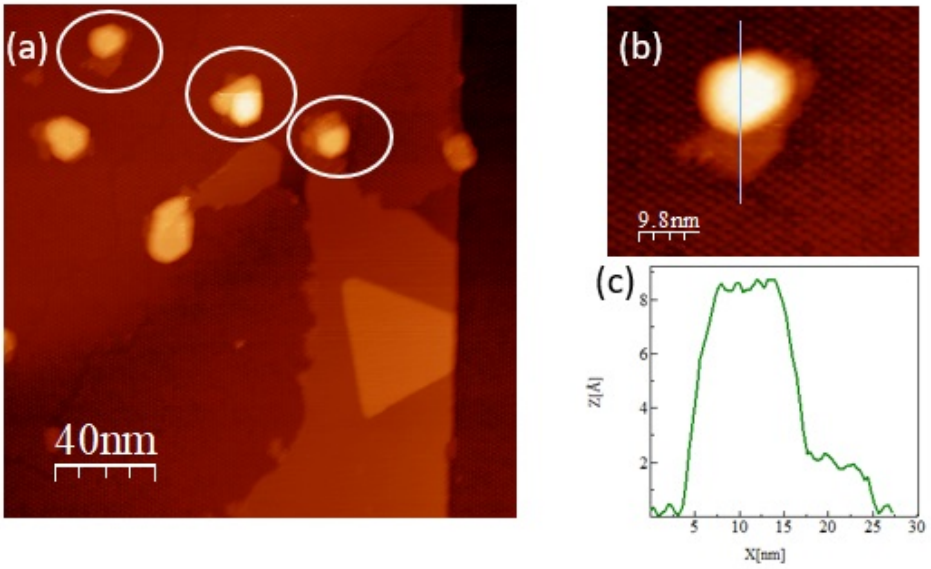

Figure 4.29: STM image of $Fe_{0.50}Ni_{0.50}$ nanoparticles deposited on graphene on Co/W(110) after heating at 673 K for 30 minutes (1 V, 0.8 nA). From the master thesis supervised by me [90]

Nanoparticles with the selected size of 4.77 nm were deposited on the graphene. After heating at 573 K, it can be seen in figure 4.29, after the heating process at 673 K for 30 minutes, the particles undergo a transformation and develop a flat carpet-like structure surrounding their centers. Figure 4.30 shows the STM image of nanoparticles after subsequent tempering at 720 K and 820 K for 30 min. As the temperature increases, the particle height decreases, and the height distribution becomes more narrower. The particles continue to flatten, and their edges gradually assume angles of 60° and 120° . Analyzing the distribution of smaller particles, it is evident that after heating to 820 K, the majority of particles have a height below 3 atomic layers (AL), while a substantial number of particles still exhibit a height above 1 AL.

For another set of samples with particle sizes selected at 3 nm and 3.5 nm, the particles located on the Co islands experienced a reduction in height to less than 2 nm after exposure

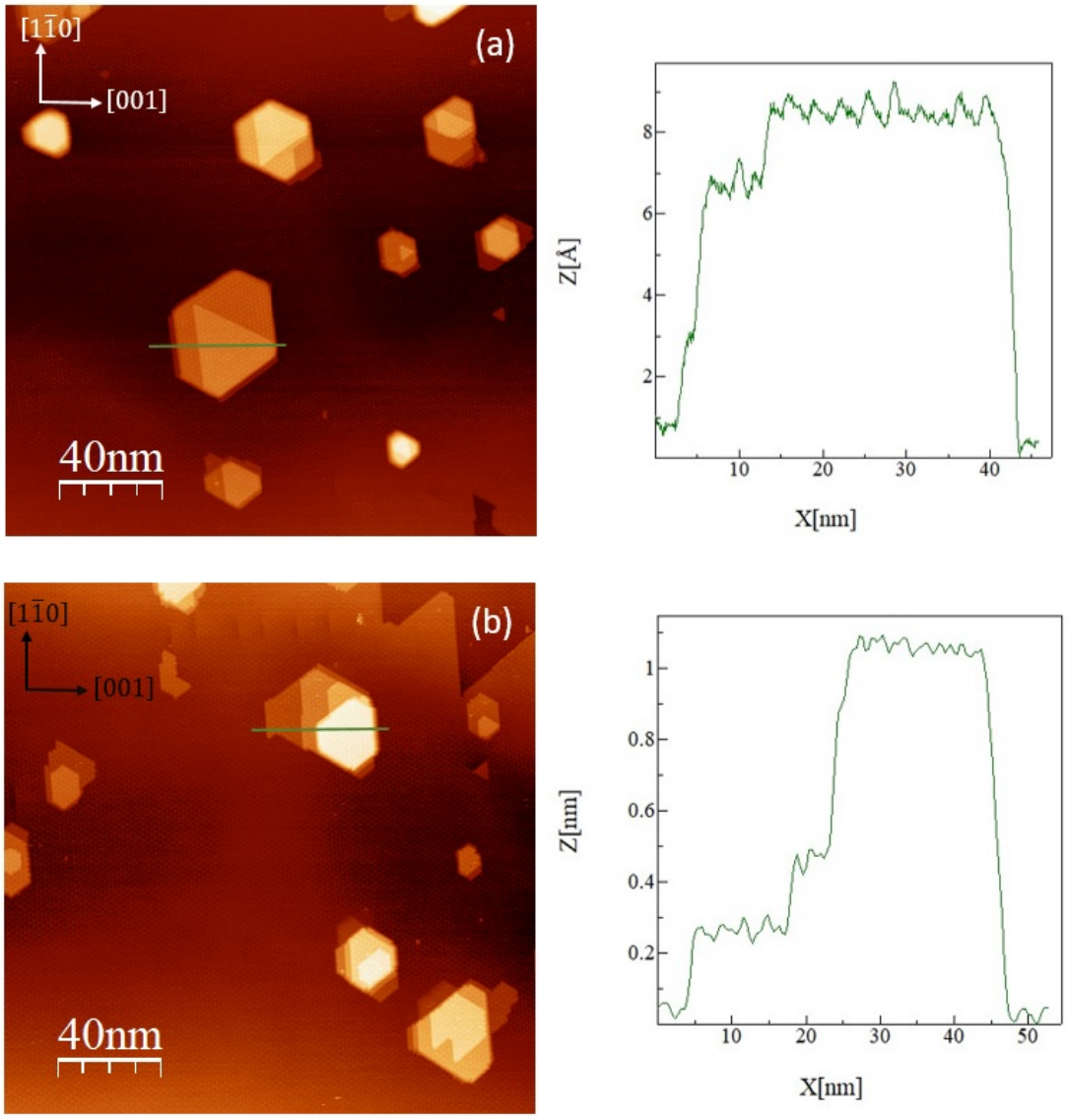

Figure 4.30: STM image of $Fe_{0.5}Ni_{0.5}$ nanoparticles deposited on graphene on Co/W(110) after subsequently heating at (a) 720 K and (b) 820 K for 30 minutes. From the master thesis supervised by me [90]

to 720 K. However, particles positioned between the Co islands could still retain heights greater than 3 nm. A notable change observed was that a majority of the particles located on the Co islands developed an unrolling carpet, with certain particles exhibiting linear edges aligned with the Moiré pattern of the underlying surface. When the system was subjected to a temperature of 820 K, the surface of the Co islands was found to be particle free. After this heating process, the Moiré pattern was no longer detectable.

5 Conclusion

This chapter presents an overview and summary of the projects conducted. The conclusion is divided into two primary sections. The first part centers on the synthesis of FeNi nanoparticles with varying stoichiometry, along with their melting behavior after annealing and the structural characterization. The second part refers to the synthesis of graphene and the characterization of nanoparticles deposited on the graphene surface.

5.1 FeNi nanoparticles on W(110)

The main focus of this study is to explore the melting behavior of FeNi nanoparticles with varying stoichiometry. Three types of FeNi alloys, namely $Fe_{0.75}Ni_{0.25}$, $Fe_{0.5}Ni_{0.5}$, and $Fe_{0.25}Ni_{0.75}$, as well as pure nickel and iron, were utilized in the investigation. The nanoparticles were synthesized using a nanocluster source. High-resolution transmission electron microscopy (HRTEM) was employed to examine the morphology and crystal structure of the nanoparticles.

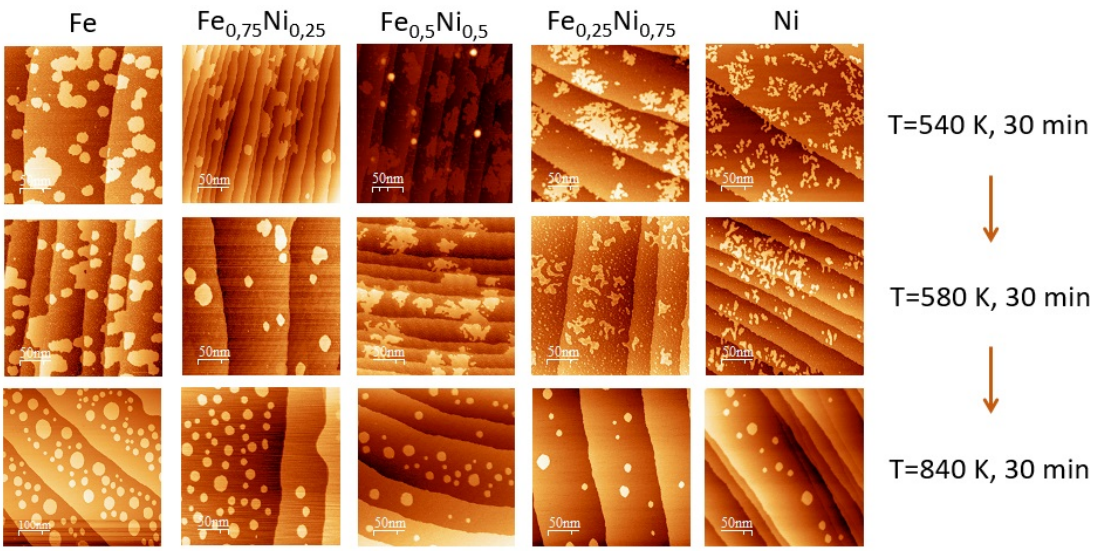

Figure 5.1: Results of the nanoparticles' melting behavior.

Scanning tunneling microscopy (STM) was used to gather information about the size and mobility of the nanoparticles after deposition, as well as details about their melting behavior and the configuration of the islands following tempering. The results revealed that the average particle size is consistent with the size selected using quadropole mass filtering. In conclusion, all nanoparticles exhibited a spherical shape, and there was no preference for specific adsorption sites. The heating cycles provided important insights

into the evolution of nickel and iron-nickel islands on tungsten (Figure 5.1). Initial melting at 540 K formed compact monolayer islands, the nanoparticles exhibited an "unrolling carpet" behavior. At around 580 K, nickel islands spread anisotropically, merging through dynamic coalescence. The absence of decreased small island frequency indicated Smoluchowski ripening. At 840 K, fully compact islands are formed, with iron islands growing larger due to higher mobility. Iron-nickel islands transformed from elongated elliptical to hexagonal shapes, showing size-dependent behavior. This transformation sequence differed from nickel islands. Overall, these findings enhance our understanding of island growth and composition effects.

Elemental mapping and line profile analysis using energy-dispersive X-ray spectroscopy (EDS) highlighted variations in Fe and Ni distribution within the particles. $Fe_{0.75}Ni_{0.25}$ particles exhibited a core enriched with Ni, while $Fe_{0.5}Ni_{0.5}$ particles showed uniform Fe-Ni distribution. Electron energy loss spectroscopy (EELS) line scans confirmed Ni enrichment in $Fe_{0.25}Ni_{0.75}$ particle cores, while Fe was more uniformly distributed. This observation indicated a preferential distribution of Ni in the core and Fe at the surface. Observations show distinctive melting responses to heat for FeNi particles of the same size but different compositions. $Fe_{0.50}Ni_{0.50}$ nanoparticles, which are characterized by their alloy structure, start melting at about 540 K. In contrast, $Fe_{0.75}Ni_{0.25}$ and $Fe_{0.25}Ni_{0.75}$ nanoparticles, which consist of a Ni core surrounded by an Fe shell, undergo complete liquefaction at 540 K during the first heating cycle. Consequently, these results suggest that nanoparticles with an alloy structure tend to have a higher melting temperature compared to those with a core-shell configuration.

Outlook Capable of capturing numerous EDX counts within a short measurement period could offer insights into nanoalloy structures in relation to their composition. The next step could be employing EDX detectors of the latest generation, which are capable of capturing numerous EDX counts within a short measurement period could offer insights into the structural features of nanoalloys in relation to their composition.

5.2 FeNi nanoparticles on graphene

The preparation of graphene on cobalt thin film was successful. Similar to previous works conducted in our institute, the Co thin film, after undergoing heating, demonstrated a high level of suitability for graphene synthesis. The characterization through LEED revealed a distinct and pleasing Moiré pattern, indicating a well-formed graphene structure. Additionally, the structure of graphene was successfully observed using STM, further confirming its acceptable quality. We observed that all particles changed shape when heated. They shifted from a rounded, sphere-like form to become flat islands, and this change was accompanied by the formation of an unrolling carpet. After heating at 720 K, most particles had a flat top surface, and heating to 820 K reduced their heights to below 2 nm.

Outlook The observed Moiré pattern after graphene synthesis is believed to arise from a single rotated layer of graphene on the Co surface. When comparing this phenomenon to heating above 773 K on W(110) surfaces, the particles exhibit less reduction in height. This finding indicates that further research should be conducted, extending the investigation to particle sizes within the range of 1 nm to 10 nm and exploring various stoichiometries.

A Appendix

A.1 Temperature reference sheet

I/A	T/°C	T/K	I/A	T/°C	T/K
0.1	86.717	359.717	2.3	703.355	976.355
0.2	114.746	387.746	2.4	731.384	1004.384
0.3	142.775	415.775	2.5	759.413	1032.413
0.4	170.804	443.804	2.6	787.442	1060.442
0.5	198.833	471.833	2.7	815.471	1088.471
0.6	226.862	499.862	2.8	843,5	1116.5
0.7	254.891	527.891	2.9	871.529	1144.529
0.8	282.92	555.92	3.0	899.558	1172.558
0.9	310.949	583.949	3.1	927.587	1200.587
1.0	338.978	611.978	3.2	955.616	1228.616
1.1	367.007	640.007	3.3	983.645	1256.645
1.2	395.036	668.036	3.4	1011.674	1284.674
1.3	423.065	696.065	3.5	1039.703	1312.703
1.4	451.094	724.094	3.6	1067.732	1340.732
1.5	479.123	752.123	3.7	1095.761	1368.761
1.6	507.152	780.152	3.8	1123.79	1396.79
1.7	535.181	808.181	3.9	1151.819	1424.819
1.8	563.21	836.21	4.0	1179.848	1452.848
1.9	591.239	864.239	4.1	1207.877	148.877
2.0	619.268	892.268	4.2	1235.906	1508.906
2.1	647.297	920.297	4.3	1263.935	1536.935
2.2	675.326	948.326	4.4	1291.964	1564.964

Table A.1: Temperature reference sheet

BIBLIOGRAPHY

[1] Georg Wulff. Xxv. zur frage der geschwindigkeit des wachsthums und der auflösung der krystallflächen. *Zeitschrift für Kristallographie-Crystalline Materials*, 34(1-6):449–530, 1901.

[2] VN Filipovich and AM Kalinina. On the critical radius of crystalline particle amorphization. *Strukturnye prevrashcheniya v steklakh pri povyshennykh temperaturakh*, pages 44–49, 1965.

[3] Claude R Henry. Morphology of supported nanoparticles. *Progress in surface science*, 80(3-4):92–116, 2005.

[4] J Bansmann, L Lu, M Getzlaff, and KH Meiwes Broer. Magnetic properties of transition metal films and islands on w (110). *Zeitschrift für Physik D Atoms, Molecules and Clusters*, 40:570–573, 1997.

[5] Isabelle ML Billas, A Chatelain, and Walt A de Heer. Magnetism from the atom to the bulk in iron, cobalt, and nickel clusters. *Science*, 265(5179):1682–1684, 1994.

[6] Isabelle ML Billas, JA Becker, A Châtelain, and Walt A de Heer. Magnetic moments of iron clusters with 25 to 700 atoms and their dependence on temperature. *Physical Review Letters*, 71(24):4067, 1993.

[7] B Lazarovits, L Szunyogh, and P Weinberger. Fully relativistic calculation of magnetic properties of fe, co, and ni adclusters on ag (100). *Physical Review B*, 65(10):104441, 2002.

[8] O Šipr, S Bornemann, J Minár, S Polesya, V Popescu, A Šimnek, and H Ebert. Magnetic moments, exchange coupling, and crossover temperatures of Co clusters on Pt (111) and Au (111). *Journal of Physics: Condensed Matter*, 19(9):096203, 2007.

[9] Murilo L Tiago, Yunkai Zhou, MM G_ Alemany, Yousef Saad, and James R Chelikowsky. Evolution of magnetism in iron from the atom to the bulk. *Physical review letters*, 97(14):147201, 2006.

[10] O Šipr, M Košuth, and H Ebert. Magnetic structure of free iron clusters compared to iron crystal surfaces. *Physical Review B*, 70(17):174423, 2004.

[11] GM Pastor, J Dorantes-Dávila, and KH Bennemann. Size and structural dependence of the magnetic properties of small 3d-transition-metal clusters. *Physical Review B*, 40(11):7642, 1989.

[12] O Šipr, J Minár, and Hubert Ebert. Magnetism of free and supported clusters: a comparative study. *Central European Journal of Physics*, 7:257–263, 2009.

[13] Fan Gao and Zhiyong Gu. Melting temperature of metallic nanoparticles. In *Handbook of Nanoparticles*, pages 661–690. Springer, 2016.

[14] Paneerselvam Antoniammal and Dakshanamoorthy Arivuoli. Size and shape dependence on melting temperature of gallium nitride nanoparticles. *Journal of Nanomaterials*, 2012:8–8, 2012.

[15] G Guisbiers and M Wautelet. Size, shape and stress effects on the melting temperature of nano-polyhedral grains on a substrate. *Nanotechnology*, 17(8):2008, 2006.

[16] Alexander van Teijlingen, Sean A Davis, and Simon R Hall. Size-dependent melting point depression of nickel nanoparticles. *Nanoscale Advances*, 2(6):2347–2351, 2020.

[17] Yan Liu, Yanxiu Chi, Shiyao Shan, Jun Yin, Jin Luo, and Chuan-Jian Zhong. Characterization of magnetic nife nanoparticles with controlled bimetallic composition. *Journal of alloys and compounds*, 587:260–266, 2014.

[18] Takayuki Kojima, Masaki Mizuguchi, Tomoyuki Koganezawa, Misako Ogiwara, Masato Kotsugi, Takumi Ohtsuki, Taka-Yuki Tashiro, and Koki Takanashi. Addition of co to l10-ordered feni films: influences on magnetic properties and ordered structures. *Journal of Physics D: Applied Physics*, 47(42):425001, 2014.

[19] Véronique Dupuis, G Khadra, A Hillion, Alexandre Tamion, Juliette Tuaillon-Combes, Laurent Bardotti, and Florent Tournus. Intrinsic magnetic properties of bimetallic nanoparticles elaborated by cluster beam deposition. *Physical Chemistry Chemical Physics*, 17(42):27996–28004, 2015.

[20] M Jamet, W Wernsdorfer, C Thirion, D Mailly, V Dupuis, P Mélinon, and A Pérez. Magnetic anisotropy of a single cobalt nanocluster. *Physical Review Letters*, 86(20):4676, 2001.

[21] IV Solovyev, PH Dederichs, and I Mertig. Origin of orbital magnetization and magnetocrystalline anisotropy in tx ordered alloys (where t= fe, co and x= pd, pt). *Physical Review B*, 52(18):13419, 1995.

[22] V Thiruvengadam, BB Singh, Takayuki Kojima, K Takanashi, Masaki Mizuguchi, and S Bedanta. Magnetization reversal, damping properties and magnetic anisotropy of l1-ordered feni thin films. *Applied Physics Letters*, 115(20), 2019.

[23] Yoshio Miura, Sho Ozaki, Yasushi Kuwahara, Masahito Tsujikawa, Kazutaka Abe, and Masafumi Shirai. The origin of perpendicular magneto-crystalline anisotropy in l10–feni under tetragonal distortion. *Journal of physics: Condensed matter*, 25(10):106005, 2013.

[24] D Ferrer, A Torres-Castro, X Gao, S Sepulveda-Guzman, U Ortiz-Mendez, and M Jose-Yacaman. Three-layer core/shell structure in au- pd bimetallic nanoparticles. *Nano letters*, 7(6):1701–1705, 2007.

[25] Pascal Andreazza, Veronique Pierron-Bohnes, Florent Tournus, Caroline Andreazza-Vignolle, and Veronique Dupuis. Structure and order in cobalt/platinum-type nanoalloys: from thin films to supported clusters. *Surface Science Reports*, 70(2):188–258, 2015.

[26] H Okamoto. Fe-pt (iron-platinum). *Journal of Phase Equilibria and Diffusion*, 25(4):395–395, 2004.

[27] RH Kodama. Magnetic nanoparticles. *Journal of magnetism and magnetic materials*, 200(1-3):359–372, 1999.

[28] Xuemin He and Huigang Shi. Size and shape effects on magnetic properties of ni nanoparticles. *Particuology*, 10(4):497–502, 2012.

[29] Ting-Wei Liao, Anupam Yadav, Kuo-Juei Hu, Johan van der Tol, Salvatore Cosentino, Francesco D'Acapito, Richard E Palmer, Cristina Lenardi, Riccardo Ferrando, Didier Grandjean, et al. Unravelling the nucleation mechanism of bimetallic nanoparticles with composition-tunable core–shell arrangement. *Nanoscale*, 10(14):6684–6694, 2018.

[30] R Cortenraad, SN Ermolov, VN Semenov, AW Denier van der Gon, VG Glebovsky, SI Bozhko, and HH Brongersma. Growth, characterisation and surface cleaning procedures for high-purity tungsten single crystals. *Journal of crystal growth*, 222(1-2):154–162, 2001.

[31] H-W Fink and Gert Ehrlich. Direct observation of overlayer structures on w (110). *Surface Science*, 110(1):L611–L614, 1981.

[32] Y Viswanath and LD Schmidt. Oxidation of carbon on (100) w and (100) mo. *The Journal of Chemical Physics*, 59(8):4184–4191, 1973.

[33] JA Becker, EJ Becker, and Re G Brandes. Reactions of oxygen with pure tungsten and tungsten containing carbon. *Journal of Applied Physics*, 32(3):411–423, 1961.

[34] U Köhler, C Jensen, C Wolf, AC Schindler, L Brendel, and DE Wolf. Investigation of homoepitaxial growth on bcc surfaces with stm and kinetic monte carlo simulation. *Surface science*, 454:676–680, 2000.

[35] Dong Chen, Wangyu Hu, Jianyu Yang, Huiqiu Deng, Lixian Sun, and Fei Gao. Diffusion of tungsten clusters on tungsten (110) surface. *The European Physical Journal B*, 68:479–485, 2009.

[36] Kenjiro Oura, VG Lifshits, AA Saranin, AV Zotov, and M Katayama. *Surface science: an introduction*. Springer Science & Business Media, 2013.

[37] R Butz and H Wagner. Surface diffusion of pd and au on w single crystal planes: I. spreading behaviour of pd and au layers. *Surface Science*, 87(1):69–84, 1979.

[38] R Butz and H Wagner. Surface diffusion of pd and au on w single crystal planes: Ii. anisotropy of pd surface diffusion due to the influence of substrate structure. *Surface Science*, 87(1):85–100, 1979.

[39] D Reuter, G Gerth, and J Kirschner. Anisotropic diffusion of 3 d metals on w (110): Competition between crystalline structure and surface steps. *Physical Review B*, 57(4):2520, 1998.

[40] Werner Pepperhoff and Mehmet Acet. *Constitution and Magnetism of Iron and its Alloys*. Springer Science & Business Media, 2001.

[41] Naraintorn Boonsong, I Ming Tang, Wuttichai Somyanonthanakun, and Sirikanjana Thongmee. Magnetic behavior of iron-rich permalloy nanoparticles. *Journal of Superconductivity and Novel Magnetism*, 31:2173–2177, 2018.

[42] Junais Habeeb Mokkath. Size and chemical order dependence of magnetic-ordering temperature and spin structure in fe@ ni and ni@ fe core–shell nanoparticles. *Physical Chemistry Chemical Physics*, 22(11):6275–6281, 2020.

[43] Huaqiang Wu, Cheng Qian, Yunjie Cao, Peipei Cao, Wenting Li, Xiaojun Zhang, and Xianwen Wei. Synthesis and magnetic properties of size-controlled feni alloy nanoparticles attached on multiwalled carbon nanotubes. *Journal of Physics and Chemistry of Solids*, 71(3):290–295, 2010.

[44] JF Hochepied, P Bonville, and MP Pileni. Nonstoichiometric zinc ferrite nanocrystals: syntheses and unusual magnetic properties. *The Journal of Physical Chemistry B*, 104(5):905–912, 2000.

[45] LJ Meng, XY Peng, C Tang, KW Zhang, GM Stocks, and JX Zhong. A quasicore-shell structure of feco and feni nanoparticles. *Journal of Applied Physics*, 108(10), 2010.

[46] Uhland Weissker, Silke Hampel, Albrecht Leonhardt, and Bernd Büchner. Carbon nanotubes filled with ferromagnetic materials. *Materials*, 3(8):4387–4427, 2010.

[47] Xiyou Cui. Self-thermoregulating ferromagnetic feni filled carbon nanotubes for magnetic hyperthermia cancer therapy. In *IOP Conference Series: Earth and Environmental Science*, volume 310, page 042016. IOP Publishing, 2019.

[48] AL Kozlovskiy, IV Korolkov, MA Ibragimova, MV Zdorovets, MD Kutuzau, LN Nikolaevich, EE Shumskaya, and E Yu Kaniukov. Magnetic nanostructured system for biomedical applications based on feni nanotubes. *Nanotechnologies in Russia*, 13:331–336, 2018.

[49] Gao Yang, Lihua Li, Wing Bun Lee, and Man Cheung Ng. Structure of graphene and its disorders: a review. *Science and technology of advanced materials*, 19(1):613–648, 2018.

[50] Björn Trauzettel. Von graphit zu graphen. *Physik Journal*, 6(7):39, 2007.

[51] Mikito Koshino. Interlayer screening effect in graphene multilayers with a b a and a b c stacking. *Physical Review B*, 81(12):125304, 2010.

[52] AA Avetisyan, B Partoens, and FM Peeters. Stacking order dependent electric field tuning of the band gap in graphene multilayers. *Physical Review B*, 81(11):115432, 2010.

[53] Mikito Koshino and Edward McCann. Gate-induced interlayer asymmetry in aba-stacked trilayer graphene. *Physical Review B*, 79(12):125443, 2009.

[54] Edward McCann and Mikito Koshino. Spin-orbit coupling and broken spin degeneracy in multilayer graphene. *Physical Review B*, 81(24):241409, 2010.

[55] RR Haering. Band structure of rhombohedral graphite. *Canadian Journal of Physics*, 36(3):352–362, 1958.

[56] Philip Richard Wallace. The band theory of graphite. *Physical review*, 71(9):622, 1947.

[57] DW Boukhvalov and MI Katsnelson. Chemical functionalization of graphene with defects. *Nano letters*, 8(12):4373–4379, 2008.

[58] Mikhail I Katsnelson. Graphene: carbon in two dimensions. *Materials today*, 10(1-2):20–27, 2007.

[59] Sukang Bae, Hyeongkeun Kim, Youngbin Lee, Xiangfan Xu, Jae-Sung Park, Yi Zheng, Jayakumar Balakrishnan, Tian Lei, Hye Ri Kim, Young Il Song, et al. Roll-to-roll production of 30-inch graphene films for transparent electrodes. *Nature nanotechnology*, 5(8):574–578, 2010.

[60] Shanshan Chen, Lola Brown, Mark Levendorf, Weiwei Cai, Sang-Yong Ju, Jonathan Edgeworth, Xuesong Li, Carl W Magnuson, Aruna Velamakanni, Richard D Piner, et al. Oxidation resistance of graphene-coated cu and cu/ni alloy. *ACS nano*, 5(2):1321–1327, 2011.

[61] Nasser AM Barakat, Ahmed G El-Deen, Zafar Khan Ghouri, and Saeed Al-Meer. Stable n-doped & feni-decorated graphene non-precious electrocatalyst for oxygen reduction reaction in acid medium. *Scientific REpORtS*, 8(1):3757, 2018.

[62] Holly Tetlow, J Posthuma De Boer, Ian J Ford, Dimitri Dimitrievich Vvedensky, Johann Coraux, and L Kantorovich. Growth of epitaxial graphene: Theory and experiment. *Physics reports*, 542(3):195–295, 2014.

[63] Yuriy Dedkov and Elena Voloshina. Graphene growth and properties on metal substrates. *Journal of Physics: Condensed Matter*, 27(30):303002, 2015.

[64] Patrick Zeller, Xinzhou Ma, and Sebastian Günther. Indexing moiré patterns of metal-supported graphene and related systems: strategies and pitfalls. *New Journal of Physics*, 19(1):013015, 2017.

[65] Santanu Das and Wonbong Choi. Graphene synthesis. *Graphene: Synthesis and Applications*, 3:27–63, 2011.

[66] A Varykhalov and O Rader. Graphene grown on co (0001) films and islands: Electronic structure and its precise magnetization dependence. *Physical Review B*, 80(3):035437, 2009.

[67] Pfeiffer Vacuum. The vacuum technology book volume ii. *Know-how Book*, 2013.

[68] Karl Jousten. *Handbuch Vakuumtechnik*. Springer-Verlag, 2018.

[69] John Meurig Thomas, Paul A Midgley, Caterina Ducati, and Rowan K Leary. Nanoscale electron tomography and atomic scale high-resolution electron microscopy of nanoparticles and nanoclusters: A short surveynanoscale electron tomography and atomic scale high-resolution electron microscopy of nanoparticles and nanoclus-

ters: A short surveyretain–. *Progress in Natural Science: Materials International*, 23(3):222–234, 2013.

[70] Cecile S Bonifacio, Sophie Carenco, Cheng Hao Wu, Stephen D House, Hendrik Bluhm, and Judith C Yang. Thermal stability of core–shell nanoparticles: A combined in situ study by xps and tem. *Chemistry of Materials*, 27(20):6960–6968, 2015.

[71] Daisuke Shindo and Tetsuo Oikawa. *Analytical electron microscopy for materials science*. Springer Science & Business Media, 2013.

[72] Wanfeng Li and Chaoying Ni. Electron energy loss spectroscopy (eels). *Encyclopedia of Tribology*, pages 940–945, 2013.

[73] Hellmut Haberland. *Clusters of atoms and molecules: theory, experiment, and clusters of atoms*, volume 52. Springer Science & Business Media, 2013.

[74] Jaroslav Kousal, Oleksandr Polonskyi, Ondřej Kylián, Andrei Choukourov, Anna Artemenko, Josef Pešička, Danka Slavinska, and Hynek Biederman. Characterization of nanoparticle flow produced by gas aggregation source. *Vacuum*, 96:32–38, 2013.

[75] Boris M Smirnov, Ibrahimkutty Shyjumon, and Rainer Hippler. Flow of nanosize cluster-containing plasma in a magnetron discharge. *Physical Review E*, 75(6):066402, 2007.

[76] Michael Köhler and Wolfgang Fritzsche. *Nanotechnology: an introduction to nanostructuring techniques*. John Wiley & Sons, 2008.

[77] M Ganeva, AV Pipa, and R Hippler. The influence of target erosion on the mass spectra of clusters formed in the planar dc magnetron sputtering source. *Surface and Coatings Technology*, 213:41–47, 2012.

[78] Matthew John Goeckner, John Arlin Goree, and Terrence E Sheridan. Monte carlo simulation of ions in a magnetron plasma. *IEEE transactions on plasma science*, 19(2):301–308, 1991.

[79] CG Granqvist and RA Buhrman. Ultrafine metal particles. *Journal of applied Physics*, 47(5):2200–2219, 1976.

[80] LB Kiss, J Söderlund, GA Niklasson, and CG Granqvist. New approach to the origin of lognormal size distributions of nanoparticles. *Nanotechnology*, 10(1):25, 1999.

[81] Oxford Applied Research. *NC200U Nanocluster Source Application Note*. Oxford Applied Research.

[82] M Ganeva, T Peter, S Bornholdt, H Kersten, T Strunskus, V Zaporojtchenko, F Faupel, and R Hippler. Mass spectrometric investigations of nano-size cluster ions produced by high pressure magnetron sputtering. *Contributions to Plasma Physics*, 52(10):881–889, 2012.

[83] Hendrik Bettermann. *Nanoparticles from 3d-metals: Influence of different substrates at different temperatures*. PhD thesis, 2018.

[84] O. Nanotechnology. *Triple Evaporator EFM 3T*. Scienta Omicron, 2004.

[85] JG Ociepa, Peter J Schultz, K Griffiths, and PR Norton. Re-emitted positron energy spectroscopy from thin co films on w (110). *Surface Science*, 225(3):281–291, 1990.

[86] S. Wanjelik Puljiz and M. Getzlaff. *Emissivity of polished tungsten surafaces as a function of temperature, detection angle and wavelength.* Frühjahrstagung der Sektion Kondensierte Materie, 2015.

[87] HJ Elmers, J Hauschild, H Höche, U Gradmann, H Bethge, D Heuer, and U Köhler. Submonolayer magnetism of fe (110) on w (110): Finite width scaling of stripes and percolation between islands. *Physical review letters*, 73(6):898, 1994.

[88] Niklas Andreas Nippe. Einfluss der stöchiometrie auf das schmelzverhalten deponierter legierungsnanopartikel, 2021.

[89] Lara Hölzle. Herstellung und charakterisierung von graphen auf einer metalloberfläche, 2023.

[90] Kai Besocke. Heating of size-selected feni-nanoparticles on a graphene surface, 2023.

Publications

Mahboobeh Ravankhah, Philipp Watermeyer, Gerard Dehm, Mathias Getzlaff. Elemental distribution and melting characteristics of FeNi nanoparticles on W(110) Surfaces. In preparation

Conference Contributions

- Mahboobeh Ravankhah, Mathias Getzlaff. Melting behavior of FeNi nanoparticles on surfaces. Poster, DPG- Frühestagung, Regensburg, 2018.
- Mahboobeh Ravankhah, Mathias Getzlaff. Temperature-induced processes for Fe_xNi_{1-x} nanoparticles on surfaces. Poster, Cluster treffen, Bad Honnef, 2019.
- Mahboobeh Ravankhah and Mathias Getzlaff. Deposition and annealing processes for FexNi1-xnanoparticles on surfaces. Poster, Symposium on Size Selected cluster, Davos, 2020.
- Mahboobeh Ravankhah and Mathias Getzlaff. Deposition and annealing of FeNi nanoparticles on surfaces. Talk, DPG- Frühestagung, Regensburg, 2022.
- Kai besocke, Mahboobeh Ravankhah, and mathias Getzlaff. Transition metal nanoparticles on graphene: Influence of temperature. Poster, DPG- Frühestagung, Dresden, 2023.

Dankesagung

I would like to thank Professor Getzlaff, my supervisor, for his constant kindness and for giving me the opportunity to do my doctorate at the Heinrich-Heine-University in Düsseldorf. His guidance and support have contributed significantly to my research progress and I am truly grateful for his help in navigating this journey.

I must express my gratitude to Professor Gerard Dehm for giving me the opportunity to visit and work in his laboratory at the Max Planck Institute for Iron Research. I would also like to thank Mr. Philipp Watermeyer for his valuable cooperation in the HRTEM measurements.

I would like to thank all my friends who make a lot of good memories in my life story: to Mona, Ehsan, Leila, Christiane, Hsiao-Ching, Maja. To all my students, who cooperate very well during their projects: Kai, Cedric, Dennis, Justus, Niklas, Lara. Thanks to Hendrik, who during my early days in the lab, generously shared their wealth of knowledge and provided invaluable guidance, and Thanks to Claudius for his consistent support and contribution throughout my Ph.D. journey.

Finally, but always first in my heart, thanks to my parents for inspiring me all the time with their love, to my sister for helping me in every second of my life, to my dear brothers. My special thank to my fiance, Masoud, who has been a constant source of support and encouragement, providing me with the strength to successfully navigate this journey.

EIDESSTATTLICHE VERSICHERUNG

Ich versichere an Eides statt, dass die Dissertation von mir eigenständig und ohne unzulässige externe Hilfe verfasst wurde und unter Einhaltung der 'Grundsätze zur Sicherung guter wissenschaftlicher Praxis' an der Heinrich-Heine-Universität Düsseldorf erstellt wurde. Alle direkt oder indirekt übernommenen Gedanken aus externen Quellen sind als solche deutlich gekennzeichnet. Nach meinem besten Wissen wurde diese Arbeit zuvor weder im Inland noch im Ausland in gleicher oder ähnlicher Form bei einer anderen Prüfungsbehörde eingereicht.

Düsseldorf, den 20 October,

Mahboobeh Ravankkhah